LUND UNIVERSITY
Faculty of Science

Searching for doubly charged Higgs bosons using same-sign hadronic tau final states —A focused study on the charge-flip background of hadronic taus

Shi Qiu

Thesis submitted for the degree of Master of Science
Project duration: 12 months

Supervised by Else Lytken

Department of Physics
Division of Particle Physics
Wednesday 14th August, 2019

I would like to dedicate this thesis to my loving parents

Acknowledgements

I would like to express my greatest appreciation to my supervisor Else Lytken for the guidance and great support throughout this masters project. Also, I deeply appreciate the help from Katja Mankinen, who is extremely efficient and is always able to provide helpful information when I am stuck. The help that I received from other PhD students and Post Docs is much appreciated as well.

Of course, the journey would be a lot harder without the company of friends in the ALTAS masters room. I would like to specifically thank Emelie Olsson, Jessamy Mol, Isabelle John and Alexander Ekman.

Abstract

The search for doubly charged Higgs bosons ($H^{\pm\pm}$) aims at resolving the mass generation mechanism of neutrinos in the Standard Model. The current search by the ATLAS Same-Sign Dilepton group uses the decay product of $H^{\pm\pm}$ to a pair of same-sign hadronic τ-leptons, which is an extension of their previous search using same-sign dielectrons and dimuons. This thesis focuses on the study of one of the backgrounds, known as the charge-flip background, as a result of the misidentification of the charge of hadronic τ-leptons by the ATLAS detector. To estimate this background, three methods are used with the data-driven and tag-and-probe method applied to MC simulated samples and the template fit method applied to detector data collected from 2015 to 2017 by the ATLAS detector at $\sqrt{s} = 13$ TeV with a total integrated luminosity of 79.8 fb^{-1}. The charge-flip rate of hadronic τ-leptons rises from around 0.3% to 2.2% with the increase of pseudorapidity from 0 to 2.5, while the charge-flip rate for detector ranges from 0.4% to 3.8%. This leads to a successful calculation of the scale factor equalling to 1.52 ± 0.42.

Table of contents

List of figures

List of tables

Nomenclature

Roman Symbols

c	charm quark
D	covariant derivative
d	down quark
e	electron
h	Standard Model Higgs boson
$H^{\pm\pm}$	doubly charged Higgs boson
$H^{\pm}$	singly charged Higgs boson
L	likelihood function
l	lepton
m	mass
P	probability density function
q	quark
R	distance parameter
s	strange quark
t	top quark
u	up quark
W	W boson
Z	Z boson

Greek Symbols

ε	charge flip rate
η	pseudorapidity
Γ	decay width
γ	photon
λ	expected number of charge-flipped events
μ	muon
ν_μ	muon neutrino
ν_τ	tau neutrino
ν_e	electron neutrino
ν_l	neutrino
ϕ	azimuthal angle
π	pion
π^0	neutral pion
$\pi^\pm$	charged pion
σ	cross section
τ	tau lepton
θ	polar angle

Other Symbols

$\mathscr{L}_{\text{int}}$	integrated luminosity
$\sqrt{s}$	central mass energy
d_0	impact parameter
E_T^{miss}	missing transverse momentum
m_T	transverse mass

N_{events} total number of events

N_{AS} number of any-sign events

N_{OS} number of opposite-sign events

N_{SS} number of same-sign events

p_T transverse momentum

v_Δ vacuum expectation value of the doubly charged Higgs boson

v_Φ Standard Model vacuum expectation value

Acronyms / Abbreviations

ATLAS A Toroidal LHC ApparatuS

BDT Boost Decision Tree

CSCs Cathode Strip Chambers

DxAOD Derived Analysis Data Object

ECal electromagnetic calorimeter

HCal hadronic calorimeter

HLT High-Level Trigger

ID inner tracking detector

IP interaction point

L1 first-level trigger

LHC Large Hadron Collider

MC Monte Carlo

MDTs Monitored Drift Tubes

RDO RAW Data Objects

SCT semi-conductor tracker

SSDiLep ATLAS Same-Sign Dilepton group

TRT transition radiation tracker

VEV vacuum expection value

VP1 Virtual Point-1

xAOD Analysis Data Object

Chapter 1

Introduction

The generation mechanism of neutrino mass is one of the major problems remaining in the Standard Model. A possible solution is to introduce exotic Higgs bosons which generate the masses of neutrinos through the See-saw mechanism. The ATLAS Same-Sign Dilepton (SSDiLep) group studies doubly charged Higgs bosons, predicted in a large variety of models beyond the Standard Model. The doubly charged Higgs boson has the unique characteristic of decaying into two particles of the same charge. In this chapter, I will first introduce the theoretical background of the Standard Model and various theories of doubly charged Higgs boson. This is followed by a description of the ATLAS experiment including the detector components and data processing.

1.1 Theoretical background

1.1.1 The Standard Model

The Standard Model of fundamental particles is formulated as a quantum field theory which describes the interaction of electromagnetic, weak and strong force between fermions (following Fermi–Dirac statistics) and bosons (following Bose–Einstein statistics). The mathematical formalism is built from the principle that the physics is invariant under a combination of local gauge symmetry $U(1)_Y \otimes SU(2)_L \otimes SU(3)_C$, where the subscripts denote corresponding degrees of freedom called weak hyper-charge Y, weak isospin L and colour C.

As proposed by Glashow, Salam and Weinberg [8–10], the electromagnetic and weak force can be combined into one known as the electroweak force with three postulated weak force mediating bosons ($W^{\pm}, Z^0$) belonging to the non-abelian [1] group $SU(2)$ and one electromagnetic force mediator (γ) belonging to the abelian [2] group $U(1)$. Both types of fermions, leptons

[1] non-commutative group elements
[2] commutative group elements

and quarks, are involved in electroweak interactions. The lepton can be separated into two classes: charged leptons $l^i = \{e, \mu, \tau\}$ and neutral leptons $\nu_i = \{\nu_e, \nu_\mu, \nu_\tau\}$. Depending on the direction of the spin and the momentum, a lepton is left-handed if the spin aligns in the opposite direction of the momentum and otherwise is called right-handed. Each type of left-handed (a.k.a. left-chiral or active) neutrino (ν_{eL}, $\nu_{\mu L}$, $\nu_{\tau L}$) together with a charged lepton partner (e_L, μ_L, τ_L) forms a SU(2) doublet

$$L^i = \begin{pmatrix} \nu_{lL}^i \\ l_L^i \end{pmatrix} \quad i = 1,2,3 \tag{1.1}$$

and each right-handed charged lepton (e_R, μ_R, τ_R) forms a SU(2) singlet, l_R^i, since no right-handed neutrinos have been found experimentally. Each component, ν_l^i, l^i or l_R^i, is a Dirac spinor, which contains the information of its spin and momentum. There are six flavours of quarks up (u), down (d), strange (s), charm (c), top (t) and bottom (b). The u, c, and t quarks are commonly classified as up-type quarks with charge $2e/3$, and the d, s, and b quarks are categorised as down-type quarks with charge -e/3. Similarly, a pair of left-handed up-type and down-type quark forms a $SU(2)$ doublet

$$Q_{L,\alpha}^i = \begin{pmatrix} u_\alpha^i \\ d_\alpha^i \end{pmatrix} \quad i = 1,2,3; \quad \alpha = r,g,b \text{ (red,green and blue)} \tag{1.2}$$

and right-handed quarks form $U(1)$ singlets, $u_{R,\alpha}^i$ and $d_{R,\alpha}^i$. Besides the information of spin and momentum carried by the Dirac spinor of each quark, it also carries a 3-valued hidden quantum number known as the colour state (represented by α), red (1,0,0), green (0,1,0) and blue (0,0,1), which means that quarks can also be put into so-called colour $SU(3)$ triplets.

The theory of strong interactions is known as Quantum Chromodynamics, which is formulated as an $SU(3)$ non-abelian gauge theory and describes the interactions of quarks and gluons [11, 12]. There are eight massless gluons as strong force mediators with each carrying a possible combination of colour and anticolour state. Gluons interact with quarks and change the colour of final state quarks. Unlike four bosons in electroweak interaction, gluons can also couple to themselves. It should be noted that leptons are colourless particles (considered as containing all three colour states which leads to white coloured state), so they do not participate in the strong interaction.

Lastly, there is a scalar Higgs boson field interacting with fermions and other gauge bosons through weak interactions which explains how particles gain their masses through the Higgs mechanism. The most important concept in the Higgs mechanism is the spontaneous symmetry breaking. It is better to illustrate this idea through a very simple case: a Lagrangian for a scalar

field (a toy model of the Higgs field)

$$\mathscr{L} = T - V = \frac{1}{2}\partial_\mu\phi\partial^\nu\phi - \left(\frac{1}{2}\mu^2\phi^2 + \frac{1}{4}\lambda\phi^4\right), \tag{1.3}$$

which is invariant under the Z_2 symmetry $\phi \to -\phi$. For $\mu^2 > 0$, the minimum of the potential, V, is at $\phi = 0$. There is no constraint on the value of μ^2, however. The potential is minimised at two possible values

$$\phi = \pm\sqrt{\frac{-\mu^2}{\lambda}} = v_\phi \tag{1.4}$$

for $\mu^2 < 0$, where v_ϕ is called the vacuum expectation value (VEV) of ϕ. Now we expand the Lagrangian around one of the minima, e.g.

$$\phi(x) = \sqrt{\frac{-\mu^2}{\lambda}} + \tilde{\phi}(x), \tag{1.5}$$

where the excitation $\tilde{\phi}(x)$ is small, then the Lagrangian becomes

$$\mathscr{L} = \frac{1}{2}(\partial_\mu\tilde{\phi}\partial^\mu\tilde{\phi}(x)) - \left(\lambda v^2\tilde{\phi}^2 + \lambda v\tilde{\phi}^3 + \frac{1}{4}\lambda\tilde{\phi}^4\right) + \text{constant}, \tag{1.6}$$

which is still invariant under the original Z_2 symmetry, meaning that $\tilde{\phi}$ transforms as $\tilde{\phi} \to -\tilde{\phi} - 2v_\phi$ since $\phi = v_\phi + \tilde{\phi}$. However, when a specific choice of the vacuum expectation value is made, the symmetry of the Lagrangian is broken, though the two possible values are equivalent for the theory. This is known as the spontaneous symmetry breaking. In addition, the term with $\tilde{\phi}^2$ can be interpreted as a particle with mass $m_{\tilde{\phi}}^2 = 2\lambda v_\phi^2$. In the Standard Model case, the Higgs Lagrangian is given as

$$\mathscr{L}_{Higgs} = |D_\mu\Phi|^2 - \left(\mu^2\Phi^\dagger\Phi + \lambda(\Phi^\dagger\Phi)^2\right), \tag{1.7}$$

where $D_\mu = \partial_\mu - ig_1\frac{\sigma^i}{2}\cdot W_\mu^i - ig_2\frac{Y}{2}B_\mu - ig_3\frac{\lambda^a}{2}G_\mu^a$ is the covariant derivative so as to ensure invariance of Lagrangian under gauge transformation. In the covariant derivative, g_1, g_2 and g_3 are the usual $SU(2)_L$, $U(1)_Y$ and $SU(3)_C$) gauge couplings, σ^i, $i = 1,2,3$, are the $SU(2)_L$ generators also known as the Pauli matrices, Y is the $U(1)_Y$ generator, λ^a, $a = 1,2,...,8$, (a.k.a. the Gell-Mann matrices) are the $SU(3)_C$ generators, the terms W^i and B^μ are the gauge field for the $SU(2)_L$ group and $U(1)$ group of weak hypercharge Y, respectively, and G_μ^a represents gluon fields. The Higgs field is assigned to an $SU(2)$ doublet in form of two complex fields Φ^+ and Φ^0

$$\Phi = \begin{pmatrix} \Phi^+ \\ \Phi^0 = \frac{1}{\sqrt{2}}(v_\Phi + h + i\chi) \end{pmatrix}, \tag{1.8}$$

where Φ^+ and χ are unphysical Goldstone boson fields and h is the real physical Higgs field. Without showing detailed mathematics, we claim that the Goldstone boson arises whenever a continuous global symmetry ($\Phi \to \Phi' = e^{i\chi}\Phi$ in this case) is spontaneously broken due to a particular choice of the group state. Inserting the Higgs doublet field into the Higgs Lagrangian and dropping the Goldstone bosons, the Higgs Lagrangian becomes

$$\mathscr{L}_{Higgs} = \frac{1}{2}(\partial_\mu h)^2 + \frac{g_1^2}{4}(v_\Phi + h)^2 W_\mu^+ W^{\mu,-} + \frac{g_1^2+g_2^2}{8}(v_\Phi+h)^2 Z_\mu Z^\mu + \frac{\mu^2}{2}(v_\Phi+h)^2 - \frac{\lambda}{16}(v_\Phi+h)^4, \tag{1.9}$$

where $W_\mu^\pm$, Z_μ and h corresponds to the gauge boson $W^\pm$, Z and Higgs with each mass equalling to

$$m_W = \frac{g_1 v_\Phi}{2}, \quad m_Z = \frac{1}{2} v_\Phi \sqrt{g_1^2+g_2^2}, \quad m_h = \sqrt{2\mu^2}. \tag{1.10}$$

The Higgs field also yields the masses of charged leptons and quarks through Yukawa interactions in a similar way, while the neutrinos cannot acquire masses through this way due to the fact that no right-handed neutrinos exist in the Standard Model.

1.1.2 Beyond the Standard Model physics

The experimental observations of the phenomenon of neutrino oscillation provide the strongest evidence that neutrinos have non-zero mass (see e.g. [13]). This phenomenon means that the flavour state of the neutrino, defined based on the charged lepton that it is produced with, oscillates down the line of propagation leading to a theoretical requirement of all neutrinos to be massive [14]. Several extensions of the Standard Model are proposed to solve the generation mechanism of neutrino masses. This project focuses on extensions of the Higgs sector involving doubly charged Higgs, which appears in, e.g., left-right symmetric models, Higgs triplet models, the little Higgs model, type-II see-saw models, and the Zee–Babu neutrino mass model [3]. Two of the models in its typical construction, the Higgs triplet model and the left-right symmetric model, are introduced in the following subsections, with a more detailed description on the first one.

The Higgs triplet model

In this section, we introduce the concept of the Higgs triplet model based on [15–21]. The detailed derivation is generally not recorded in the literature, so some of the derivations represent my study and work. This model is a minimal extension of the Higgs sector by adding a $SU(2)_L$ (2×2 representation) triplet of scalar particles

$$\Delta = \begin{pmatrix} \frac{\Delta^+}{\sqrt{2}} & \Delta^{++} \\ \Delta^0 = \frac{1}{\sqrt{2}}(v_\Delta + \delta + i\eta) & -\frac{\Delta^+}{\sqrt{2}} \end{pmatrix}, \tag{1.11}$$

where v_Δ is VEV for the triplet Higgs field, with $v^2 \equiv v_\Phi^2 + 2v_\Delta^2 \simeq (246\,\text{GeV})^2$. There are seven physical mass eigenstates predicted in this model: singly charged Higgs bosons ($H^\pm$), doubly charged Higgs bosons ($H^{\pm\pm}$), neutral CP-odd A^0, and neutral CP-even H^0 and h^0 (the Standard Model Higgs boson), where only $H^{\pm\pm}$ is of interest in our analysis. Neutrinos can obtain mass via v_Δ in this triplet representation, and the magnitude of v_Δ is assumed to be less than 1 GeV to ensure the smallness of neutrino masses. The most general scalar potential involving the Standard Model doublet Φ, defined in Eq. (1.8) and triplet Δ is given by

$$\begin{aligned} V(\Phi,\Delta) =& m_\Phi^2(\Phi^\dagger\Phi) + \lambda_1(\Phi^\dagger\Phi)^2 + M_\Delta^2\text{Tr}(\Delta^\dagger\Delta) + \lambda_2\left[\text{Tr}(\Delta^\dagger\Delta)\right]^2 + \lambda_3\text{Tr}\left[(\Delta^\dagger\Delta)^2\right] \\ &+ \lambda_4(\Phi^\dagger\Phi)\text{Tr}(\Delta^\dagger\Delta) + \lambda_5\Phi^\dagger\Delta^\dagger\Delta\Phi + \left[\mu(\Phi^T i\sigma_2\Delta^\dagger\Phi) + h.c.\right], \end{aligned} \tag{1.12}$$

where m_Φ and M_Δ are the bare Higgs doublet and triplet mass, respectively, $\lambda_1 - \lambda_5$ are real parameters in the Higgs potential, μ is a complex parameter for the lepton number violation term and σ_2 is the second Pauli matrix. The reason that the last term violates the lepton number is because it couples two Standard Model Higgs bosons each with lepton number 0 to a doubly charged Higgs boson which lepton number would equal to ± 2 if the lepton number is conserved in the $H^{\pm\pm} \to l^\pm l^\pm$ decay. Similar to the procedure in the Standard Model Higgs, we have

$$\langle\Phi\rangle_0^\dagger\langle\Phi\rangle_0 = \frac{1}{\sqrt{2}}\begin{pmatrix}0 & v_\Phi\end{pmatrix}\frac{1}{\sqrt{2}}\begin{pmatrix}0\\ v_\Phi\end{pmatrix} = \frac{v_\Phi^2}{2} \tag{1.13}$$

and

$$\langle\Delta\rangle_0^\dagger\langle\Delta\rangle_0 = \frac{1}{\sqrt{2}}\begin{pmatrix}0 & v_\Delta^*\\ 0 & 0\end{pmatrix}\frac{1}{\sqrt{2}}\begin{pmatrix}0 & 0\\ v_\Delta & 0\end{pmatrix} = \frac{1}{2}\begin{pmatrix}|v_\Delta|^2 & 0\\ 0 & 0\end{pmatrix} = \frac{1}{2}\begin{pmatrix}w^2 & 0\\ 0 & 0\end{pmatrix}, \tag{1.14}$$

where $v_\Delta = we^{i\varphi}$ with $w = |v_\Delta|$ is complex due to the global symmetry of lepton number broken by the lepton number violation term. The potential as a function of the VEVs is given by

$$\begin{aligned} V(\langle\Phi\rangle_0,\langle\Delta\rangle_0) =& \frac{1}{2}m_\Phi^2 v_\Phi^2 + \frac{1}{4}\lambda_1 v_\Phi^4 + \frac{1}{2}M_\Delta^2 w^2 + \frac{1}{4}\lambda_2 w^4 + \frac{1}{4}\lambda_3 w^4 \\ &+ \frac{1}{4}\lambda_4 v_\Phi^2 w^2 + \frac{1}{4}\lambda_5 v_\Phi^2 w^2 - \frac{1}{\sqrt{2}}|\mu| v_\Phi^2 w\cos(\omega+\varphi), \end{aligned} \tag{1.15}$$

where in the last term, we have $\mu v_\Delta = |\mu| w e^{i(\omega+\varphi)}$ so that $\mu v_\Delta + (\mu v_\Delta)^\dagger = 2|\mu| w\cos(\omega+\varphi)$. Minimising with respect to φ gives $\omega + \varphi = n\pi$ and we choose $\omega + \varphi = 0$. This is followed by minimising with respect to v_Φ and w, which yields

$$\begin{cases} m_\Phi^2 + \lambda_1 v_\Phi^2 + \frac{1}{2}\lambda_4 w^2 + \frac{1}{2}\lambda_5 w^2 - \sqrt{2}|\mu| w = 0 \\ M_\Delta^2 w + \lambda_2 w^3 + \lambda_3 w^3 + \frac{1}{2}\lambda_4 v_\Phi^2 w + \frac{1}{2}\lambda_5 v_\Phi^2 w - \frac{1}{\sqrt{2}}|\mu| v_\Phi^2 = 0. \end{cases} \tag{1.16}$$

By making the approximation $w, |\mu| \ll v_\Phi$ and $v_\Phi \ll M_\Delta$, we find that

$$\begin{cases} v_\Phi^2 \simeq -m_\Phi^2/\lambda_1 \\ |v_\Delta| \simeq \frac{|\mu| v_\Phi^2}{\sqrt{2}(M_\Delta^2 + v_\Phi^2(\lambda_4+\lambda_5)/2)} \simeq \frac{|\mu| v_\Phi^2}{\sqrt{2} M_\Delta^2}, \end{cases} \tag{1.17}$$

which shows that $|v_\Delta|$ is small as long as $|\mu|, v_\Phi \ll M_\Delta$. By assuming that neutrinos are Majorana particles, the masses can be obtained from the Yukawa interaction

$$\mathscr{L}_{Yuk} = h_{ll'} L_l^T C i\sigma_2 \Delta L_{l'} + h.c. = h_{ll'} \begin{pmatrix} \nu_l & l_L \end{pmatrix} C i \begin{pmatrix} 0 & -i \\ i & 0 \end{pmatrix} \begin{pmatrix} \frac{\Delta^+}{\sqrt{2}} & \Delta^{++} \\ \Delta^0 & -\frac{\Delta^+}{\sqrt{2}} \end{pmatrix} \begin{pmatrix} \nu_{l'} \\ l'_L \end{pmatrix} + h.c., \tag{1.18}$$

where $h_{ll'}$ $(l, l' = e, \mu, \tau)$ is the coupling, C is the charge conjugation operator. The neutrino mass matrix comes from the term containing $\nu_l \nu_{l'}$, which equals to

$$m_\nu^{ll'} = 2 h_{ll'} \langle \Delta^0 \rangle = \sqrt{2} h_{ll'} |v_\Delta| = h_{ll'} \frac{|\mu| v_\Phi^2}{M_\Delta^2}. \tag{1.19}$$

The masses for the physical mass eigenstates can be obtained by expanding Eq. (1.12) in a similar way. It should be noted that the mass eigenstates are in general a mix of doublet and triplet fields except for $H^{\pm\pm}$ which is entirely comprised of the triplet scalar field $\Delta^{\pm\pm}$, as shown below

$$H^{\pm\pm} = \Delta^{\pm\pm}, \quad \text{with mass } m_{H^{\pm\pm}} = m_{\Delta^{\pm\pm}} \tag{1.20}$$

$$H^\pm = -\phi^\pm \sin\beta_\pm + \Delta^\pm \cos\beta_\pm, \quad \text{with } \tan\beta_\pm = \frac{\sqrt{2} v_\Delta}{v_\Phi} \tag{1.21}$$

$$A^0 = -\chi \sin\beta_0 + \eta \cos\beta_0, \quad \text{with } \tan\beta_0 = \frac{2 v_\Delta}{v_\Phi} \tag{1.22}$$

$$\text{and} \quad \begin{pmatrix} h^0 \\ H^0 \end{pmatrix} = \begin{pmatrix} \cos\alpha & \sin\alpha \\ -\sin\alpha & \cos\alpha \end{pmatrix} \begin{pmatrix} h \\ \delta \end{pmatrix} \quad \text{with } \tan\alpha \approx \frac{2 v_\Delta}{v_\Phi}. \tag{1.23}$$

Without performing the tedious expansion, we show the result of the squared mass of the doubly charged scalar

$$m_{H^{++}}^2 = M_\Delta^2 + \frac{\lambda_4}{2} v_\Phi^2 + \lambda_2 v_\Delta^2. \tag{1.24}$$

The left-right symmetric model

The following description of the left-right symmetric model is based on [22–25]. In the minimal version of this model, the broken symmetry of left- and right-handed particles is restored by extending the symmetry in the electroweak sector to include right-handed fermions as doublets

in $SU(2)_R$ group

$$SU(3)_C \otimes SU(2)_L \otimes SU(2)_R \otimes U(1)_{B-L}, \tag{1.25}$$

where $B-L$ is the baryon number subtracted by the lepton number. This also implies the existence of heavy right-handed gauge bosons $W_R^{\pm}$ and Z_R^0 coupling to the right-handed set of particles. The Higgs sector consists of a bidoublet ϕ [3], and a left- and right-handed triplet as shown below

$$\phi = \begin{pmatrix} \phi_1^0 & \phi_1^+ \\ \phi_2^- & \phi_2^0 \end{pmatrix}, \quad \Delta_{L/R} = \begin{pmatrix} \frac{\Delta_{L/R}^+}{\sqrt{2}} & \Delta^{++} \\ \Delta_{L/R}^0 & -\frac{\Delta_{L/R}^+}{\sqrt{2}} \end{pmatrix}, \tag{1.26}$$

where the neutral components can potentially acquire complex VEVs

$$\langle \phi \rangle_0 = \begin{pmatrix} \frac{\kappa_1}{\sqrt{2}} & 0 \\ 0 & \frac{\kappa_2}{\sqrt{2}} \end{pmatrix}, \quad \langle \Delta_{L/R} \rangle_0 = \begin{pmatrix} 0 & 0 \\ \frac{v_{L/R}}{\sqrt{2}} & 0 \end{pmatrix}, \tag{1.27}$$

with v_L and v_R breaking the symmetry $SU(2)_R \otimes U(1)_{B-L} \to U(1)_Y$ at a high energy scale, $\kappa = \sqrt{\kappa_1^2 + \kappa_2^1} = 246$ GeV breaking the Standard Model $SU(2)_L \otimes U(1)_Y$ symmetry and VEVs furthermore obey the hierarchy $v_L \ll \kappa_{1,2} \ll v_R$. Through the type-I see-saw mechanism, the left-handed neutrinos obtain masses but the right-handed neutrinos acquire heavy masses (see e.g. [26] for more details on the type-I see-saw mechanism).

1.2 The Large Hadron Collider

The Large Hadron Collider (LHC) with a circumference of 27 km is the world's largest circular particle accelerator primarily colliding proton beams but also capable of performing heavy-ion collisions of two types: lead-lead collisions and Xenon-Xenon collisions. Before accelerating protons or ions in the LHC, a series of accelerators are used to bring up the energy of particles. In the example of protons, the linear accelerator LINAC2 first accelerates protons to 50 MeV. Then the Protons Synchrotron Booster, made up of four superimposed synchrotron rings, accelerates protons to 1.4 GeV, followed by injecting into the Proton Synchrotron, which has a circumference of 628 metres, brings up the energy to 26 GeV. Afterwards, the Super Proton Synchrotron, the second largest accelerator at CERN with a circumference of 7 kilometres, accelerates protons to 450 GeV before injecting into and getting accelerated at the LHC, where the current highest energy for protons can reach 6.5 TeV. Protons or heavy ions in the beam pipe are grouped into dense bunches and eight radio frequency cavities per beam in the LHC are responsible for accelerating the bunches. In order to keep the circulating beams inside the vacuum chamber, 1232 magnetic dipoles situated inside the collider and 392 quadruple magnets are used to curve

[3] A bidoublet consists of two copies of doublets.

and focus the beams, respectively. Before the collision, particles are squeezed closer by a special type of magnet to increase the chances of collisions. At the collision point, two bunches from opposite beams inter-penetrate each other every 25 ns during Run II, which is known as the bunch crossing. Multiple collisions take place for each bunch crossing leading to the pile-up effect, which essentially is the background created by collisions apart from the collision of interest.

One vital parameter for an accelerator is the luminosity which characterises the number of collisions per unit area and per unit time in a detector. Mathematically, it is given by the following expression [27]:

$$L = F\frac{N_1 N_2 n_b f_r \gamma}{4\pi\varepsilon\beta^*} \tag{1.28}$$

where F is the geometrical luminosity reduction factor coming from the crossing angle of two beams at the interaction point (IP), N_1 and N_2 are the number of particles per bunch from each beam, n_b is the number of bunches per beam, f_r is the revolution frequency, γ is the relativistic factor, and the denominator is the beam size expressed in terms of two quantities: one being the normalised transverse emittance (a quantity characterising the parallelism of a beam), ε, and the other, the amplitude function (roughly being the width of the beam squared divided by ε at the interaction region), β^*.

More commonly, the quantity integrated luminosity $\mathscr{L}_{\text{int}}$ is used, which is defined as the integration of the luminosity over the period of observation

$$\mathscr{L}_{\text{int}} = \int_0^t L dt. \tag{1.29}$$

The total number of events for a physics process with cross-section σ is related to the luminosity and integrated luminosity by

$$N_{events} = \int_0^t L\sigma dt = \mathscr{L}\sigma. \tag{1.30}$$

1.2.1 The ATLAS detector

The ATLAS (A Toroidal LHC ApparatuS) detector is one of the two general-purpose detectors at the LHC consisting of a series of cylindrical detectors (barrel region), enclosed by two end-cap with each composed of several layers of disk-like detectors, as shown in Fig. 1.1. The interaction point is surrounded by the hermetic ATLAS detector, with a coverage of $|\eta| \lesssim 4.9$, where η is the pseudorapidity related to the polar angle, θ, by $\eta = -\ln\tan\theta/2$. Note that ATLAS uses a right-handed coordinate system with the origin located at the interaction point. The positive x-axis points from the interaction point towards the centre of the LHC tunnel, the positive y-axis points upward and the z-axis runs along the beam pipe. The polar angle is measured from the positive z-axis. The detector can be divided into four main components: the magnet system,

the inner detector, the calorimeter and the muon spectrometer. The following summary of each component is based on similar presentations which can be found in e.g. [28–30].

Magnet system

The superconducting magnet system in the ATLAS detector is responsible for bending the charged particles so that their momenta can be measured from the curvature of the trajectories. In addition, the trajectories can be used to determine the sign of charged particles. There are three main sections: the central solenoid magnet, the barrel toroid and two end-cap toroids. The central solenoid magnet is designed to generate a 2 T magnetic field along the beam axis for the inner detector with a nominal current of 7.73 kiloamperes. The barrel toroid, consisting of eight separate coils, and two end-cap toroids situated external of the hadronic calorimeter and within the muon system, producing magnetic fields ranging between 2 to 6 T for the muon detectors in the cylindrical region and end-cap region, respectively.

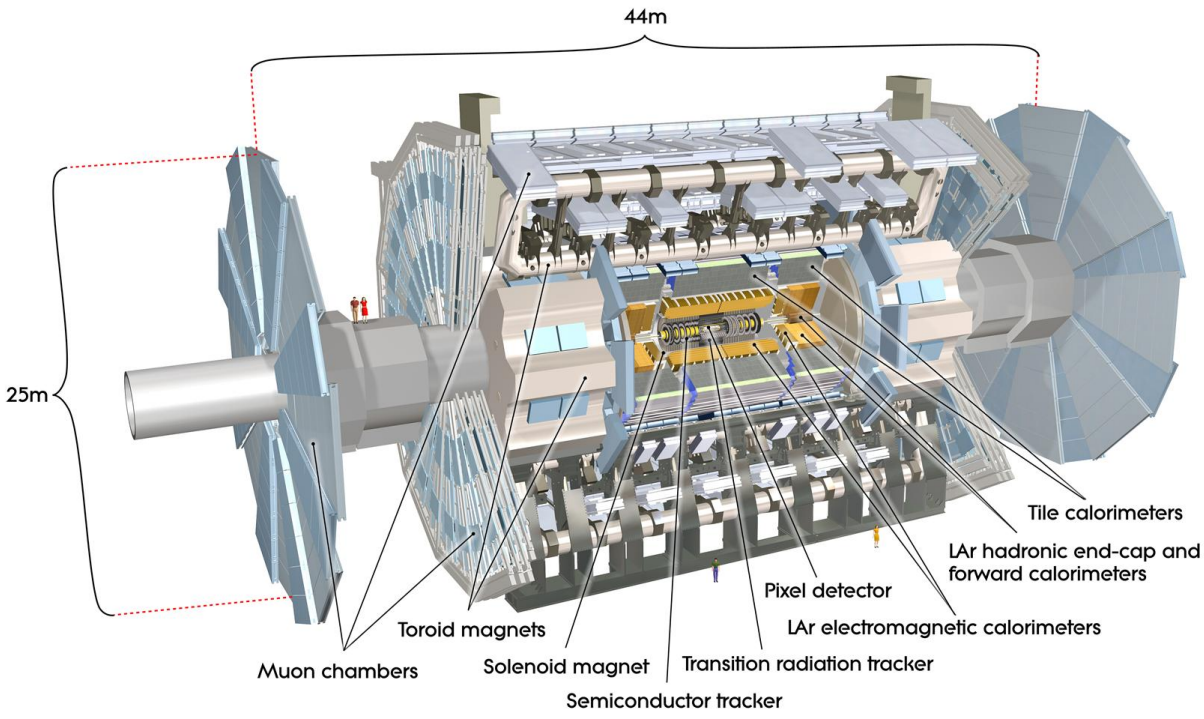

Fig. 1.1 Schematic diagram of the ATLAS detector [1].

Inner detector and the insertable B-layer

The inner tracking detector (ID) is the innermost component surrounding the interaction point, starting from a few centimetres away from the beam axis to a radial distance of 1.2 metres. It is very compact and highly sensitive, which provides hermetic, accurate momentum measurement

of charged particles and excellent primary and secondary vertex resolution. It should be noted that neutral particles do not interact with the ID, so that no tracks are left. The ID can be separated into three independent sub-detectors: the silicon pixel detector, the semi-conductor tracker (SCT) and the transition radiation tracker (TRT).

The silicon pixel detector is the first layer, which consists of three barrel layers and three pixel disks on each end covering a range of $|\eta| < 2.5$. With its designed spatial resolution of 10 μm, it is capable of providing information on the impact parameter (d_0) and identifying short-lived particles. The insertable B-layer was added as an additional layer between the ID and the beam pipe in 2014 so as to further improve the tracking performance.

The SCT is the middle component, which functions similar to the silicon pixel detector but uses silicon microstrip trackers distributed over 4 barrel layers and 18 end-cap discs to reduce the cost.

The outermost layer is the TRT, consisting of layers of straw drift tubes filled with a mixture of gas (70% Xe, 27% CO_2 and 3% O_2) with transition radiation material interwoven in between. Note that due to the leaking of the gas in the TRT, some parts of the detector are now filled with argon-based mixture, 70% Ar, 27% CO_2 and 3% O_2) [31]. Argon-based mixture is not as good for particle identification as it cannot absorb the transition radiation photons as well as xenon due to a lower atomic number, but it is cheaper than Xe-based gas mixture. When charged particles pass through the tubes, the gas gets ionised leading to a current pulse in the wire located in the centre of each straw. The transition radiation material creates a boundary of two media with different refraction indices, which induces transition radiations when charged particles pass through so as to enhance their signals. In addition, improved signals of different characteristics can be used to improve electron and pion identification.

Calorimeters

The calorimeter is designed to measure the energy of particles by absorbing them. Depending on the types of incoming particles, the calorimeter system is separate to the electromagnetic calorimeter (ECal) and the hadronic calorimeter (HCal). The ECal absorbs mostly photons, electrons and positrons that interact electromagnetically. It consists of a barrel region, covering $|\eta| < 1.475$, and two end-cap regions, covering $1.375 < |\eta| < 3.2$. In the experimental analysis, the transition region, $1.37 < |\eta| < 1.52$, is usually excluded. The hadronic calorimeter is dedicated to measure the energy of hadrons through their strong interaction with the detector material. It consists of three parts, which are the tile calorimeter, two hadronic end-cap calorimeters and the forward calorimeter covering the range of $\eta < 1.7$, $1.5 < |\eta| < 3.2$ and $3.1 < |\eta| < 4.9$, respectively.

Muon spectrometer

The muon spectrometer is placed at the outermost layer of the detector because muon can travel through calorimeters easily. It consists of two parts: the Monitored Drift Tubes (MDTs) for the low η region and the Cathode Strip Chambers (CSCs) in the forward region, which together cover a range of $|\eta| < 2.7$. The momentum of the muon is measured based on the magnetic deflection effect of the trajectories by the magnetic field surrounding the muon spectrometer.

1.2.2 The ATLAS trigger system

The collisions at the ATLAS detector, in the case of proton-proton collisions, take place 1.7 billion times per second, which generate around 60 Terabytes of data per second. The ATLAS trigger system is designed to pre-select the events of interest based on the preset energy thresholds and angle criteria, so as to greatly reduce the amount of data. Since 2012 run, the trigger system has been significantly upgraded in order to address a high pile-up environment. The new trigger system consists of two parts [32]. The first-level trigger (L1), consisting of fast custom-made electronics, determines a region of interest for each accepted L1 objects and effectively reduces event rates from $\sim$40 MHz to $\sim$100 kHz based on information such as transverse momentum, angle, and even complicated quantities like missing transverse energy. The second layer, the High-Level Trigger (HLT), uses the offline program that makes use of the region-of-interest information or performs global reconstructions to reduce the event rates from $\sim$100 kHz to $\sim$1 kHz.

1.2.3 ATLAS data formats

Before presenting the types of ATLAS data formats, it is necessary to introduce the concept of Monte Carlo (MC) event generators. The purpose of event generators is to use particle physics theories to simulate and predict the output seen by the detectors, so that a direct comparison between theories and experimental results can be made. Current widely used general purpose MC event generators in the ATLAS experiment include PYTHIA [33], HERWIG [34] and SHERPA [35].

Different data formats are developed by the ATLAS group to improve the efficiency of data analysis. For the detector data, shown in the left branch of Fig. 1.1, the Analysis Data Object (xAOD [4]) is derived from the RAW detector data containing full information of all reconstructed particles. Depending on the analysis interest, a number of derived formats known as the Derived Analysis Data Objects (DxAOD) are made from xAOD files through three processes, skimming, slimming, and thinning, to reduce unnecessary information. Skimming removes events that fail

[4]For the LHC run 1, the abbreviation AOD is used. The *x* in the front is used to indicate that it is for the LHC run 2.

to pass some selection criteria, e.g. at least two muons. Slimming removes uninteresting objects, e.g. all electron objects for the cases where they are not needed, within events. Thinning removes unnecessary variables within an object. Though each DxAOD file is significantly smaller in size and can be directly used in the final analysis, it is more common to be reduced further into the ntuple format. A ntuple is tabular where each event consists of a few elements with each in form of a row of data storing, e.g., kinematics of the particles.

For the MC generated data shown in the right branch of Fig. 1.2, the initial output from the event generators needs to go through the ATLAS detector simulator using GEANT4 to produce HITS format [36]. Then, the HITS format storing simulated detector hits needs to be converted into the so-called RAW Data Objects (RDO) format, which is the same data format as the raw data retrieved from the detector. Simulated RDO data are then processed with the same reconstruction and derivation algorithms as RAW format. The simulated formats typically include the same information as detector data formats, but also contain the so-called truth level information, which records the true types of particles generated by the event generators.

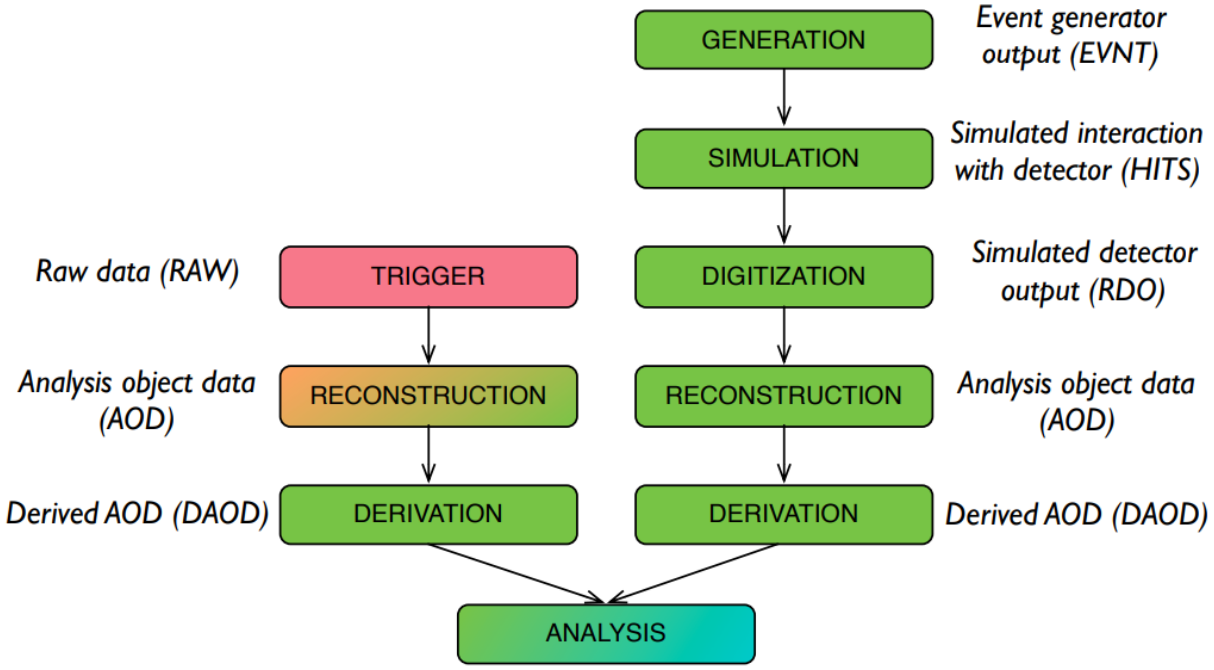

Fig. 1.2 Simplified flowchart of the ATLAS data flow with the left branch showing the detector data and the right branch showing the MC generated data. The plot is adopted from [2].

Chapter 2

Same-sign hadronic tau leptons

After the theoretical background of the doubly charged Higgs boson and the ATLAS detector being established in the previous chapter, the topic of this thesis can be formulated. In this chapter, I will first introduce the previous experimental search for doubly charged Higgs bosons decaying to electrons and muons by the ATLAS group, which leads to a discussion on the physics related to the τ-lepton. After that, some details for the current search using the same-sign hadronic tau channel will be presented. Finally, three background processes for this search will be described and I will point out the particular background of interest in this thesis work: the charge flip background.

2.1 Previous search for $H^{\pm\pm}$ by the ATLAS SSDiLep group

Doubly charged Higgs bosons can be produced from proton-proton collisions through a few processes. In Fig. 2.1, the production channels which produce a pair of doubly charged Higgs bosons are shown, where the Drell-Yan pair production process is the dominant process. The two photon fusion processes contribute approximately 10% of that from Drell-Yan process when the collision energy is 13 TeV at the LHC [37]. The cross-section of the weak boson fusion process is proportional to v_Δ so that its contribution is negligible for collider search since v_Δ is required to be small to agree with the smallness of neutrino masses.

Experimental search for the doubly charged Higgs bosons typically considers their decay into a pair of same-sign leptons [3] or a pair of same-sign W bosons [38]. The partial decay widths of $H^{\pm\pm}$ into leptons and WW are given by [3, 37]

$$\begin{aligned}
&\Gamma(H^{\pm\pm} \to l^\pm l'^\pm) = (1+\delta_{ll'})\frac{h_{ll'}^2 m_{H^{\pm\pm}}}{16\pi} \propto \frac{m_{H^{\pm\pm}}}{|v_\Delta|^2},\ \delta_{ll'} = \begin{cases} 1 & l = l' \\ 0 & l \neq l' \end{cases}, \text{ and} \\
&\Gamma(H^{\pm\pm} \to W^\pm W^\pm) \approx \frac{g_1^4 |v_\Delta|^2}{32\pi}\left(\frac{8}{m_{H^{\pm\pm}}} + \frac{m_{H^{\pm\pm}}^3}{m_W^4}\right) \propto |v_\Delta|^2\left(\frac{1}{m_{H^{\pm\pm}}} + m_{H^{\pm\pm}}^3\right),
\end{aligned} \tag{2.1}$$

where in the Higgs triplet model, the expression of $h_{ll'}$ comes from rearranging Eq. (1.19), leading to $h^2_{ll'} = (m_\nu^{ll'})^2/2|v_\Delta|^2$. It is easy to see that $\Gamma(H^{\pm\pm} \to l^\pm l'^\pm)$ completely dominates for small v_Δ value unless $m_{H^{\pm\pm}}$ is extremely massive such as $m_{H^{\pm\pm}} = 1/|v_\Delta|^2$, which gives $\Gamma(H^{\pm\pm} \to l^\pm l'^\pm) \approx \Gamma(H^{\pm\pm} \to W^\pm W^\pm)$.

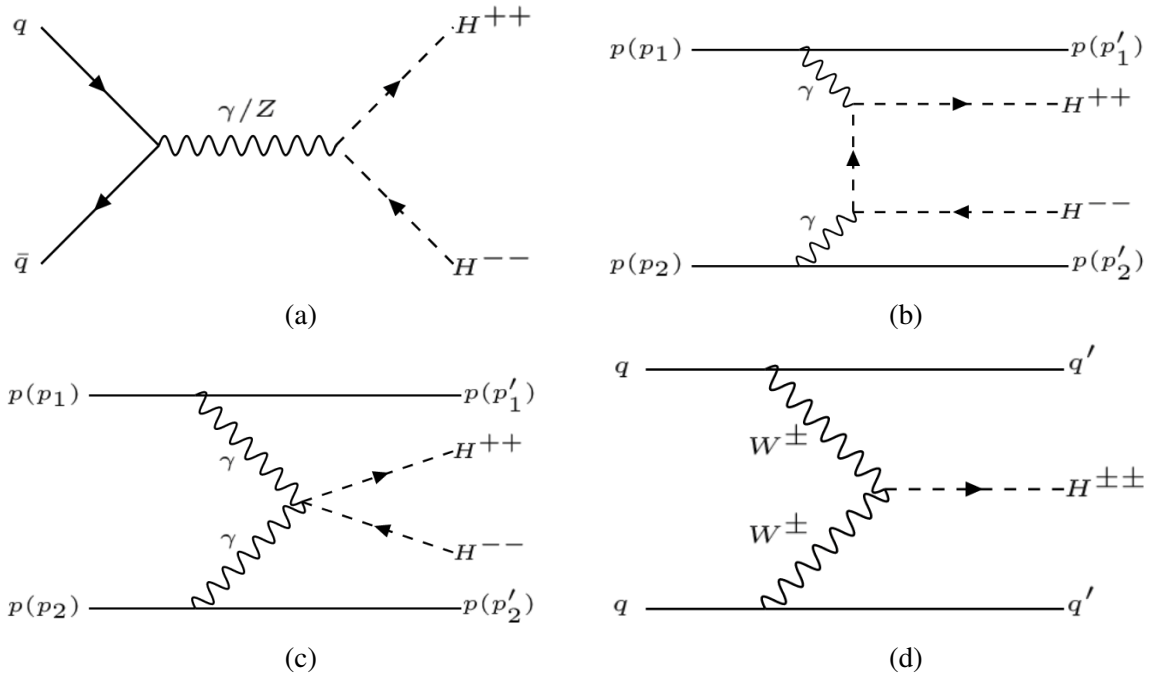

Fig. 2.1 Feynman diagrams of the production channels of $H^{\pm\pm}$: (a) Drell-Yan pair production, (b) and (c) two photon fusion processes, (d) weak boson fusion process.

In the previous analysis by the ATLAS SSDiLep group, the two photon fission channel and the weak boson fusion channel were assumed to be negligible; therefore the Drell-Yan process was considered to be the only production channel [3]. The decay signal of interest is the same-sign dilepton from each of the two doubly charged Higgs bosons. It should be noted that only electron and muon were considered, specifically $H^{\pm\pm} \to e^\pm e^\pm$, $e^\pm \mu^\pm$, $\mu^\pm \mu^\pm$. As electrons and muons are reconstructed very well by the ATLAS detector, a clear resonance peak in the invariant mass spectrum that is not predicted by the Standard Model would be observed at the mass of $H^{\pm\pm}$. The tree level Feynman diagram of the whole process is shown in Fig. 2.2. The total assumed branching ratio of $H^{\pm\pm}$ is

$$\mathrm{Br}(H^{\pm\pm} \to l^\pm l'^\pm) + \mathrm{Br}(H^{\pm\pm} \to X) = 100\% \tag{2.2}$$

where $l, l' = e, \mu$ and X is any other final states. With the increase of the branching ratio of $H^{\pm\pm} \to l^\pm l'^\pm$, the lower limits on the mass of a potential $H^{\pm\pm}$ particle also increase. It was concluded that the lower limits on the mass of doubly-charged Higgs bosons with $\mathrm{Br}(H_L^{\pm\pm} \to l^\pm l^\pm) = 100\%$ vary between 770 and 870 GeV for the $H_L^{\pm\pm}$ mass and between 660 and 760

GeV for the $H_R^{\pm\pm}$ mass, while the limits reduce to 450 GeV ($H_L^{\pm\pm}$) and 320 GeV ($H_R^{\pm\pm}$) for $\mathrm{Br}(H_L^{\pm\pm} \to l^{\pm} l^{\pm}) = 10\%$.

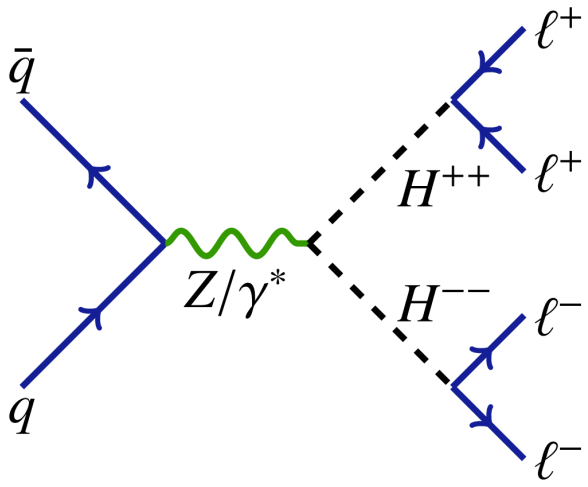

Fig. 2.2 Leading order Feynman diagram of the Drell-Yan pair production process and final states of interest [3].

2.2 τ-lepton related physics

The τ-lepton is the heaviest lepton ($m_\tau = 1776.85$ MeV) in the lepton family which has a short lifetime of 2.9×10^{-13} s [39]. This means that τ decays almost immediately after being produced and does not leave a detectable track in the ATLAS detector. The determination of τ is, therefore, based on its decay products, which can be classified into two categories: leptonic decay and hadronic decay modes, shown in self-explanatory Fig. 2.3a and 2.3b, respectively.

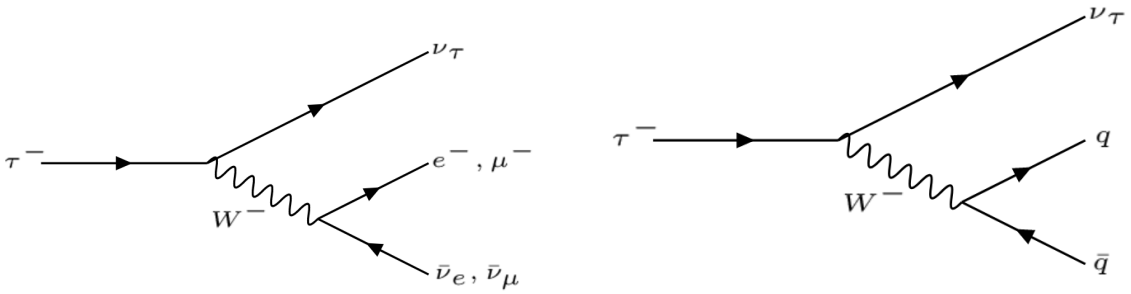

(a) (b)

Fig. 2.3 Feynman diagrams of leptonic (left) and hadronic (right) τ decay.

The quark-antiquark pair from the hadronic τ decay will eventually form hadrons due to colour confinement, a phenomenon that isolated colour charged particles, such as quarks and

gluons, cannot be observed. Depending on the number of charged particles in the final state, *1-pronged* modes and *3-pronged* modes refer to the final state with one and three charged particles, respectively. The most common decay modes of τ and corresponding branching ratios along with the notations are summarised in table 2.1. There is one extra notation used in this thesis: $\tau_{\text{had-vis}}$, which denotes τ_{had} without the tau neutrino ν_τ.

Decay mode	Branching ratio [%]	Notation
All leptonic modes	35.2	τ_{lep}
$\tau \to \nu_\tau e \nu_e$	17.8	τ_e
$\tau \to \nu_\tau \mu \nu_\mu$	17.4	τ_μ
All hadronic modes	64.8	τ_{had}
All 1-pronged modes	50.0	$\tau_{\text{1-pronged}}$
$\tau \to \nu_\tau q\bar{q} \to \nu_\tau \pi^\pm$	10.8	/
$\tau \to \nu_\tau q\bar{q} \to \nu_\tau \pi^\pm \pi^0$	25.5	/
$\tau \to \nu_\tau q\bar{q} \to \nu_\tau \pi^\pm 2\pi^0$	9.26	/
All 3-pronged modes	14.6	$\tau_{\text{3-pronged}}$
$\tau \to \nu_\tau q\bar{q} \to \nu_\tau \pi^\pm \pi^\pm \pi^\mp$	8.99	/
$\tau \to \nu_\tau q\bar{q} \to \nu_\tau \pi^\pm \pi^\pm \pi^\mp \pi^0$	2.79	/

Table 2.1 Summary of common decay modes of τ and corresponding branching ratios. The notations used throughout this thesis are listed in the rightmost column. There is no specific notation for each channel in 1-pronged and 3-pronged modes.

2.3 Search for $H^{\pm\pm} \to \tau^\pm_{had}\tau^\pm_{had}$

In the existing theoretical models, there is no constraint to prevent doubly charged Higgs bosons from decaying to a pair of same-sign τ-leptons. In addition, the couplings between the $H^{\pm\pm}$ and three charged leptons are commonly assumed to be proportional to the mass of the lepton, such as in Eq. (2.1), implying that the decay width of the ditau channel is higher than that of dielectron and dimuon. Therefore, there are good reasons to include τ-leptons in the analysis to increase the statistics. It should be noted that the leptonic tau modes are already included in the previous light lepton analysis since the ATLAS detector is unable to distinguish whether the light lepton is a prompt lepton (the lepton directly from the hard scattering) or a non-prompt lepton (the lepton from a leptonic tau decay). In other words, the leptonic tau modes are reconstructed as electrons and muons in the detector. Only the hadronic tau modes are of interest in this analysis.

2.3.1 Reconstruction and identification of hadronic decay $\tau-$leptons

The reconstruction and identification of hadronic τ is a particularly challenging task which is constantly under improvement. The reason for this being challenging is that the decay products of the τ-lepton can resemble hadronic jets, which appear almost everywhere in the proton-proton collision due to QCD interactions. In this subsection, I describe the procedures based on the latest official documents on the "Tau Recommendations for Release 21" TWiki page [40, 41].

The reconstruction of hadronic tau, specifically referring to the visible part $\tau_{\text{had-vis}}$, is the procedure to associate the tracks seen by the detector to the decay products of each hadronic tau. First, the seeds of hadronic taus are selected from jets constructed using the anti-k_t algorithm (see [42]) with a distance parameter $R = 0.4$ followed by requiring $p_T^{\text{jet}} > 10$ GeV and $|\eta| < 2.5$. This is followed by the tau vertex association since the tau vertex does not necessarily correspond to the chosen primary vertex due to multiple interactions at the same time. The association algorithm sums the p_T of tau candidate tracks within the cone size of $\Delta R = 0.2$ around the jet seed direction and matches it to the primary vertex in agreement with the p_T sum. The tau candidate tracks consist of π^0 and charged hadrons, $\pi^{\pm}$, which are reconstructed using complicated techniques involving the help of Boost Decision Tree[1] (BDT) (see e.g. [40] for more details). Depending on the number of reconstructed $\pi^{\pm}$ tracks and the number of π^0's determined by the calorimeter, the hadronic tau can be classified into different decay modes as listed in table 2.1.

However, the reconstruction process does not reliably distinguish hadronic taus from the jet background. The identification of $\tau_{\text{had-vis}}$ is dedicated to distinguishing true hadronic taus among all of the reconstructed hadronic taus using a BDT. A list of discriminating variables regarding the kinematics of each tau candidate are fed into the BDT algorithm as inputs and a score is produced as output which indicates how $\tau-$like the candidate is. Two separate BDT algorithms are trained for 1-pronged and 3-pronged $\tau_{\text{had-vis}}$ events using MC simulated samples so that the truth information of particles is known. Specifically, the $Z/\gamma^* \to \tau\tau$ and di-jet samples are used as training samples to simulate signals and jet background, respectively. The output from the training sets can be compared with the truth information to optimise the BDT. Then, the trained BDT can be used to run on detector data and other MC simulated samples to reject low-scoring jet candidates and accept high-scoring candidates as true hadronic taus. Four Jet ID working points are provided, corresponding to various ID efficiencies for 1-pronged and 3-pronged hadronic taus, as summarised in table 2.2. However, it should be noted that even with the tight working point, the identification efficiency for $\tau_{\text{had-vis}}$ is still quite low as we will show in Chapter 4.4.

[1] A machine learning technique for decision making, e.g. classifying the types of particles, based on a series of input parameters.

Jet ID working points	ID efficiency	
	1-prong	3-prong
JETIDBDTVERYLOOSE	95%	95%
JETIDBDTLOOSE	85%	75%
JETIDBDTMEDIUM	75%	60%
JETIDBDTTIGHT	60%	45%

Table 2.2 ID efficiency for 1-pronged and 3-pronged hadronic taus at different working points [7].

2.4 Same-sign dilepton Standard Model Background

One of the most important parts in an experimental search for a new particle is to eliminate the contamination of the Standard Model background in the final signal region. The background is typically estimated using various techniques in the so-called control regions chosen to be orthogonal to the signal region. In the case of doubly charged Higgs boson, theoretically speaking the Standard Model background is rare because most of the possible background channels from the Standard Model involve missing energy due to neutrinos from the electroweak interaction [24]. However, the detector is far from perfect so that the final states with the possibility of giving same-sign lepton signature are considered as the background. There are three main sources of background: prompt, non-prompt and charge flip.

2.4.1 Prompt background

The prompt (a.k.a irreducible) background mainly consists of prompt same-sign leptons originating from the direct products of some Standard Model decay including diboson ($W^{\pm}W^{\pm}$, ZZ, WZ) and $t\bar{t}X$ processes ($t\bar{t}W$, $t\bar{t}Z$ and $t\bar{t}H$). Since the ATLAS detector is unable to distinguish the exact vertices of the leptons, these processes may be misreconstructed as either one or two pairs of same-sign τ-leptons which emulate the decay signals of $H^{\pm\pm}$. Background contributions from prompt leptons are estimated using MC simulation. Two examples of the leading order process are shown in Fig. 2.4 with one corresponding to ZZ/WZ and the other one corresponding to $t\bar{t}W$. The predominant prompt background process for the four-lepton final state leading to two pairs of same-sign leptons is

$$q\bar{q} \rightarrow ZZ \rightarrow l^{\pm}l^{\mp}l^{\pm}l^{\mp}, \tag{2.3}$$

which has a measured production cross-section of $46.2^{+2.5}_{-2.3}$ fb at $\sqrt{s} = 13$ TeV when only electrons and muons are considered [43]. Since the ZZ channel does not have missing momentum

originated from neutrinos, it has the identical final state as same-sign dilepton signal from a pair of the $H^{\pm\pm}$. However, such background can be distinguished as the resonance mass peak

The WZ channel, with a measured cross-section of 63.7 ± 4.7 fb using electron and muon final states at $\sqrt{s} = 13$ TeV [44], is possible to be reconstructed as a pair of same-sign leptons if the charged lepton from W boson is combined with one of the leptons with same charge from Z boson decay, such as

$$q\bar{q} \to ZW^{\pm} \to l^{\pm}l^{\mp}l^{\pm}\nu_l. \tag{2.4}$$

The last diboson channel is the WW channel, such as

$$q\bar{q} \to q\bar{q} + W^{\pm}W^{\pm} \to q\bar{q} + l^{\pm}\nu_l l^{\pm}\nu_l, \tag{2.5}$$

which has a cross-section of 379.1 ± 38.4 fb measured using $WW \to e^{\pm}\nu\mu^{\mp}\nu$ channel at $\sqrt{s} = 13$ TeV [45].

The $t\bar{t}X$ channels include

$$\begin{aligned} q\bar{q} &\to t\bar{t}Z \to l^{\pm}\nu_l l^{\mp}\nu_l l^{\pm}l^{\mp} + \text{2b-jets} \\ q\bar{q} &\to t\bar{t}W \to l^{\pm}\nu_l l^{\mp}\nu_l l^{\pm}\nu_l + \text{2b-jets} \\ q\bar{q} &\to t\bar{t}H \to l^{\pm}\nu_l l^{\mp}\nu_l l^{\pm}l^{\mp} + \text{2b-jets}, \end{aligned} \tag{2.6}$$

which can also give rise to one or two pairs of same-sign leptons. The cross-sections for the first two channels were typically measured using the electron and muon final state, which are $\sigma_{ttZ} = 0.95 \pm 0.18$ pb and $\sigma_{ttW} = 0.87 \pm 0.27$ at $\sqrt{s} = 13$ TeV according to the latest results from the ATLAS group [46]. The $t\bar{t}H$ channel has a much lower contribution since the total production cross-section was measured to be $\sigma_{ttH} = 0.67 \pm 0.2$ pb at $\sqrt{s} = 13$ TeV [47]. The b-jets in the final state can be used to identify the $t\bar{t}X$ channels from diboson channels.

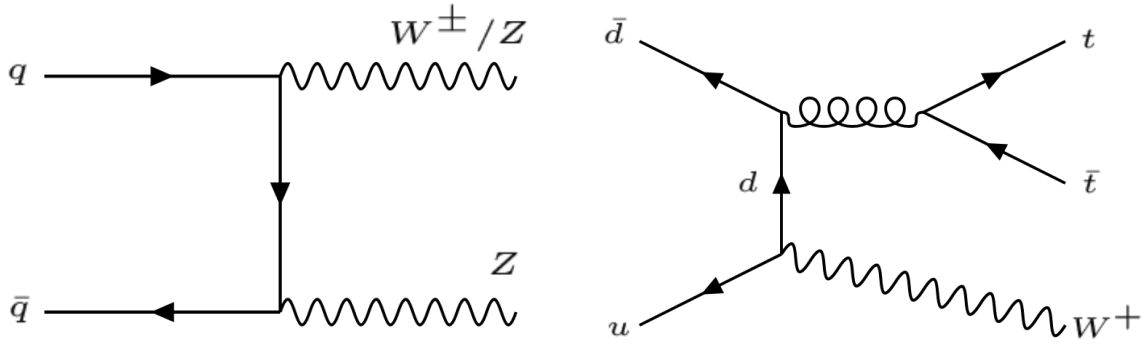

(a) (b)

Fig. 2.4 Two example leading order Feynman diagrams of ZZ/WZ and $t\bar{t}W$ process as prompt background.

2.4.2 Non-prompt background

The non-prompt (a.k.a fake) background consists of two parts: leptons originated from the secondary decay of other particles and other physics objects (especially hadron jets in this case) misidentified as leptons.

The first part corresponds to the same decay processes for all charged leptons due to lepton universality. Specifically, the decay of hadrons gives rise to charged leptons (as shown in Fig. 2.5 for the case of τ-lepton) which leave tracks and hits in the relevant parts of the detector as would a prompt lepton.

The second part contributes differently to the non-prompt background depending on the flavour of the charged lepton since distinct leptons are reconstructed using different parts of the detector and techniques. MC samples are not used to provide an estimation of this background due to large uncertainties in the QCD jets and hadronisation simulation [3]. In the case of hadronic τ-lepton, the quark and gluon jets are two sources to give rise to the same jet signature as a hadronic tau jet. In most of the events, a typical hadronic tau jet is more collimated and has a lower particle multiplicity, as shown in Fig. 2.6. Such signatures can be exploited to reduce the quark and gluon jets background. The current ongoing study within the SSDiLep group uses the multijet and V+jet samples to study the origins of tau fakes. By looking at the differences in some key parameters (e.g. jet width), the multijet and V+jets events are known to have a low quark/gluon ratio and a high quark/gluon ratio, respectively, which means that the multijet sample is dominated by gluon-oriented tau fakes while the V+jets sample is dominated by quark-oriented tau fakes.

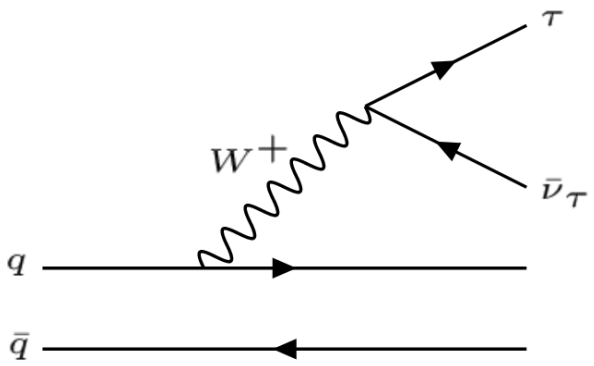

Fig. 2.5 The Feynman diagram illustrating τ-leptons originating from the decay of hadronised quarks as non-prompt background.

(a) (b)

Fig. 2.6 Comparison of the typical signature of a QCD (left) and a hadronic (right) tau jet. The plot is adopted from [4].

2.4.3 Charge-flip background

The charge of a particle is determined using the curvature of the track when it travels through the tracking detector surrounded by the magnetic field. The charge-flip background corresponds to the misidentification of the sign of the charge of prompt leptons by the ATLAS detector due to limited detector resolution. This means that the events with a pair of opposite-sign leptons may be regarded as a same-sign signal if one lepton has its charge misidentified. In this subsection, I will first describe the previous study on the charge-flip of electrons and muons by the SSDiLep group [28, 48]. Then, I will introduce the charge-flip background of hadronic τ-lepton which is the focus of this entire thesis work.

Electron charge misidentification

For electrons, the electric charge is determined from the curvature of the best matched track associated to the primary electron. The misidentification of the charge of electrons gives rise to the largest background. Using the truth information from simulated $Z \to e^+e^-$ samples, the scenario of electron charge identification can be classified into four types:

1. correctly matched track and charge;
2. correctly matched track but wrong charge;
3. wrong matched track and wrong charge;
4. wrong matched track but correct charge.

The first type represents the purest prompt electrons that the best-matched track is correctly associated with the prompt electron. Electrons with the correct track but wrong charge (stiff tracks) indicate the difficulties in determining the curvature of the prompt electron track. This can be a result of the track with high p_T which makes the bending less significant by the magnetic field in a limited region, resulting in a straight trajectory with ambiguous curvature for

determining the charge. Also, the lack of sufficient SCT hits leads to difficulties in calculating the curvature as well. Therefore, the charge-flip rates of electrons are expected to depend on p_T. The most of the stiff track events are found in the region $2.2 < |\eta| < 2.5$, where only the SCT end-cap region is available for measuring the curvature of the track as shown in Fig. 2.7.

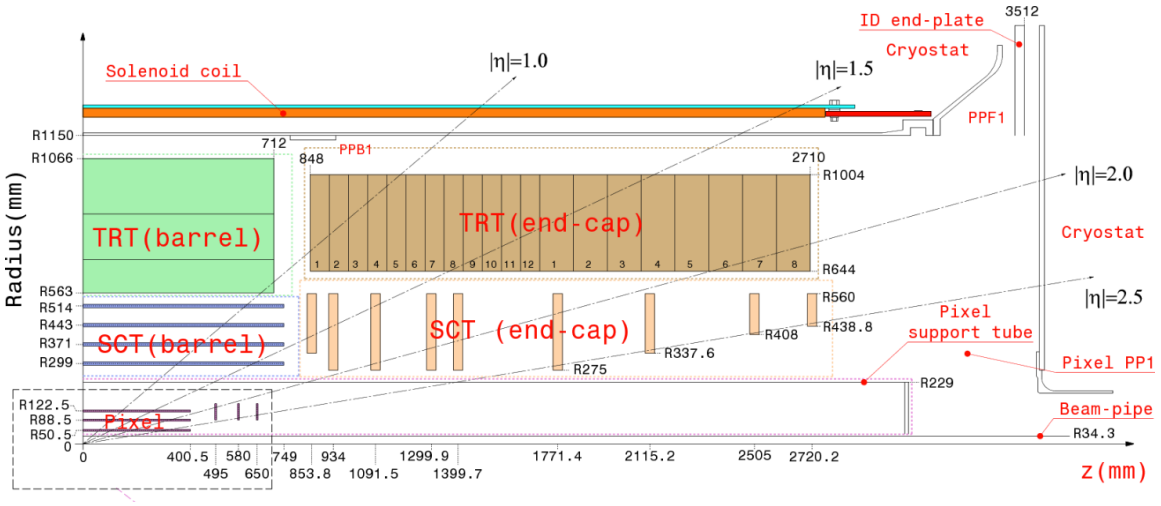

Fig. 2.7 Plan view of ATLAS inner detector [5].

Electrons with wrong track and wrong charge are called trident events. As an electron travels through the detector material, it experiences deacceleration from the Coulomb field of nucleus which leads to emission of bremsstrahlung radiations. The emitted photon can further convert into an electron-positron pair, leading to a more-or-less random chance of which track is chosen to reconstruct the charge of the prompt electron. If it happens to give the correct charge from the wrong matched track, it corresponds to the fourth type.

The famous study on bremsstrahlung radiation by Bethe and Heitler showed that the cross-section of energy loss of fast-moving particles (primary energy $E_0 \ll mc^2$) due to radiation is proportional to the square of nuclear charge, Z, of the absorber [49], given as

$$\sigma \sim \frac{Z^2}{137}\left(\frac{e^2}{mc^2}\right)^2. \tag{2.7}$$

The average rate of electron energy loss through bremsstrahlung radiation depends considerably on the amount of material traversed. Consequently, the charge-flip rate is expected to depend on pseudorapidity, η, due to the cylindrical geometry of the detector. It was found that most electrons categorised as trident events are found in the region $1.5 < |\eta| < 2.2$, which corresponds to the part with vast inactive material.

Three methods (direct extraction, tag-and-probe and data-driven method) were used to estimate the charge-flip rates of electrons and cross-check with each other. The details of the tag-and-probe and data-driven method will be presented in the following chapters for the charge-flip

rates of hadronic τ-leptons. Here, the result of the nominal charge-flip rate from the data-driven method is shown in Fig. 2.8. Note that in the data-driven method, the charge-flip rate, denoted as ε, is assumed to depend on p_T and η, but these two variables are uncorrelated, meaning that

$$\varepsilon(\eta, p_T) = \sigma(p_T) \times f(\eta), \tag{2.8}$$

where $\sigma(p_T)$ and $f(\eta)$ are single-variable functions of p_T and η respectively.

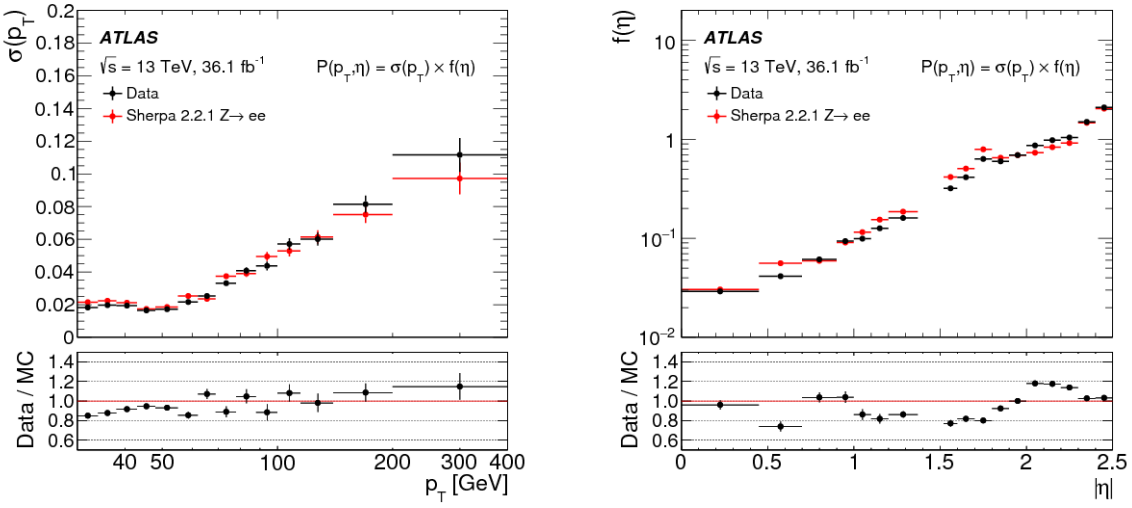

(a) (b)

Fig. 2.8 The nominal charge flip rate $\sigma(p_T)$ (left) and $f(\eta)$ (right) of electron estimated using the data-driven method. The plot is adopted from [3].

The charge-flip rates of electrons were tested by applying it to the opposite-sign samples to check for the agreement with same-sign mass resonance peak, as shown in Fig. 2.9.

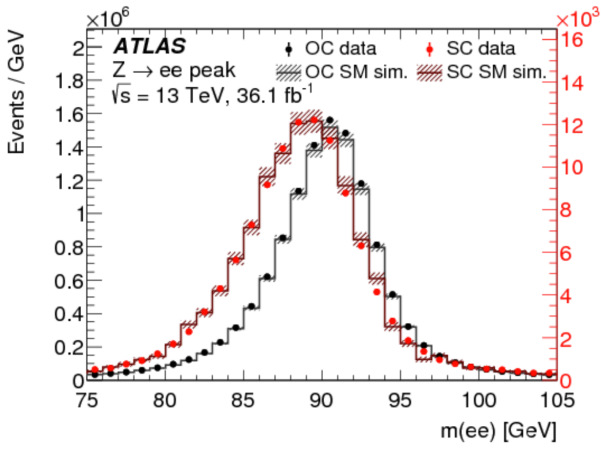

Fig. 2.9 Closure test of the electron charge-flip rate. The opposite-sign data and MC are multiplied by the estimated charge-flip rate. The plot is adopted from [3].

Muon charge misidentification

The muon charge is determined from the information of the track primarily from the Inner detector and the Muon Spectrometer. In order to measure the curvature of a curve, at least three points in space are required to obtain the sagitta, which is defined as the distance from the midpoint of a circular arc to the centre of its chord. The Muon Spectrometer consists of three layers known as the inner, middle and outer station, which is able to provide at least three measurements at each station for a muon. Together with the measurement from the Inner detector, the curvature measurement is a lot more precise due to a much longer lever arm. In addition, muons undergo bremsstrahlung much more rare than electrons due to a much higher mass. Therefore, the muon charge misidentification rate is negligible, which was proven by the previous study [28, 48].

Hadronic τ-lepton charge misidentification

In the case of hadronic τ-leptons, the charge is identified through the sum of charged tracks from its decay products [40]. This is a more complicated situation as the hadronic tau jet usually has many collimated tracks leading to mismatch to the prompt tracks from the τ-lepton. In addition, the neutral pions appearing in the decay products decay to a pair of photons almost all the time, followed by around half of the photons further convert into electron-positron pairs. This is similar to the trident event as mentioned previously. Therefore, the dependence of the charge-flip rate on η is anticipated. As the sum of the p_T of each track only needs to equal to the p_T of the prompt τ-lepton, the distribution of p_T of each track is strictly constrained. It is reasonable to expect a much weaker dependence between the charge-flip probability and p_T for hadronic τ-leptons in comparing to electrons.

In the following two chapters, I will present the study of the hadronic τ-lepton charge misidentification rate for MC samples and detector data respectively. The data-driven and tag-and-probe method are adopted from the previous study of electrons and applied to MC samples. A new method known as the template fit method is designed to extract the charge-flip probability for detector data. The cause of the charge-flip is briefly studied and the method and the results are presented in Appendix B.

Chapter 3

Charge-flip rate for Monte Carlo simulated samples

3.1 Data-driven

3.1.1 Method

The description of the data-driven approach is based on [28, 48]. The name "data-driven" is adopted from the previous convention, but it is more appropriate to call it the likelihood charge-flip estimation method because this method is essentially a maximum likelihood method. Also, the name "data-driven" may imply the use of detector data, while it only works for MC samples in the case of τ_{had} because of large fake tau background.

The charge-flip events are assumed to be the same-sign τ_{had} pair events observed in the decay processes such as $Z \to \tau^+_{\text{had}}\tau^-_{\text{had}}$ and $t\bar{t} \to \tau^+_{\text{had}}\tau^-_{\text{had}}\nu_\tau\bar{\nu}_\tau + 2\text{b-jets}$, where the true final states must be a pair of opposite-sign τ-leptons. Each charge-flip event is assumed to be independent of each other. The probability function $P(N^{ij}_{SS}|\lambda_{ij})$, which describes the chance of observing N^{ij}_{SS} same-sign pairs given the expected number of charge-flipped events λ_{ij}, follows a Poissonian distribution

$$P(N^{ij}_{SS}|\lambda_{ij}) = \frac{\lambda_{ij}^{N^{ij}_{SS}} e^{-\lambda_{ij}}}{N^{ij}_{SS}!}, \tag{3.1}$$

where i and j represent the leading and sub-leading τ-lepton respectively. As mentioned previously in section 2.4.3, the charge-flip probability in the data-driven method is two-dimensional represented on the grid of p_T and η. For example, if p_T has 3 bins and η has 2 bins, the charge-flip probability has 6 values corresponding to different permutation of p_T and η. This is hidden in the symbol i and j, as each index denotes a two-dimensional bin $(p_{T_{i/j}}, \eta_{i/j})$ recording the transverse momentum and pesudorapidity of the leading and sub-leading τ-lepton. The choice of the p_T and η binning affect the statistics of the results. A too narrow bin width will make

the maximisation of the likelihood function very unstable or fail to converge. The likelihood function is defined as the multiplication of the probability density

$$L(\boldsymbol{\lambda}|\mathbf{N}_{SS}) = \prod_{i,j} P(N_{SS}^{ij};\lambda_{ij}) = \prod_{i,j} \frac{\lambda_{ij}^{N_{SS}^{ij}} e^{-\lambda_{ij}}}{N_{SS}^{ij}!}, \tag{3.2}$$

where $\boldsymbol{\lambda}$ and $\mathbf{N}_{SS}$ are two vectors with $\boldsymbol{\lambda} = (\lambda_{11},...,\lambda_{1j_{\max}},\lambda_{21},...,\lambda_{2j_{\max}},...,\lambda_{i_{\max}j_{\max}})$ and $\mathbf{N}_{SS} = (N_{SS}^{11},...,N_{SS}^{1j_{\max}},N_{SS}^{21},...,N_{SS}^{2j_{\max}},...,N_{SS}^{i_{\max}j_{\max}})$.

In order to explain the meaning of the likelihood function, it is better to use a one-dimensional example. In Fig. 3.1, the orange dots along the horizontal axis represent the distribution of the measurements, such as the number of same-sign events N_{SS}. The red curve is the probability distribution peaked at the dashed vertical line. If the distribution is Possionian, the mean and the width is controlled by the parameter λ (the expected number of occurrences). The likelihood function is the product of the chance of observing the measurements based on the assumed probability distribution. We want the optimum value of λ which maximises the likelihood of observing the data we measured.

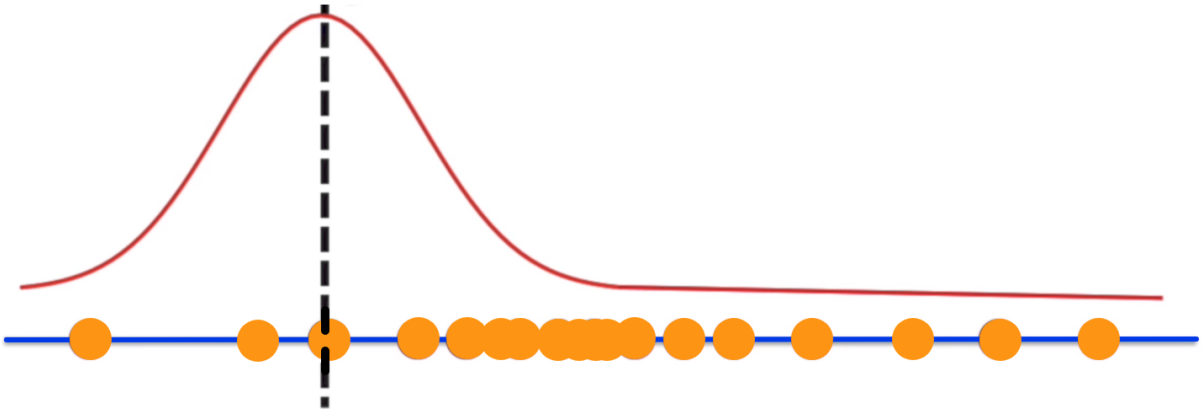

Fig. 3.1 A schematic diagram shows the relation among the probability distribution function, measured data and corresponding likelihood.

The likelihood function is usually quite complicated, leading to difficulties for the maximisation algorithm to converge. A trick to simplify calculations is to take the logarithm of the negative of the likelihood function, as it brings the parameter from an exponential form to a linear form and turns a maximisation process to a minimisation process

$$\begin{aligned} -l(\boldsymbol{\lambda}|\mathbf{N}_{SS}) &= -\ln(L(\boldsymbol{\lambda}|\mathbf{N}_{SS}) = -\ln\sum_{i,j}\frac{\lambda_{ij}^{N_{SS}^{ij}} e^{-\lambda_{ij}}}{N_{SS}^{ij}!} = -\sum_{i,j}\ln\left(\frac{\lambda_{ij}^{N_{SS}^{ij}} e^{-\lambda_{ij}}}{N_{SS}^{ij}!}\right) \\ &= -\sum_{i,j}\left(N_{SS}^{ij}\ln\lambda_{ij} - \lambda_{ij} - \ln(N_{SS}^{ij})\right). \end{aligned} \tag{3.3}$$

The expected number of charge flipped leptons is related to the charge-flip probability of main interest. The expression is simply based on the probability theory

$$\lambda_{i,j} = \varepsilon_i(1-\varepsilon_j)N_{AS}^{ij} + \varepsilon_j(1-\varepsilon_i)N_{AS}^{ij} = (\varepsilon_i(1-\varepsilon_j) + \varepsilon_j(1-\varepsilon_i))N_{AS}^{ij}, \tag{3.4}$$

where $N_{AS}^{ij} = N_{OS}^{ij} + N_{SS}^{ij}$ is the measured number of any-sign ditaus and $\varepsilon_{i/j}$ is the charge-flip probability of the leading and sub-leading τ_{had}, respectively. By substituting the expression of $\lambda_{i,j}$ into Eq. (3.3), the log-likelihood function can be expressed as

$$\begin{aligned} -l(\boldsymbol{\varepsilon}; \boldsymbol{N}_{SS}, \boldsymbol{N}_{AS}) &= -\sum_{i,,j} N_{SS}^{ij} \ln\left((\varepsilon_i(1-\varepsilon_j) + \varepsilon_j(1-\varepsilon_i))N^{ij}\right) - \left(\varepsilon_i(1-\varepsilon_j) + \varepsilon_j(1-\varepsilon_i)\right) N_{AS}^{ij} - \ln(N_{SS}^{ij}!) \\ &\approx -\sum_{i,,j} N_{SS}^{ij} \ln\left((\varepsilon_i(1-\varepsilon_j) + \varepsilon_j(1-\varepsilon_i))N^{ij}\right) - \left(\varepsilon_i(1-\varepsilon_j) + \varepsilon_j(1-\varepsilon_i)\right) N_{AS}^{ij}, \end{aligned} \tag{3.5}$$

where the constant term is dropped since it does not have any impact on the minimisation of the log-likelihood function. Same as the parametrisation of $\varepsilon(p_T, \eta)$ used for electrons, as shown in Eq. (2.8), the dependence of the charge-flip probability on p_T and η is assumed to be uncorrelated in order to reduce the parameter space. Moreover, one of the functions, such as $f(\eta)$ in our algorithm, is required to be normalised, which is achieved in the likelihood fit by adding an exterior penalty function

$$\alpha \left(\sum_{i=1}^{N_\eta} (f(\eta_i) \times \Delta\eta_i) - 1 \right)^2, \tag{3.6}$$

where α is the penalty coefficient with its value chosen to be on order of 10^6. If the integrated value of $f(\eta)$ deviates far from unity, a heavy penalty is going to be applied to the returned value so that the algorithm knows the parameters are far from the optimum values. In all, the number of free parameters in is $N_\eta + N_{p_T} - 1$. The likelihood function is minimised using the ROOT minimisation interface with the `Minuit2` package and `Migrad` algorithm [50].

In the previous study on electrons, other backgrounds in the invariant mass region (e.g. Z and $t\bar{t}$) are subtracted using the so-called sideband method. The idea of this method is to use the tail regions at two sides of the mass resonance peak to estimate other backgrounds, which means that the distribution of other background is assumed to be flat. Since the data-driven method only applies to MC samples in the case of hadronic τ-leptons, there is no need to apply the background removal procedure.

3.1.2 Data sets

Two ntuples with the SUSY3 derivation corresponding to $Z \to \tau\tau$ and $t\bar{t} \to \tau\tau$ are used in the analysis. The SUSY3 derivation has the following basic selections:

- at least 2 leptons, at least 1 tau;
- all tau trigger combinations (including light leptons), single electron and muon triggers.

In Fig. 3.2 and 3.3, the truth origins and truth types of the τ-leptons in the $Z \to \tau\tau$ and $t\bar{t} \to \tau\tau$ samples are shown. The truth origins with non-zero filling have following meaning: 0 = non-defined, 6 = Dalitz decay (a meson decay involving two leptons in the final state), 10 = top, 12 = W Boson, 13 = Z Boson, 23 = light mesons, 25 = charmed mesons, 26 = bottom mesons, 31 = strange baryon, 32 = charged baron and 33 = bottom baryon. The truth types with non-zero filling have following meaning: 0 = unknown, 2 = isolated electron, 3 = non-isolated electron, 4 = background electron, 6 = isolated muon, 7 = non-isolated muon, 8 = background muon, 10 = isolated tau and 11 = non-isolated tau. The truth origin or the truth type equalling to '0' mainly corresponds to the cases that the MC truth classification algorithm fails or there is no original vertex.

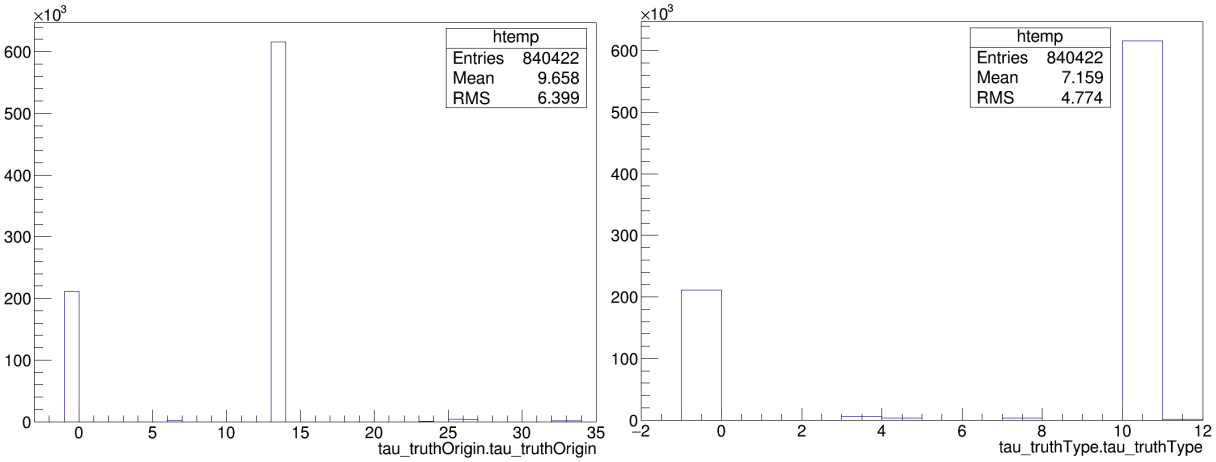

(a) (b)

Fig. 3.2 Truth origins (left) and truth types (right) in the $Z \to \tau\tau$ samples.

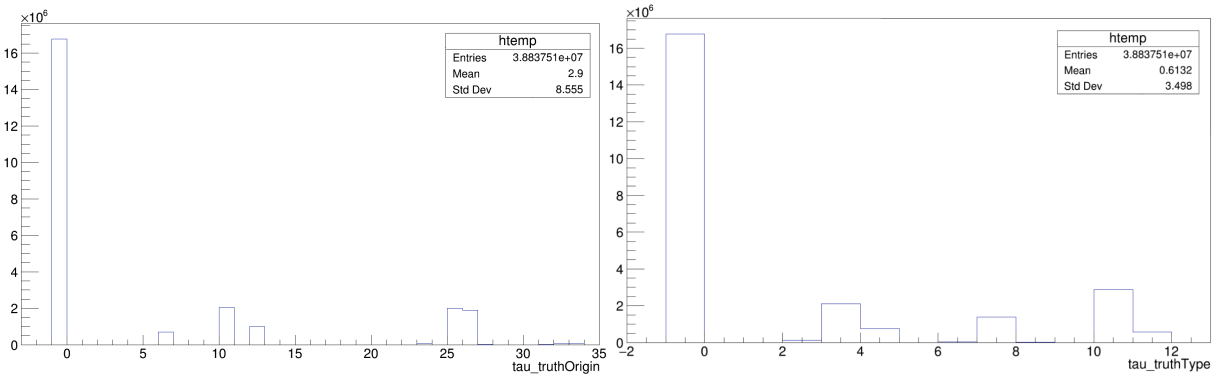

(a) (b)

Fig. 3.3 Truth origins (left) and truth types (right) of the τ-leptons in the $t\bar{t} \to \tau\tau$ samples.

3.1.3 Selections

The selections are summarised in table 3.1. The baseline selections apply to both samples: $Z \to \tau\tau$ and $t\bar{t} \to \tau\tau$. Depending on the processes we want to look at, the Z and $t\bar{t}$ control region is defined. In the case of MC study, the control regions are not so important because the samples already simulated based on the processes we are interested in. However, the control regions will be important when looking at detector data. In the ditau trigger name, the HLT objects are indicated as 'tau' with the digital number after it denoting the requirement on p_T and the 'medium' is the working point for the HLT BDT chosen at an efficiency of $\sim 95\%$ with respect to selected offline tau candidates. The L1 objects are denoted as 'TAU' and 'J' (jet) with the digits before these names indicating the multiplicity and digits after representing the energy requirement. In addition, 'IM' or 'I' refer to isolation requirement.

Type	Selections
Baseline	Ditau trigger: HLT_tau35_medium1_tracktwo_tau25_medium1_tracktwo _L1TAU20IM_2TAU12IM (2015) HLT_tau35_medium1_tracktwo_tau25_medium1_tracktwo (2016) HLT_tau35_medium1_tracktwo_tau25_medium1_tracktwo _L1DR-TAU20ITAU12I-J25 (2017) Two τ-leptons. Electron and muon veto Tau: $p_T > 30$ GeV, medium working point, isolated, ishadronic
Z control region	No extra cuts for MC samples
$t\bar{t}$ control region	At least one b-tagged jet

Table 3.1 Summary of the selections for the data-driven method.

3.1.4 Results

The dependence of estimated nominal charge-flip possibility on η and p_T are shown in Fig. 3.4. The results for $Z \to \tau\tau$ and $t\bar{t} \to \tau\tau$ agree well with each other. The charge-flip probability is weakly dependent on transverse momentm, while the dependence on pseudorapidity shares the same trend as $f(\eta)$ for electrons, as shown in Fig. 2.8b. The statistics of $t\bar{t}$ is worse than $Z \to \tau\tau$ samples, which is automatically calculated by the `Minuit2` package [50]. This could be resulted by the distribution of the mass resonance for $t\bar{t} \to \tau\tau$ being a lot wider than the Z boson mass resonance, which makes the peak signature less prominent and leads to more uncertainties in likelihood fit.

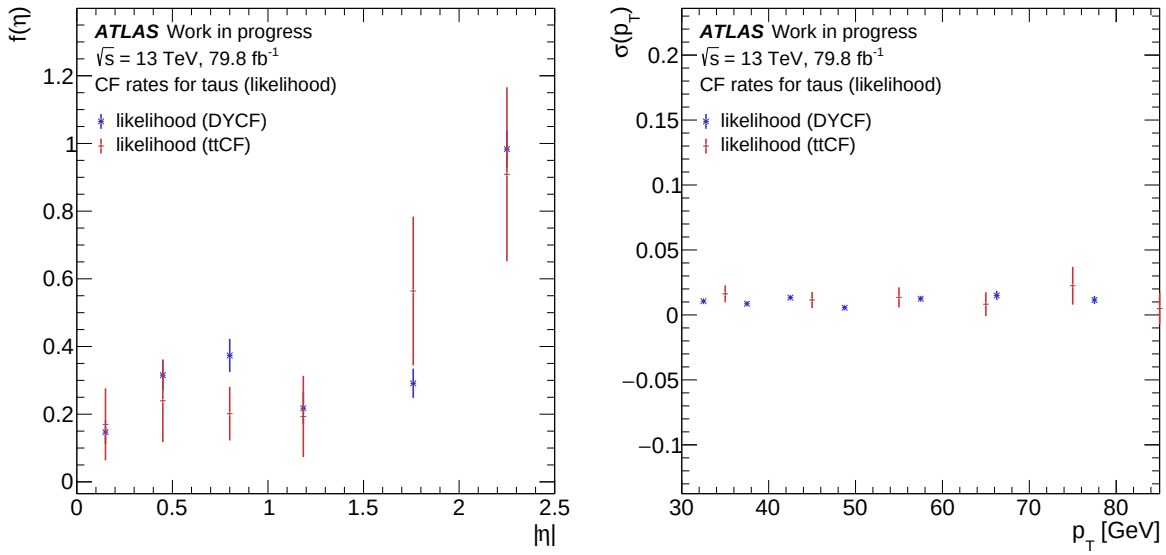

(a) (b)

Fig. 3.4 The nominal charge-flip rate estimated by the data-driven method. The blue and red points correspond to the result from $Z \to \tau\tau$ and $t\bar{t} \to \tau\tau$, respectively. The crack region (between the barrel and end-cap cryostats, including both material in front of the active layers and the whole thickness of the active calorimeter [6]), $1.37 < \eta < 1.52$, is excluded.

3.2 Tag-and-probe

3.2.1 Method

The tag-and-probe method is commonly used in many analyses in the ATLAS experiment. In the estimation of the charge-flip probability of the hadronic τ-leptons, one of the τ-leptons from either $Z \to \tau\tau$ or $t\bar{t} \to \tau\tau$ is required decay leptonically to a muon, since the charge of muon is known to be reliably reconstructed by the ATLAS detector. The charge misidentification rate of muons is assumed to be insignificant in comparing to that of τ_{had}. The muon is then chosen as the tag, which is used to test the correctness of the charge reconstruction of another τ-lepton known as the probe and the other τ-lepton is required to decay hadronically. In Fig. 3.5, the idea of the tag-and-probe method is illustrated using the $Z \to \tau\tau$ channel.

The charge-flip rate in the tag-and-probe method is chosen to be one-dimensional, meaning that it depends on either η or p_T. The charge-flip rate is calculated according to the following equation

$$\varepsilon_{\tau_{had}}(p_T/\eta) = \frac{N_{SS}(p_T/\eta)}{N_{AS}(p_T/\eta)}, \tag{3.7}$$

where $N_{AS}(p_T/\eta)$ and $N_{SS}(p_T/\eta)$ are the number of any-sign and same-sign $\tau_{\text{had}}\tau_{\mu}$ events in each p_T or η bin.

One can easily make the charge-flip rate two-dimensional by letting N_{SS} and N_{AS} be a record of the number of same-sign and any-sign events on the grid of p_T and η. But the number of bins dramatically increases from N_η or N_{p_T} to $N_\eta \times N_{p_T}$ so that the statistics of the results is greatly reduced. The results from this two-dimensional tag-and-probe method turn out to have very low statistics, especially that many bins away from the resonance peak have negative values due to negative weights in some MC events. Therefore, they are not presented as my final results.

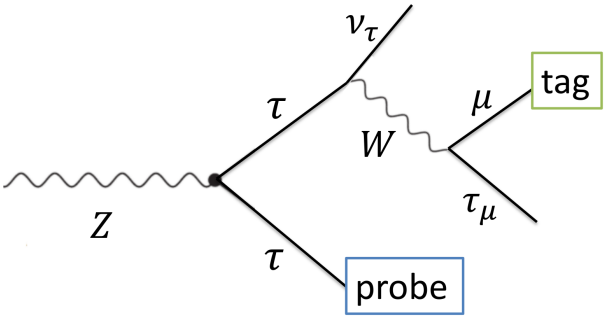

Fig. 3.5 The Feynman diagram of $Z \to \tau\tau$ illustrating the idea of the tag-and-probe method.

3.2.2 Data sets

The data sets used for the tag-and-probe method are exactly same as ones used in the data-driven method (see section 3.1.2).

3.2.3 Selections

Type	Selections
Baseline	Single muon trigger: HLT_mu20_iloose + HLT_mu50 (2015) HLT_muon26_ivarmedium + HLT_mu50 (2016-2017) One muon and one tau. Electron veto Muon: $p_T > 30$ GeV, medium working point, isolated, $z_0 \sin\theta < 0.5$, $d_0\text{sig} < 3.0$ Tau: $p_T > 30$ GeV, medium working point, isolated
Z control region	No extra cuts for MC samples
$t\bar{t}$ control region	At least one b-tagged jet

Table 3.2 Summary of the selections for the tag-and-probe method.

The selections are summarised in table 3.2. The single muon triggers are used to select events with one muon, followed by requiring one reconstructed τ-lepton passing the medium working

point. This turns out to be the most efficient way of selecting events with $\tau_\mu \tau_{\text{had}}$ final states. The available muon-tau triggers (e.g. `HLT_mu14_ivarloose_tau25_medium1_tracktwo`), which also serve the same purpose, end up passing fewer events.

3.2.4 Results

The dependency of the one-dimensional charge-flip rates on η and p_T are shown in Fig. 3.6. The results from $Z \to \tau_\mu \tau_{\text{had}}$ and $t\bar{t} \to \tau_\mu \tau_{\text{had}}$ agree well with each other. Again, the charge-flip probability depends weakly on transverse momentum but strongly on pseudorapidity. The dependence on η shares the same trend as $f(\eta)$ for electrons and hadronic τ-leptons in the data-driven method. The statistics of $Z \to \tau_\mu \tau_{\text{had}}$ samples is worse than $t\bar{t} \to \tau_\mu \tau_{\text{had}}$ samples due to the fact that the event numbers in the $t\bar{t}$ samples is a lot higher. Since the tag-and-probe method is essentially the division of the N_{SS} and N_{AS} histogram, a higher event number in each histogram naturally yields better statistics in the resulting histogram.

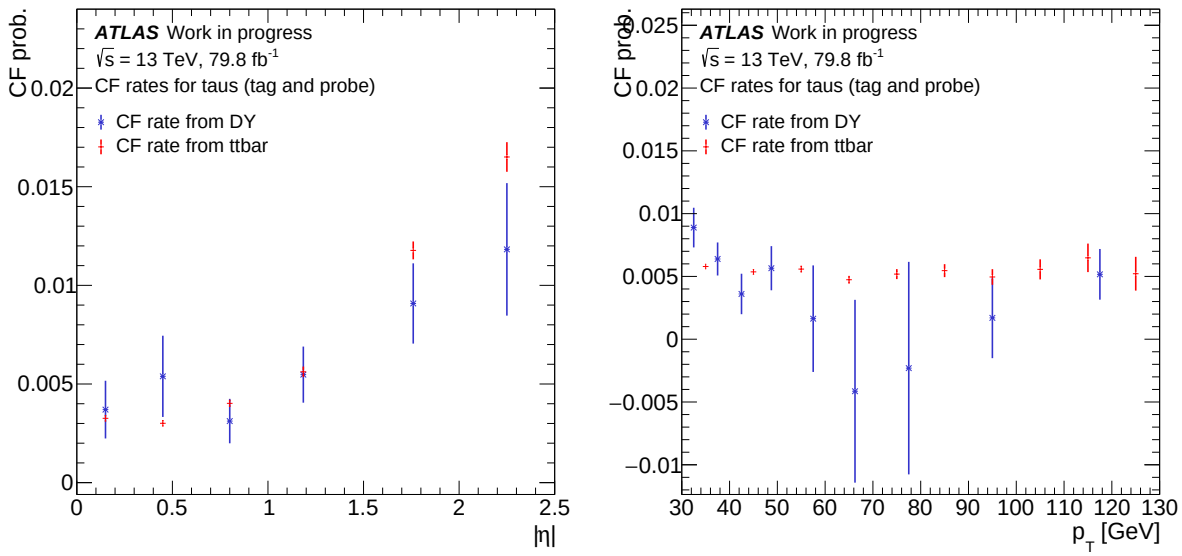

(a) (b)

Fig. 3.6 Charge flip rate estimated by the tag-and-probe method. The blue and red points correspond to the result from $Z \to \tau_\mu \tau_{\text{had}}$ and $t\bar{t} \to \tau_\mu \tau_{\text{had}}$, respectively. The crack region, $1.37 < \eta < 1.52$, is excluded.

It should be noted that in Fig. 3.6b, two data points for the $Z \to \tau_\mu \tau_{\text{had}}$ samples in the p_T range from 65 to 85 GeV have negative values and very large error bars. This is a result of the negative weights in the same-sign fill, which also result in large error bars. As an example, the value of the bin centred at $p_T = 68$ GeV in the same-sign histogram is -6.37 ± 11.19. This error bar is calculated using the `sumw2` option in ROOT **(author?)** [51], which is commonly used in estimating the statistical error of the histogram representing counts. The `sumw2` option calculates

the error for each bin according to

$$\text{error} = \left(\sum_i \text{weight}_i^2 \right)^{1/2}, \tag{3.8}$$

so that the negative weights reduce the magnitude of the value but still increase the error due to the square in the summation. Therefore, better treatment of some bins with large negative weights from MC simulation should be considered.

The one- and three-pronged hadronic taus are also investigated separately. This is achieved by separating the final state into two cases: $\tau_\mu \tau_{\text{1-pronged}}$ and $\tau_\mu \tau_{\text{3-pronged}}$. The results of the dependence of the charge-flip probability on η are plotted in Fig. 3.7 with the plot on the left and right showing the result from $Z \to \tau_\mu \tau_{\text{had}}$ and $t\bar{t} \to \tau_\mu \tau_{\text{had}}$ samples, respectively. The charge-flip probability of one-pronged τ_{had} is slightly higher than that of three-pronged τ_{had} especially at large η value.

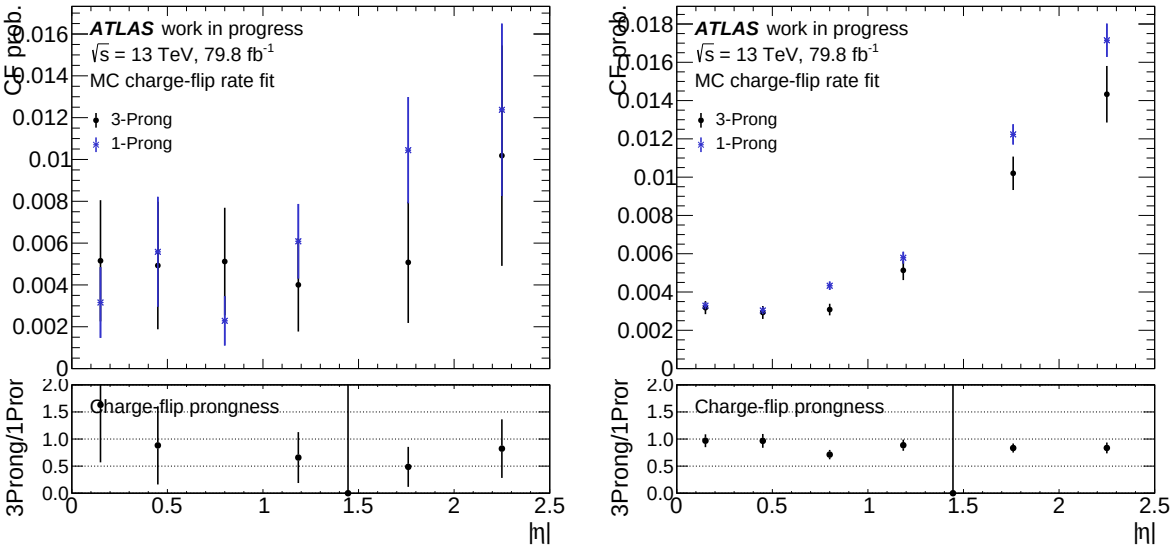

(a) (b)

Fig. 3.7 Charge flip rate vs. $|\eta|$ for 1-pronged (red) and 3-pronged (black) hadronic tau estimated by the tag-and-probe method. The figure on the left and right corresponds to $Z \to \tau_\mu \tau_{\text{had}}$ and $t\bar{t} \to \tau_\mu \tau_{\text{had}}$ samples, respectively. The crack region, $1.37 < \eta < 1.52$, is excluded.

The dependence of the charge-flip probability for one- and three-pronged τ-leptons on p_T is shown in Fig. 3.8. Only the results from the $t\bar{t} \to \tau_\mu \tau_{\text{had}}$ samples are presented because the $Z \to \tau_\mu \tau_{\text{had}}$ samples have too little statistics for the same-sign histogram to be separated to one- and three-pronged case. It can be clearly seen that the charge-flip rate is higher for one-pronged τ_{had} at p_T lower than around 110 GeV in comparing to three-pronged τ_{had}, while the data points at higher p_T have too little statistics to draw any conclusion.

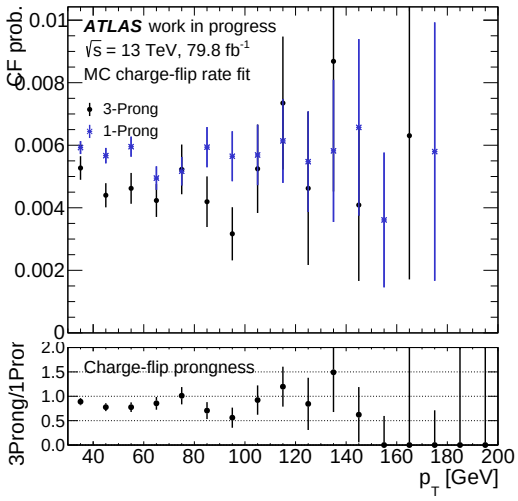

Fig. 3.8 Charge flip rate vs. p_T for 1-pronged (red) and 3-pronged (black) hadronic taus estimated by the tag-and-probe method using the $t\bar{t} \to \tau_\mu \tau_{\text{had}}$ samples.

3.3 Closure test

The validation of the estimated charge-flip rate is performed in a similar way as the electron charge-flip probability, as shown in Fig. 2.9. In general, the closure test shows that the estimated charge-flip rates are able to predict the same-sign distributions from any-sign distributions. More plots of the closure test on other variables are presented in Appendix A.

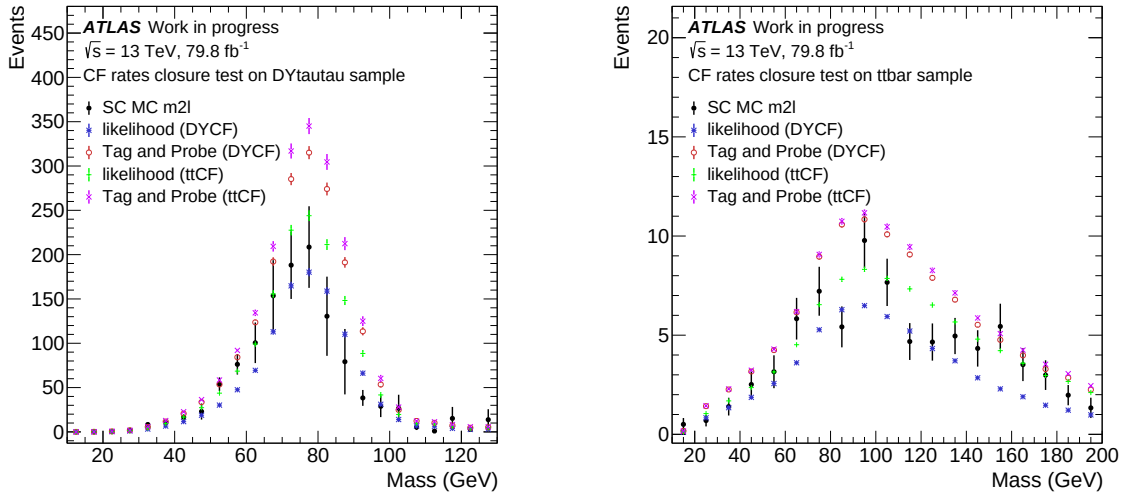

(a) (b)

Fig. 3.9 Closure test of the estimated charge-flip rates on ditau mass distribution. The legend "SC MC m2l" denotes the ditau mass distribution from same-sign MC samples. Other legends represent the prediction of the charge-flip rate from corresponding sample and method.

Chapter 4

Charge flip rate for ATLAS detector data

4.1 Motivation for template fit method

A new method is required to study the charge-flip rate for detector data. The motivation for this is that the identification efficiency of real hadronic τ-leptons is quite poor, leading to a huge fake tau background in the detector data. As shown in Fig. 4.1, the same-sign ditau visible mass ($\tau_{\text{had-vis}}$) distribution for detector data is roughly half of the magnitude of any-sign distribution. It is certainly unreasonable to have so many same-sign events which suggest that the data is heavily contaminated as the reconstruction and identification process pick up a lot of fake τ-leptons. Therefore, unlike electrons which has a much lower fake background, it is necessary to find a new method to extract the part of data that contains only true taus so that the charge-flip rate of real hadronic taus is measured.

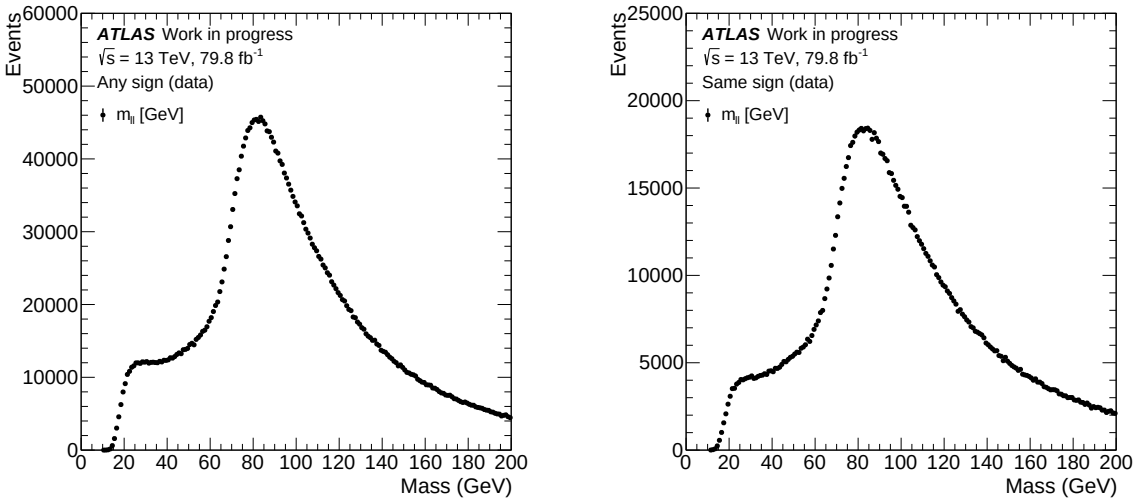

(a) (b)

Fig. 4.1 Any-sign (left) and same-sign (right) ditau visible mass ($\tau_{\text{had-vis}}$) distribution for the detector data in the Z control region defined in table 3.1.

4.2 Template fit method

The template fit method is commonly used in some ATLAS analysis such as measuring the mass of top quark. The general idea of this method is to make a comparison between discriminant distributions from data and Monte Carlo templates of the same distributions. In my study, the opposite- and same-sign data are decomposed into signal (real τ_{had}) and background (fake τ_{had}) part:

$$\begin{aligned} N^{OS}_{data}(\eta_i) &= N^{OS}_{signal}(\eta_i) + N^{OS}_{bck}(\eta_i) \\ N^{SS}_{data}(\eta_i) &= N^{SS}_{signal}(\eta_i) + N^{SS}_{bck}(\eta_i), \end{aligned} \tag{4.1}$$

where $N^{OS/SS}_{data}(\eta_i)$ denotes the number of opposite- and same-sign events in the detector data within i^{th} η bin and $N^{OS/SS}_{signal/bck}$ on the right side of the equation denotes the corresponding number of opposite- and same-sign events for real and fake τ_{had} within i^{th} η bin. Only the dependency of the charge-flip rate on η has been added since it has already been shown in the MC study (see Fig. 3.4 and 3.6) that the charge-flip rate is only strongly dependent on η but the dependency on p_T is almost flat, implying that the distribution of N^{OS} and N^{SS} with respect to p_T have almost the same shape. As shown in Fig. 4.2, the normalised any- and same-sign distribution of hadronic τ-leptons with respect to η have opposite trend but almost overlap for p_T. Note that Fig. 4.2 is plotted as a comparison between any- and same-sign events, but it does not affect the illustration of the idea that including p_T in Eq. (4.1) is unnecessary as the distribution of N^{AS} is very close to that of N^{OS}. In the template method, it is necessary to make sure that the templates have different shapes so that the fit of the templates to data is non-degenerate.

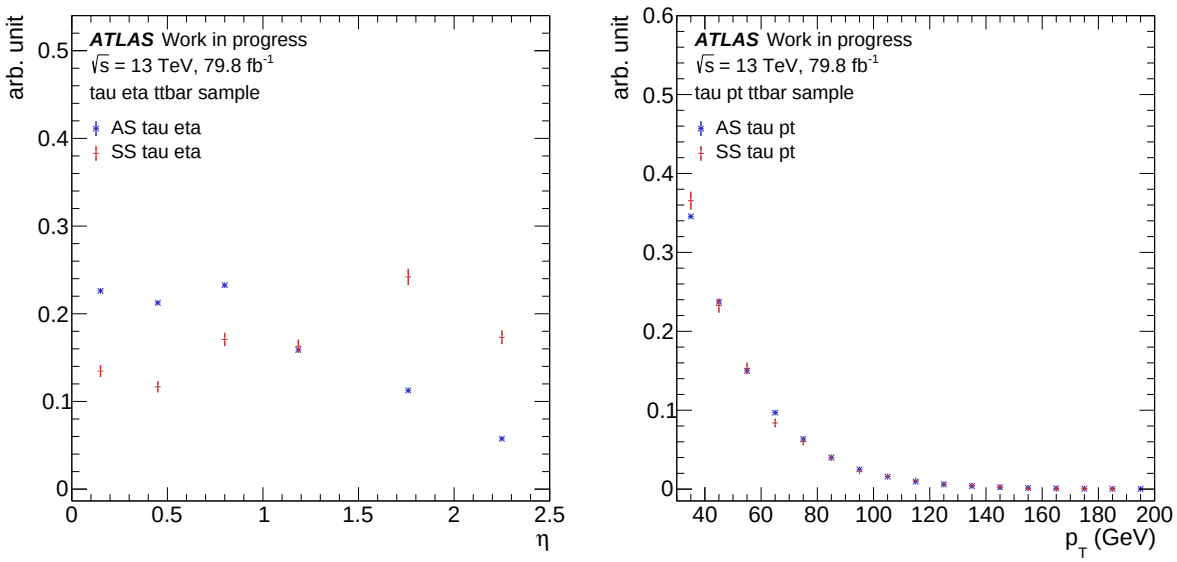

(a) (b)

Fig. 4.2 Comparison of the normalised any- and same-sign distribution of hadronic τ-leptons with respect to η (left) and p_T (right), respectively, in the $t\bar{t} \to \tau_\mu \tau_{\text{had}}$ channel.

According to Eq. (4.1), four templates are required to characterise the shape of each part. The definitions of these four templates are summarised in Table 4.1.

Template	Definition
TMPL(N^{OS}_{signal})	$N^{OS}_{truthMC}$
TMPL(N^{OS}_{bck})	$N^{OS}_{inc.MC} - N^{OS}_{truthMC}$
TMPL(N^{SS}_{signal})	$N^{SS}_{truthMC}$
TMPL(N^{SS}_{bck})	$N^{SS}_{inc.MC} - N^{SS}_{truthMC}$

Table 4.1 Summary of the definitions of templates. Truth MC and inclusive MC mean that the reconstructed taus are truth matched to their origins and not truth matched, respectively.

Therefore, by performing the fit of the templates to data, the optimum scaling parameters (a,b,c,d), as stated in the equations below

$$N^{OS}_{data}(\eta_i) = a \cdot \text{TMPL}\left(N^{OS}_{signal}(\eta_i)\right) + b \cdot \text{TMPL}\left(N^{OS}_{bck}(\eta_i)\right) \tag{4.2}$$

$$N^{SS}_{data}(\eta_i) = c \cdot \text{TMPL}\left(N^{SS}_{signal}(\eta_i)\right) + d \cdot \text{TMPL}\left(N^{SS}_{bck}(\eta_i)\right), \tag{4.3}$$

can be found. The $\tau_\mu \tau_{\text{had}}$ final state is used to apply the template fit method since the SS truth matched MC in this channel has the highest statistics in comparing to $\tau_{\text{had}}\tau_{\text{had}}$ final state. The charge flip rate $\varepsilon_{\tau_{\text{had}}}$, in this case, is similar to the definition in the tag-and-probe method which can be calculated according to

$$\varepsilon_{\tau_{had}}(\eta_i) = \frac{c \cdot \text{TMPL}\left(N^{SS}_{signal}(\eta_i)\right)}{a \cdot \text{TMPL}\left(N^{OS}_{signal}(\eta_i)\right) + c \cdot \text{TMPL}\left(N^{SS}_{signal}(\eta_i)\right)}. \tag{4.4}$$

Although the charge-flip rate is chosen to relate any-sign events with same-sign events according to the convention used in the previous study on electrons, it should be noted that the template fit in RooFit (see section 4.5.2) as my final result is performed on the opposite- and same-sign data respectively so as to make sure that the scaling parameters are not correlated with each other. In the proof of concept study using Mathematica (see section 4.5.1), the template fit is performed on the any- and same-sign data so that the correlation is not excluded.

4.3 Data sets

The data collected by the ATLAS detector from 2015 to 2017 with the SUSY3 derivation are used in this part of the analysis. The proton–proton collision energy is $\sqrt{s} = 13$ TeV with a total integrated luminosity of 79.8 fb^{-1}.

4.4 Selections

The selections are summarised in table 4.2 with the specific selections for the Z control region and $t\bar{t}$ region recommended by the SSDiLep group.

Type	Selections
Baseline	Single muon trigger: HLT_mu20_iloose + HLT_mu50 (2015) HLT_muon26_ivarmedium + HLT_mu50 (2016-2017) One muon and one tau. Electron veto Muon: $p_T > 30$ GeV, medium working point, isolated, $z_0 \sin\theta < 0.5$, $d_0\text{sig} < 3.0$ Tau: $p_T > 30$ GeV, medium working point, isolated
Z control region	$m_T(\mu, E_T^{miss}) = \sqrt{2p_T(\mu)E_T^{miss}\left(1-\cos\Delta\phi(\mu, E_T^{miss})\right)} < 50$ GeV $\cos\Delta\phi(\mu, E_T^{\text{miss}}) + \cos\Delta\phi(\tau_{\text{had}}, E_T^{\text{miss}}) > 0.5$
$t\bar{t}$ control region	Muon: $p_T > 50$ GeV, Tau: $p_T > 50$ GeV At least one b-tagged jet

Table 4.2 Summary of the selections for the template fit method.

In the Z control region, the definition of transverse mass is simply a rearrangement of the basic definition

$$\begin{aligned} m_T^2(l, E_T^{\text{miss}}) &= (E_{T,l} + E_{T,E_T^{\text{miss}}})^2 - (\mathbf{p}_{T,l} + \mathbf{p}_{T,E_T^{\text{miss}}})^2 \\ &= 2|\mathbf{p}_{T,l}||\mathbf{p}_{T,E_T^{\text{miss}}}|\left(1-\cos\left(\Delta\phi_{l,E_T^{\text{miss}}}\right)\right). \end{aligned} \tag{4.5}$$

Based on the presented selections, the opposite-sign and same-sign data and MC compositions are plotted with respect to the mass of $\tau_\mu\tau_{\text{had}}$ final state for both $Z \to \tau_\mu\tau_{\text{had}}$ and $t\bar{t} \to \tau_\mu\tau_{\text{had}}$ samples in Fig. 4.3, 4.4, 4.5 and 4.6. The inclusive (non-truth matched) and truth matched MC compositions are plotted separately. As expected, the inclusive MC agrees well with the data, while the truth matched MC indicates a significant difference between the data and the contributions from real prompt τ-leptons. In principle, both $Z \to \tau_\mu\tau_{\text{had}}$ and $t\bar{t} \to \tau_\mu\tau_{\text{had}}$ can be used for the template fit method, while the signal-to-background ratio (real τ_{had} against fake τ_{had}) is lower for same-sign $Z \to \tau_\mu\tau_{\text{had}}$ samples in comparing to $t\bar{t} \to \tau_\mu\tau_{\text{had}}$, as shown in Fig. 4.4b and 4.6b. Therefore, only $t\bar{t}$ samples are used in the template fit. Additionally, the requirement on the number of b-tagged jets is chosen to be at least one instead of exactly two due to the fact that the two b-tagged jets cut kills too many events which makes the distribution look like statistical fluctuation.

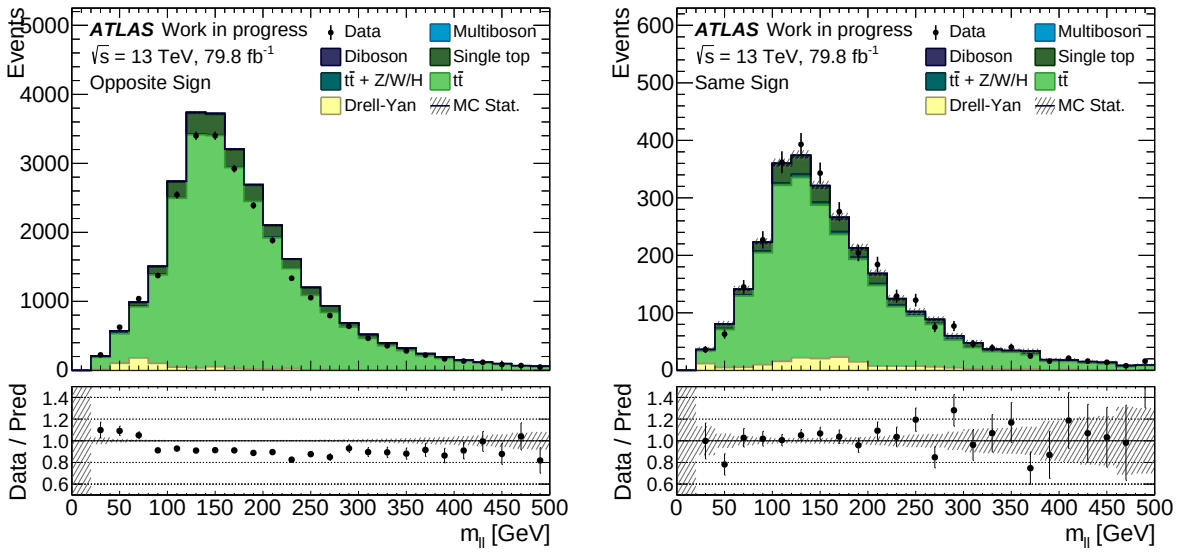

(a) (b)

Fig. 4.3 Compositions of the OS (left) and SS (right) inclusive selection in the $t\bar{t}$ control region.

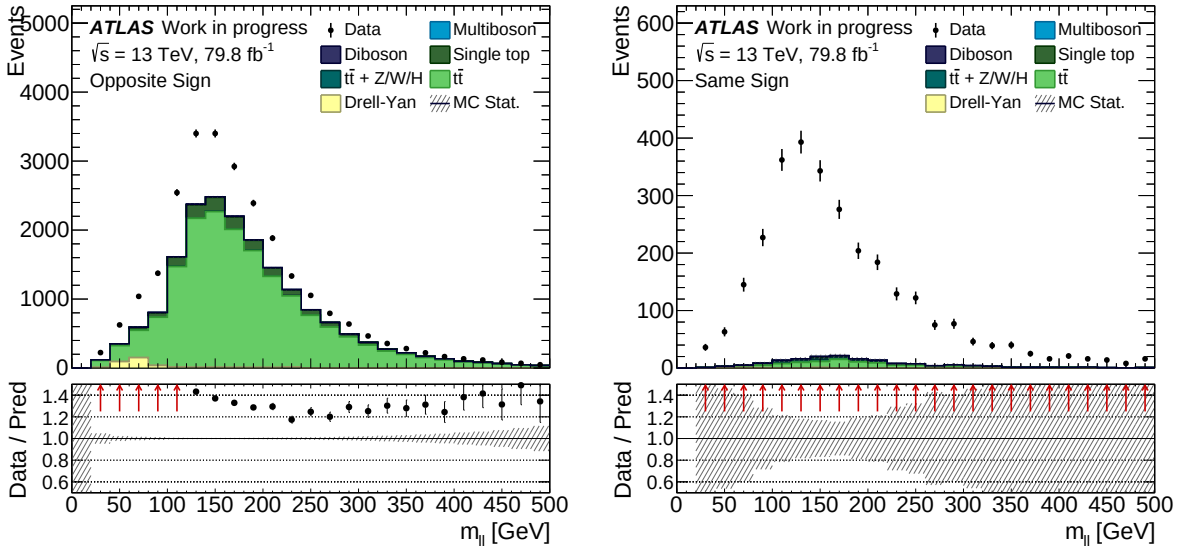

(a) (b)

Fig. 4.4 Compositions of the OS (left) and SS (right) truth selection in the $t\bar{t}$ control region.

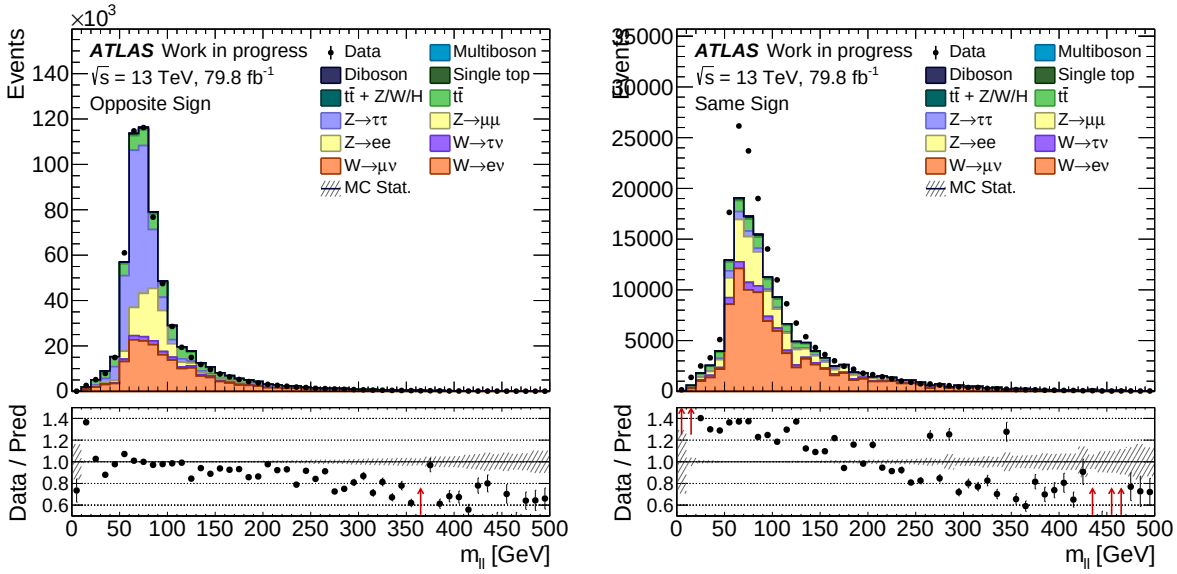

(a) (b)

Fig. 4.5 Compositions of the OS (left) and SS (right) inclusive selection in the Z control region.

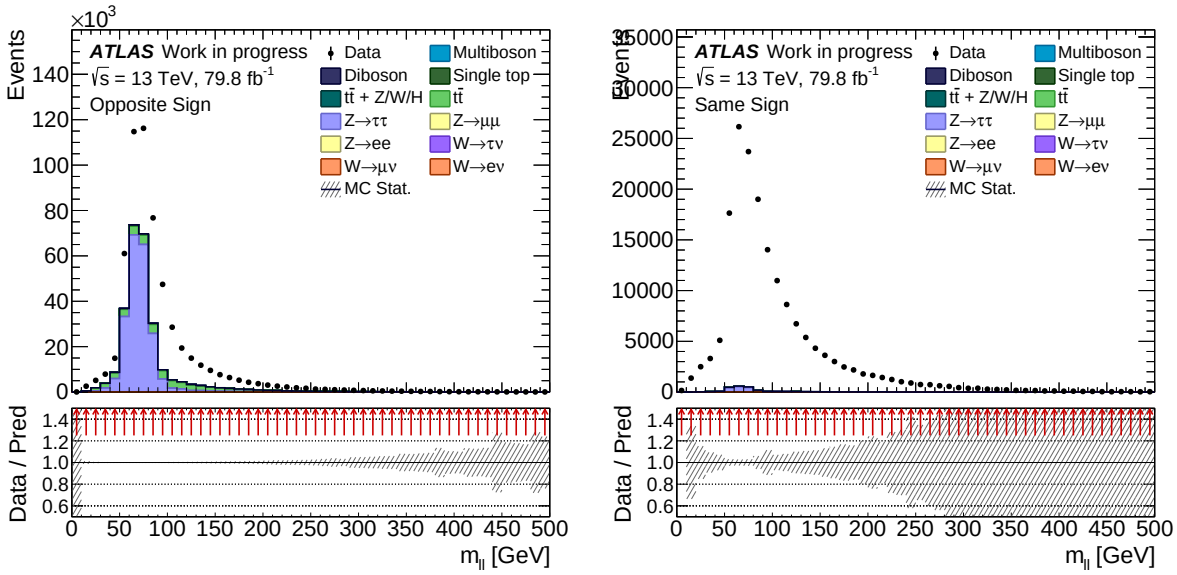

(a) (b)

Fig. 4.6 Compositions of the OS (left) and SS (right) truth selection in the Z control region.

4.4.1 Check for the performance of BDT

In this subsection, I present the attempts to increase the signal-to-background ratio, which also reflects the performance of the BDT for reconstructing and identifying hadronic τ-leptons. First, I will introduce some kinematic quantities that are provided in our ntuples.

A commonly used quantity to provide discrimination for the weakly interacting particles is the missing transverse momentum, E_T^{miss}, caused by the neutrinos escaping the detector. The following definition of the missing transverse momentum is based on [52, 53]. The reconstructed $\mathbf{E}_T^{\text{miss}}$ can be separated to two parts: the hard objects (electrons, muons, τ-leptons, photons, jets) and the soft term (anything, e.g. soft charged particles, disassociated with the reconstructed hard objects), mathematically given by

$$\mathbf{E}_T^{\text{miss}} = \underbrace{-\sum_{i\in\text{electrons}} \mathbf{p}_T^i}_{\mathbf{E}_T^{\text{miss},e}} \underbrace{-\sum_{i\in\text{muons}} \mathbf{p}_T^i}_{\mathbf{E}_T^{\text{miss},\mu}} \underbrace{-\sum_{i\in\text{hadronics }\tau} \mathbf{p}_T^i}_{\mathbf{E}_T^{\text{miss},\tau_{\text{had}}}} \underbrace{-\sum_{i\in\text{photons}} \mathbf{p}_T^i}_{\mathbf{E}_T^{\text{miss},\gamma}} \underbrace{-\sum_{i\in\text{jets}} \mathbf{p}_T^i}_{\mathbf{E}_T^{\text{miss,jets}}} \underbrace{-\sum_{i\in\text{soft term}} \mathbf{p}_T^i}_{\mathbf{E}_T^{\text{miss,soft}}}. \tag{4.6}$$

This leads to a similar quantity $\sum E_T$ (denoted as metSumEt) which is the scalar sums of the transverse momenta, given as

$$\sum E_T = \sum p_T^e + \sum p_T^\mu + \sum p_T^{\tau_{\text{had}}} + \sum p_T^\gamma + \sum p_T^{\text{jets}} + \sum p_T^{\text{soft}}. \tag{4.7}$$

Another quantity that requires explanation is ΔR which is the angular distance between two objects, calculated as

$$\Delta R_{ll'} = \left(\Delta\eta_{ll'}^2 + \Delta\phi_{ll'}^2\right)^{1/2}, \tag{4.8}$$

where l and l' denote two leptons in our case. The correlations of the kinematic variables (including $p_{T,ll'}$, $\eta_{ll'}$ $M_{T,ll'}$, $\phi_{ll'}$, $\Delta p_{T,ll'}$, $\Delta\eta_{ll'}$, $\Delta\phi_{ll'}$ and $\Delta R_{ll'}$) of two τ-lepton are plotted for detector data and MC simulation, respectively. In Fig. 4.7, the example plots of the correlation of $M_{T,ll'}$ and $\Delta R_{ll'}$ are presented and no significant difference between the detector and $t\bar{t} \to \tau_\mu \tau_{\text{had}}$ samples. The correlations of the permutation of all kinematic variables of ditau do not show a significant difference.

Then, jet variables are checked since hadronic τ-leptons can be faked by QCD jets. The events in $t\bar{t} \to \tau_\mu \tau_{\text{had}}$ samples are separated into three cases: true taus, unknown taus (truth origin = 0) and taus originated from charm and bottom mesons. The available jet kinematic variable distributions (including E_{jet}, η_{jet}, ϕ_{jet}, $p_{T,\text{jet}}$, $\mathbf{E}_T^{\text{miss,jet}}$ and $E_T^{\text{miss,jet}}$) are plotted for three cases. In Fig. 4.8, the distributions of two jet variables, η^{jet} and $\mathbf{E}_T^{\text{miss,jet}}$ are shown. In general, no significant difference can be observed for the distributions of all jet variables.

Moreover, the correlations of jet variables are compared for true taus and fake taus (unknown taus + taus originated from charm and bottom mesons). As shown in Fig. 4.9, the correlation between $p_{T,\text{jet}}$ and $\mathbf{E}_T^{\text{miss,jet}}$ is presented for true taus and fake taus in $t\bar{t} \to \tau_\mu \tau_{\text{had}}$ samples with no significant difference. For the correlations of other jet variables, the plane colour plots do not show significant differences as well.

Therefore, the lepton and jet variables in the current ntuples are not available to provide more discrimination between real taus and fake taus so as to increase the signal-to-background

ratio. The results also reflect that the current BDT has reached its best performance unless extra information can be provided.

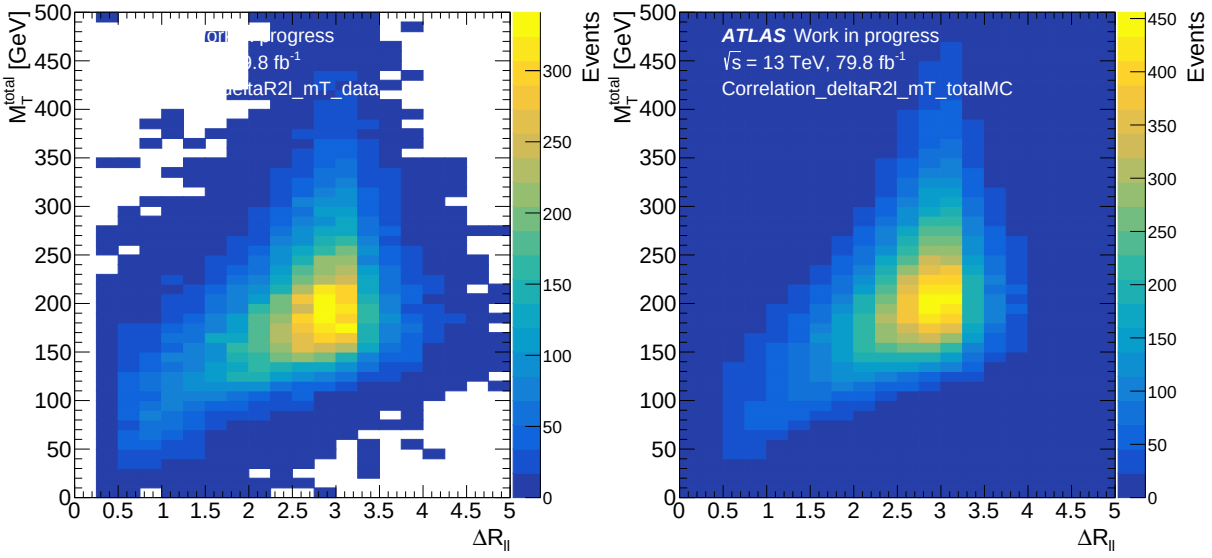

(a) (b)

Fig. 4.7 The correlation of ditau variables, $\Delta R_{ll'}$ and M_T^{total}, for detector data (left) and $t\bar{t} \to \tau_\mu \tau_{\text{had}}$ samples (right).

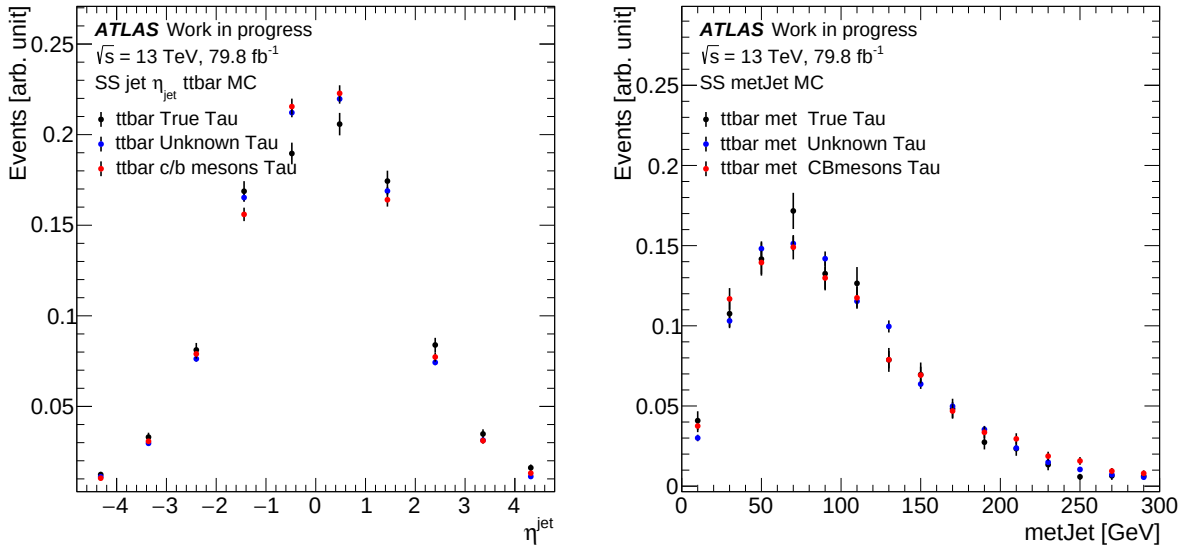

(a) (b)

Fig. 4.8 Distributions of two jet variables, η^{jet} and $\mathbf{E}_T^{\text{miss,jet}}$ for true taus, unknown taus and taus originated from charm and bottom mesons.

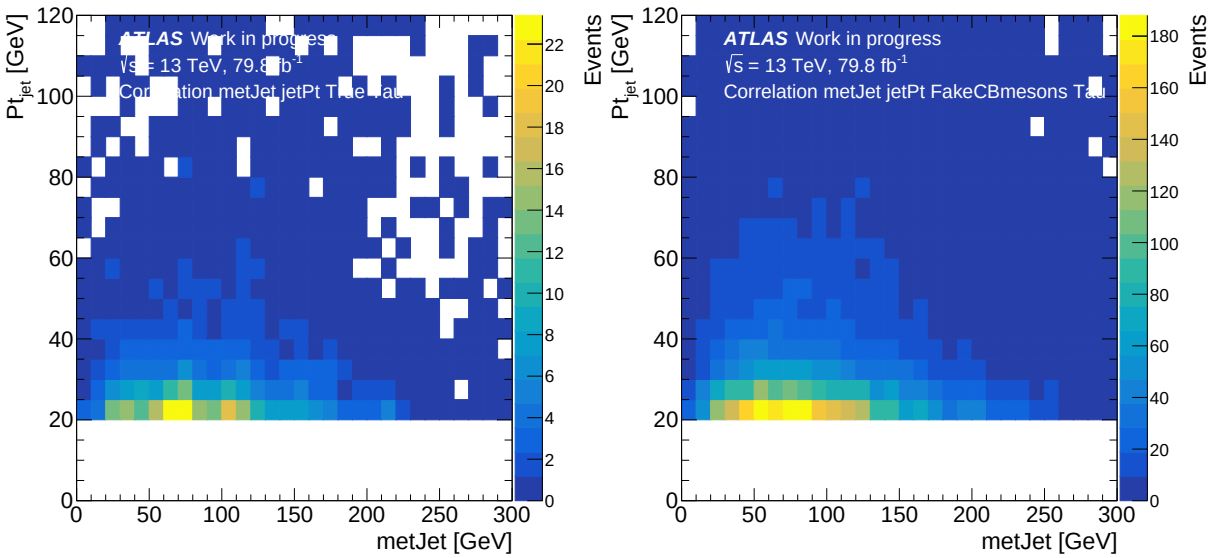

(a) (b)

Fig. 4.9 A plane colour plot representation of the correlation of $p_{T,\text{jet}}$ and $\mathbf{E}_T^{\text{miss,jet}}$ for true taus (left) and fake taus (right) in $t\bar{t} \to \tau_\mu \tau_{\text{had}}$ samples.

4.5 Results

4.5.1 Unbinned template fit in Mathematica

A proof of concept study was first conducted in Mathematica 11.1 in order to test whether the template fit with such a low signal-to-background ratio would be stable. Since this part of the study was performed before the template fit method finally determined, the signal and background templates for N^{OS} were approximated by N^{AS} instead of rigorously using N^{OS} to avoid the correlations between the any-sign and same-sign templates. This means that Eq. (4.2) is changed to

$$N^{AS}_{data}(\eta_i) = a \cdot \text{TMPL}\left(N^{AS}_{signal}(\eta_i)\right) + b \cdot \text{TMPL}\left(N^{AS}_{bck}(\eta_i)\right). \tag{4.9}$$

With this approximation, the charge-flip rate is simply given by

$$\varepsilon_{\tau_{had}}(\eta_i) = \frac{c \cdot \text{TMPL}\left(N^{SS}_{signal}(\eta_i)\right)}{a \cdot \text{TMPL}\left(N^{AS}_{signal}(\eta_i)\right)}. \tag{4.10}$$

The template fit in Mathematica is unbinned which means that continuous analytic functions are fitted to four templates as Mathematica is not specifically designed and optimised for binned fit using histograms directly. The analytic functions that fit well to the shape of the template data

are chosen to have following forms

$$\frac{ax+b}{e^{p_k(x)}} \quad \text{or} \quad \frac{ax+b}{e^{p_k(x)}} + \text{Gaussian}(x), \tag{4.11}$$

where $p_k(x)$ is the polynomial of x with degree k. In general, it is enough to set the degree $k = 3$, since the polynomial with a higher degree starts to show signs of oscillation. The built-in function `NonLinearModelFit` is used to perform the fit with the default fitting method chosen as the quasi-Newton method. The results of the fit which build the templates for (any- and same-sign) signal and background are shown in Fig. 4.10. Then, the any- and same-sign templates are fitted to corresponding detector data, as shown in Fig. 4.11. All the uncertainty bands are automatically generated by setting the confidence level in the `MeanPredictionBands` option to 68%.

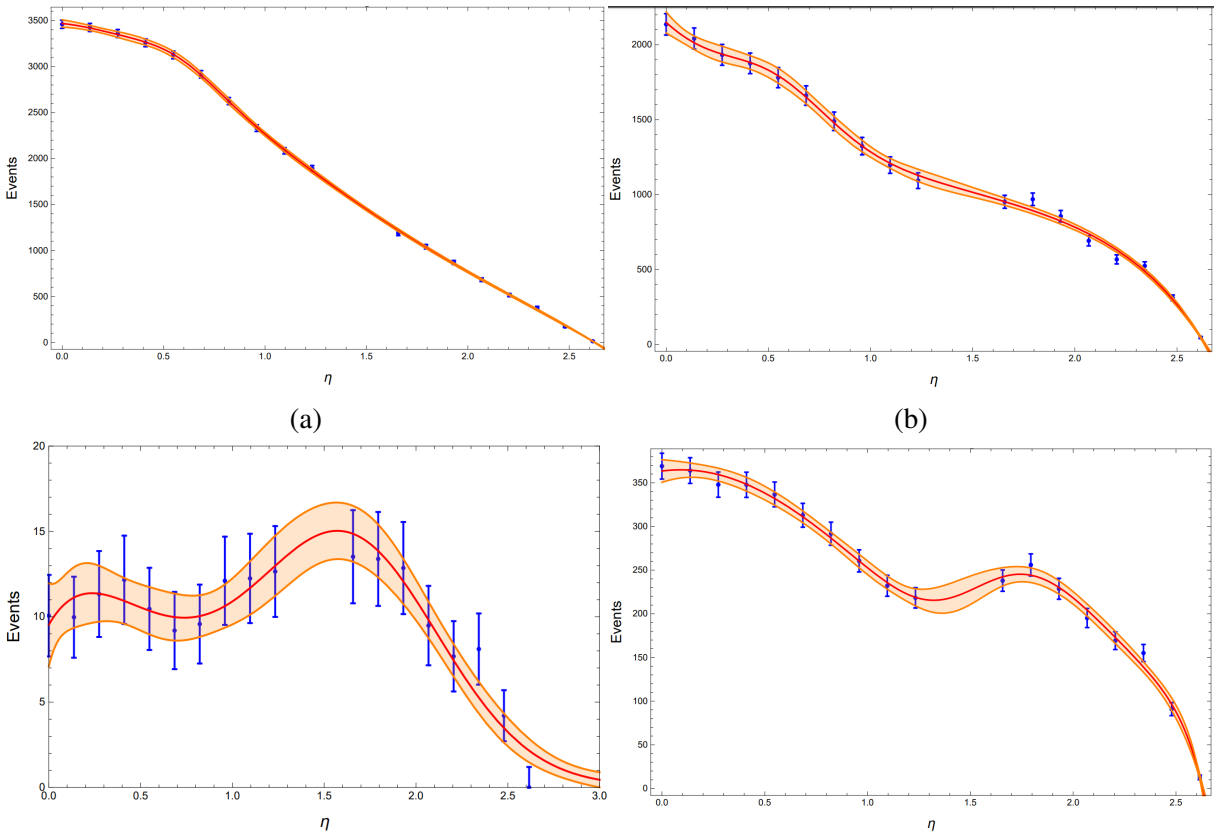

Fig. 4.10 Best fit of the analytic models (Eq. (4.11)) to $t\bar{t}$ any-sign signal (a), background (b) and same-sign signal (c), background (d) in the $t\bar{t}$ control region.

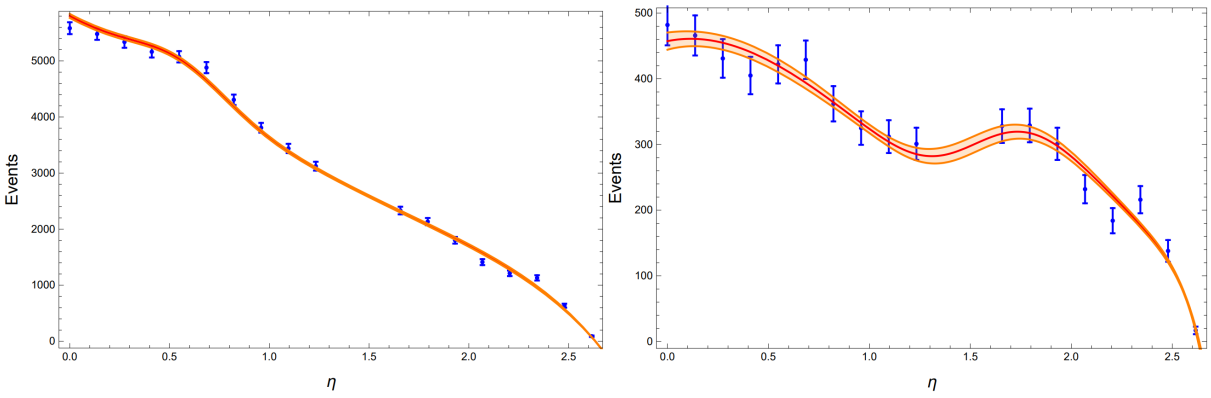

(a) (b)

Fig. 4.11 Best fit of the any- and same-sign templates to any- (left) and same-sign (right) detector data in the $t\bar{t}$ control region.

The best-fit values of the scaling parameters in Eq. (4.9) and 4.3 using Mathematica is summarised in table 4.3. The values are not unreasonable as they all lie within the vicinity of unity. In addition, to test the stability of the fit, the templates are scaled by some factors to test whether it still results in the same best-fit values. It is concluded that the fit is stable so that the feasibility of the template fit method is validated.

Parameter name	Mathematica best-fit value
a (N^{AS} sig.)	0.820 ± 0.045
b (N^{AS} bck.)	1.377 ± 0.070
c (N^{SS} sig.)	1.364 ± 1.862
d (N^{SS} bck.)	1.223 ± 0.078

Table 4.3 Best-fit values of the parameters in Eq. 4.9 and 4.3 using Mathematica.

4.5.2 Binned template fit in RooFit

In this subsection, the results of the template fit using a dedicated toolkit, known as the RooFit [54], are presented. RooFit is designed specifically for modelling the distribution of events in particle physics and its binned fit (using histogram directly) is highly customisable. All configuration information is automatically passed to Minuit, as mentioned in section 3.1.4. In addition, the (a)symmetric uncertainties of the fitted parameters are automatically calculated using the MINOS method in the Minuit package (see e.g. [55] for more details). The errors of the parameters are presented in terms of a symmetric error or two asymmetric errors characterising the variation in the positive and negative direction. Since the symmetric errors are almost the same as the average of two asymmetric errors in our study, the symmetric errors are used.

The results of the template fit using RooFit are presented in Fig. 4.12. Note that other MC processes: diboson, Drell-Yan, singletop and ttX process are included in the compositions of the detector data, but they are fixed and only the $t\bar{t}$ templates are actually floating in order for the fit to be more stable. The best-fit values of the scaling parameters in Eq. (4.2) and 4.3 are summarised in table 4.4.

Parameter name	RooFit best-fit value
a (N^{OS} sig.)	0.7591 ± 0.0358
b (N^{OS} bck.)	1.1688 ± 0.0697
c (N^{SS} sig.)	1.1630 ± 1.0583
d (N^{SS} bck.)	1.0389 ± 0.0176

Table 4.4 Best-fit values of the parameters in Eq. (4.10) using RooFit.

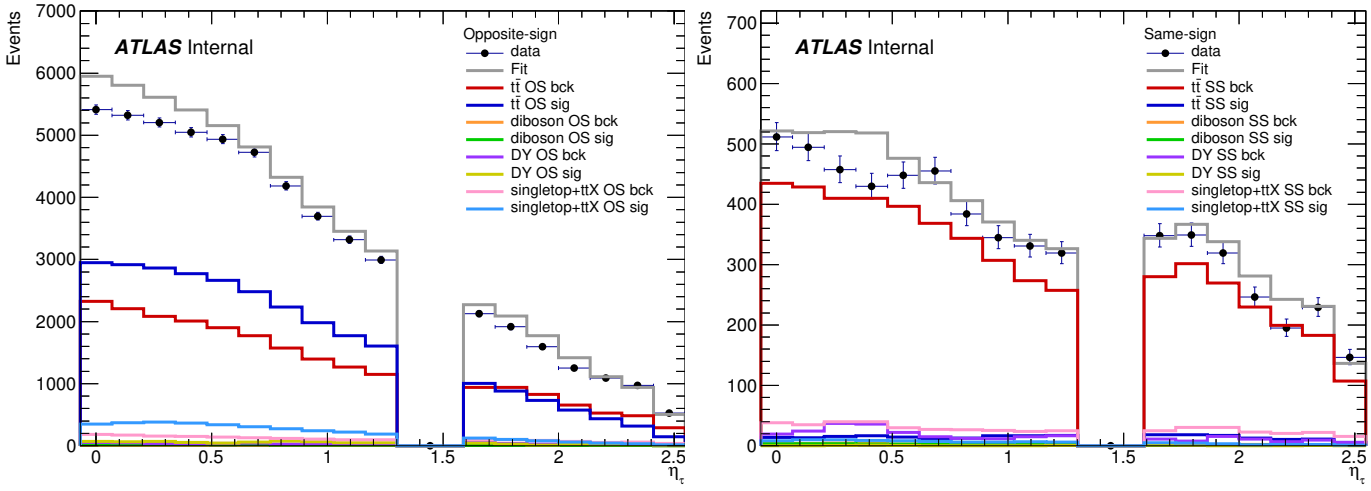

(a) (b)

Fig. 4.12 The template fit of opposite-sign and same-sign $t\bar{t}$ templates using RooFit. The crack region, $1.37 < \eta < 1.52$, is excluded.

In comparing to the best-fit values from Mathematica fit, the values are slightly lower which is reasonable as other background processes are included in RooFit. The ratio of the scaling parameters a and c approximately characterising the magnitude of the charge-flip rate agree well for both fitting algorithms. The charge-flip rate of detector data in the $t\bar{t}$ control region using $\tau_\mu \tau_{\text{had}}$ final state is calculated using Eq. (4.10) and presented in Fig. 4.13 along with the previous result estimated based on $t\bar{t} \to \tau_\mu \tau_{\text{had}}$ MC samples using tag-and-probe method because this estimation has the lowest uncertainty.

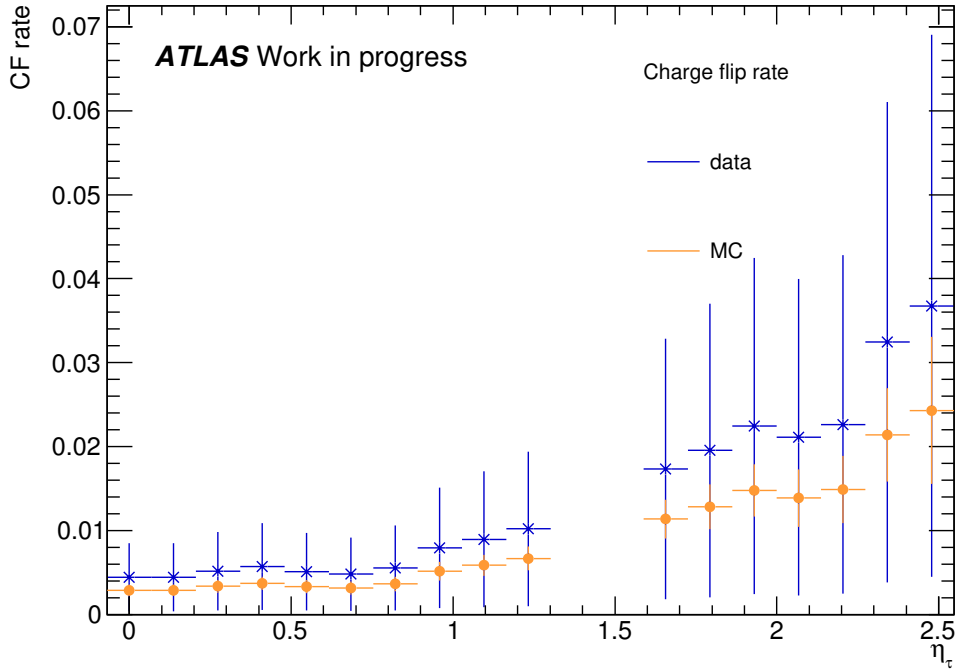

Fig. 4.13 Charge flip rate of hadronic taus for data and MC estimated using template fit and tag-and-probe method in the $t\bar{t}$ control region, respectively. The crack region, $1.37 < \eta < 1.52$, is excluded.

4.6 Scale factor and discussion

The scale factor, defined as the ratio of the charge flip rate of data and MC, is obtained by dividing two distributions in fig. 4.13. The error bars for the charge-flip rate of data are quite large as a result of a large error in the best-fit value of parameter c, as stated in table 4.4, due to the low signal-to-background ratio in N^{SS} distribution. Therefore, the values of the scale factor are merged for all η bins to reduce the uncertainty.

More importantly, the templates used in the template fit method are built from MC samples so that the shape of the charge-flip rate distribution is the same for data and MC. This means the scale factor is independent with respect to η_τ which is considered as a limitation of this method. As shown in Fig. 4.14, the scale factors are first combined in two ranges $|\eta| < 1.37$ and $1.52 < |\eta| < 2.5$. By further combining the scale factors in those two regions, we are able to reduce the uncertainty and obtain the final value of the scale factor equalling to 1.52 ± 0.42.

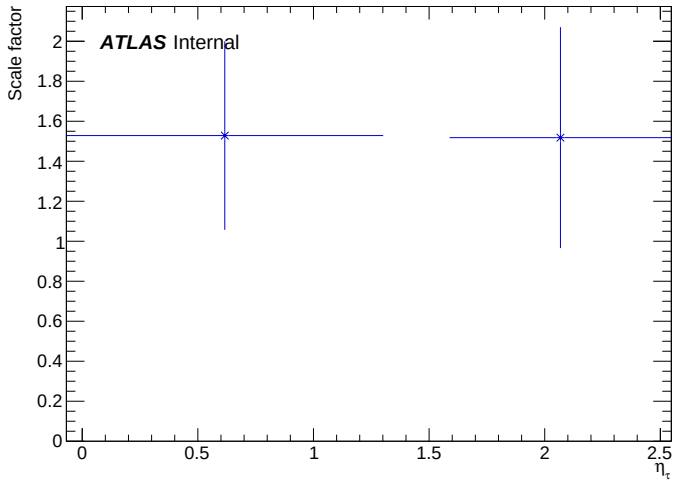

Fig. 4.14 The combined scale factors in the ranges $|\eta| < 1.37$ and $1.52 < |\eta| < 2.5$.

The scale factors for the charge-flip rate of electrons is slightly lower than unity while it is opposite for hadronic τ-leptons [28]. As unity does not fall within the range of the uncertainty in the scale factor, it is necessary to apply this correction to MC samples to compensate for the difference to detector data in the search for doubly charged Higgs bosons using hadronic τ-leptons. It should be noted that the closure test for the charge-flip rate for detector data is not mentioned. This is because the current data in two control regions are enriched in the QCD multijet (fake tau) background so that there is no way to apply the estimated charge-flip rate directly. Therefore, a more conservative way of applying the scale factor is to add its error bar into the uncertainty estimation in the signal region instead of applying correction directly.

The charge-flip rates for hadronic τ-leptons typically range from 0.4% to 3.8% and it is not the dominant background process. The dominant background comes from misidentification of QCD jets which can have indistinguishable signatures. Also, fake tau background in detector data greatly affects the statistics in estimated charge-flip rates. Although the current BDT for reconstruction and identification of τ_{had} has been shown to perform effectively, it is far from ideal. Other discriminating variables should be considered to add to the BDT to improve its performance. However, it may not be so obvious what variables may provide better discrimination.

Chapter 5

Summary and outlook

This thesis work is dedicated to the study of one of the backgrounds, known as the charge-flip background, in the search for doubly charged Higgs bosons using hadronic τ-leptons. The charge-flip background corresponds to the misidentification of the sign of the charge of prompt leptons by the ATLAS detector due to limited detector resolution. To estimate this background, three methods are used with the data-driven and tag-and-probe method applied to MC simulated samples and the template fit method applied to detector data collected from 2015 to 2017 by the ATLAS detector at $\sqrt{s} = 13$ TeV with a total integrated luminosity of 79.8 fb^{-1}.

The data-driven and tag-and-probe method are adopted from the previous study on electrons misidentification probability. The resulting τ_{had} charge-flip rates from both methods using $Z \to \tau\tau$ and $t\bar{t} \to \tau\tau$ samples agree well with each other. It was observed that the charge-flip rates are strongly dependent on η but almost independent on p_T. In the tag-and-probe method, the charge-flip probability rises from around 0.3% to 2.2% with the increase of η, which agrees with the charge-flip rate, given as $\sigma(p_T) \times f(\eta)$, from the data-driven method. The one- and three-pronged decay modes are investigated using the tag-and-probe method respectively. The one-pronged τ_{had} has a slightly higher rate, especially at a high η value. Due to the tiny difference (e.g. within 0.1% at $2 < |\eta| < 2.5$ bin), it seems that there is no need for separating prongedness with current statistics. The result from the tag-and-probe method using $t\bar{t} \to \tau_\mu \tau_{\text{had}}$ channel is chosen to be used in calculating the scale factor since it has the highest statistics.

The template fit method is performed in Mathematica as a proof of concept study and in RooFit to produce the final results. It is necessary to make sure that the templates have different shapes so that the fit of the templates to data is non-degenerate. Therefore, it is unnecessary to include the dependency of the charge-flip rate on p_T in our method. The $t\bar{t} \to \tau_\mu \tau_{\text{had}}$ channel is chosen to build the templates due to a higher signal-to-background ratio in comparing to other channels. The detector data are therefore applied with the selections for the $t\bar{t}$ control region. The resulting charge-flip rate for detector data is higher than the results from MC samples, leading to a scale factor of 1.52 ± 0.42.

The value of the scale factor as the main purpose of this thesis is successfully derived. However, there are still many questions remaining open for future work. The cause of the charge-flip rate of τ-leptons will be an important thing to investigate and understand. The idea for this study is to use the truth information of the tracks and event display. Though not presented in this thesis work, the AOD files of a few selected one- and three-pronged charge-flip events were extracted from the ATLAS data repository and displayed using Virtual Point-1 (VP1), a visualisation software that digitally recreates the 3D collision event. However, the truth information (types of particles and the sign of the charge) for the tracks from the decay of τ_{had} is not saved so that it is difficult to draw a conclusion on what is the exact cause. If such truth information is not available, the generation of MC samples followed by detector simulation and reconstruction and identification process may be required. The study of this will give a clear answer on whether the strong dependence of the charge-flip rate on η has a similar cause (e.g. trident events created by π^0 decay) in comparing to electrons and why charge-flip rate of $\tau_{\text{1-pronged}}$ is slightly higher than that of $\tau_{\text{3-pronged}}$.

The understanding of the cause of the charge-flip of τ_{had} will also provide some insights on what discriminating variables may be useful to improve the performance of the BDT responsible for reconstruction and identification of τ_{had}. This will lead to a better estimation of the charge-flip rate of τ_{had} for detector data as the current constraint to the statistics is not the number of events but the signal-to-background ratio.

In addition, the scale factor is independent on η due to the limitation of the template fit method. If the signal-to-background ratio can be reduced, it will be interesting to develop new methods to derive η-dependent scale factor with better statistics.

References

[1] Joao Pequenao. Computer generated image of the whole ATLAS detector. Mar 2008.

[2] J. Catmore. Introduction to atlas data preparation and analysis. In *Joint Oslo/Bergen/NBI ATLAS Software Tutorial*, University of Oslo, Norway, Feb. 8-9 2016.

[3] Morad Aaboud et al. Search for doubly charged Higgs boson production in multi-lepton final states with the ATLAS detector using proton–proton collisions at $\sqrt{s} = 13\,\text{TeV}$. *Eur. Phys. J.*, C78(3):199, 2018.

[4] Joern Mahlstedt. The atlas hadronic tau trigger. *Journal of Physics: Conference Series*, 513:012021, 06 2014.

[5] M. Aaboud et al. A study of the material in the ATLAS inner detector using secondary hadronic interactions. A measurement of the material in the ATLAS inner detector using secondary hadronic interactions. *JINST*, 7(arXiv:1110.6191. CERN-PH-EP-2011-147):P01013. 22 p, Oct 2011. Comments: 22 pages plus author list (41 pages total), 12 figures, 4 tables, submitted to Journal of Instrumentation.

[6] G. Aad et al. The ATLAS Experiment at the CERN Large Hadron Collider. *JINST*, 3:S08003, 2008.

[7] Tau Selection Tool. https://gitlab.cern.ch/atlas/athena/blob/21.2/PhysicsAnalysis/TauID/TauAnalysisTools/doc/README-TauSelectionTool.rst.

[8] S. L. Glashow. Partial Symmetries of Weak Interactions. *Nucl. Phys.*, 22:579–588, 1961.

[9] Steven Weinberg. A Model of Leptons. *Phys. Rev. Lett.*, 19:1264–1266, 1967.

[10] Abdus Salam. Weak and Electromagnetic Interactions. *Conf. Proc.*, C680519:367–377, 1968.

[11] Richard Keith Ellis, William James Stirling, and Bryan R Webber. *QCD and Collider Physics*. Cambridge monographs on particle physics, nuclear physics, and cosmology. Cambridge Univ. Press, Cambridge, 2003. Photography by S. Vascotto.

[12] P. Skands. Introduction to QCD. In K. Matchev and et al., editors, *Searching for New Physics at Small and Large Scales (TASI 2012) - Proceedings of the 2012 Theoretical Advanced Study Institute in Elementary Particle Physics. Edited by Schmaltz Martin Pierpaoli Elena. Published by World Scientific Publishing Co. Pte. Ltd., 2013. ISBN #9789814525220, pp. 341-420*, pages 341–420, August 2013.

[13] B. Pontecorvo. Neutrino Experiments and the Problem of Conservation of Leptonic Charge. *Sov. Phys. JETP*, 26:984–988, 1968. [Zh. Eksp. Teor. Fiz.53,1717(1967)].

[14] J. Schechter and J. W. F. Valle. Neutrino Masses in SU(2) x U(1) Theories. *Phys. Rev.*, D22:2227, 1980.

[15] J. E. Cieza Montalvo, Nelson V. Cortez, J. Sa Borges, and Mauro D. Tonasse. Searching for doubly charged Higgs bosons at the LHC in a 3-3-1 model. *Nucl. Phys.*, B756:1–15, 2006. [Erratum: Nucl. Phys.B796,422(2008)].

[16] J. F. Gunion, R. Vega, and J. Wudka. Higgs triplets in the standard model. *Phys. Rev. D*, 42:1673–1691, Sep 1990.

[17] Eung Jin Chun, Kang Young Lee, and Seong Chan Park. Testing Higgs triplet model and neutrino mass patterns. *Phys. Lett.*, B566:142–151, 2003.

[18] Ambalika Biswas. All about $H^{\pm\pm}$ in Higgs Triplet Model. 2017.

[19] Pavel Fileviez Perez, Tao Han, Gui-yu Huang, Tong Li, and Kai Wang. Neutrino Masses and the CERN LHC: Testing Type II Seesaw. *Phys. Rev.*, D78:015018, 2008.

[20] Paramita Dey, Anirban Kundu, and Biswarup Mukhopadhyaya. Some consequences of a Higgs triplet. *J. Phys.*, G36:025002, 2009.

[21] Ernest Ma, Martti Raidal, and Utpal Sarkar. Phenomenology of the neutrino mass giving Higgs triplet and the low-energy seesaw violation of lepton number. *Nucl. Phys.*, B615:313–330, 2001.

[22] Bhaskar Dutta, Ricardo Eusebi, Yu Gao, Tathagata Ghosh, and Teruki Kamon. Exploring the doubly charged Higgs boson of the left-right symmetric model using vector boson fusionlike events at the LHC. *Phys. Rev.*, D90:055015, 2014.

[23] J. F. Gunion, J. Grifols, A. Mendez, B. Kayser, and F. Olness. Higgs bosons in left-right-symmetric models. *Phys. Rev. D*, 40:1546–1561, Sep 1989.

[24] K. Huitu, J. Maalampi, A. Pietila, and M. Raidal. Doubly charged Higgs at LHC. *Nucl. Phys.*, B487:27–42, 1997.

[25] N. G. Deshpande, J. F. Gunion, B. Kayser, and Fredrick Olness. Left-right-symmetric electroweak models with triplet higgs field. *Phys. Rev. D*, 44:837–858, Aug 1991.

[26] S. F. King. Neutrino mass models. *Rept. Prog. Phys.*, 67:107–158, 2004.

[27] Lyndon Evans. The large hadron collider. *New Journal of Physics*, 9(9):335–335, sep 2007.

[28] Anthony Hawkins. *Searches for beyond Standard Model physics with same-sign dileptons*. PhD thesis, Lund U., 2014-10-20.

[29] Shalu Solomon and François Corriveau. Measurement of the Production Cross-Section of the Z Boson and Determination of its Spin with the ATLAS Detector, Feb 2019. Presented 2019.

[30] Tony Tong and Melissa Franklin. *Search for pair production of Higgs bosons in the four b quark final state with the ATLAS detector*. PhD thesis, May 2018. Presented 27 Apr 2018.

[31] Morad Aaboud et al. Performance of the ATLAS Transition Radiation Tracker in Run 1 of the LHC: tracker properties. *JINST*, 12(05):P05002, 2017.

[32] Moritz Backes. The ATLAS Trigger System : Ready for Run-2. Technical Report ATL-DAQ-PROC-2015-041, CERN, Geneva, Oct 2015.

[33] Torbjörn Sjöstrand, Stefan Ask, Jesper R. Christiansen, Richard Corke, Nishita Desai, Philip Ilten, Stephen Mrenna, Stefan Prestel, Christine O. Rasmussen, and Peter Z. Skands. An Introduction to PYTHIA 8.2. *Comput. Phys. Commun.*, 191:159–177, 2015.

[34] M. Bahr et al. Herwig++ Physics and Manual. *Eur. Phys. J.*, C58:639–707, 2008.

[35] T. Gleisberg, Stefan. Hoeche, F. Krauss, M. Schonherr, S. Schumann, F. Siegert, and J. Winter. Event generation with SHERPA 1.1. *JHEP*, 02:007, 2009.

[36] S. Agostinelli et al. GEANT4: A Simulation toolkit. *Nucl. Instrum. Meth.*, A506:250–303, 2003.

[37] Vikram Rentala, William Shepherd, and Shufang Su. A Simplified Model Approach to Same-sign Dilepton Resonances. *Phys. Rev.*, D84:035004, 2011.

[38] Morad Aaboud et al. Search for doubly charged scalar bosons decaying into same-sign W boson pairs with the ATLAS detector. *Eur. Phys. J.*, C79(1):58, 2019.

[39] M. Tanabashi et al. Review of Particle Physics. *Phys. Rev.*, D98(3):030001, 2018.

[40] Georges Aad et al. Reconstruction of hadronic decay products of tau leptons with the ATLAS experiment. *Eur. Phys. J.*, C76(5):295, 2016.

[41] Reconstruction, Energy Calibration, and Identification of Hadronically Decaying Tau Leptons in the ATLAS Experiment for Run-2 of the LHC. Technical Report ATL-PHYS-PUB-2015-045, CERN, Geneva, Nov 2015.

[42] Matteo Cacciari, Gavin P. Salam, and Gregory Soyez. The anti-k_t jet clustering algorithm. *JHEP*, 04:063, 2008.

[43] Morad Aaboud et al. $ZZ \to \ell^+\ell^-\ell'^+\ell'^-$ cross-section measurements and search for anomalous triple gauge couplings in 13 TeV pp collisions with the ATLAS detector. *Phys. Rev.*, D97(3):032005, 2018.

[44] Morad Aaboud et al. Measurement of $W^{\pm}Z$ production cross sections and gauge boson polarisation in pp collisions at $\sqrt{s} = 13$ TeV with the ATLAS detector. 2019.

[45] Morad Aaboud et al. Measurement of fiducial and differential W^+W^- production cross-sections at $\sqrt{s}$ =13 TeV with the ATLAS detector. 2019.

[46] Morad Aaboud et al. Measurement of the $t\bar{t}Z$ and $t\bar{t}W$ cross sections in proton-proton collisions at $\sqrt{s} = 13$ TeV with the ATLAS detector. *Phys. Rev.*, D99(7):072009, 2019.

[47] M. Aaboud et al. Observation of Higgs boson production in association with a top quark pair at the LHC with the ATLAS detector. *Phys. Lett.*, B784:173–191, 2018.

[48] Miha Muskinja, Borut Kersevan, and Andrej Gorisek. *Search for new physics processes with same charge leptons in the final state with the ATLAS detector using proton–proton collisions at* $\sqrt{s} = 13$ *TeV. Iskanje procesov nove fizike s pari enako nabitih leptonov v končnem stanju z detektorjem ATLAS s trki protonov pri energiji* $\sqrt{s} = 13$ *TeV*. PhD thesis, CERN-THESIS-2018-196, Aug 2018.

[49] H. Bethe and W. Heitler. On the Stopping of fast particles and on the creation of positive electrons. *Proc. Roy. Soc. Lond.*, A146:83–112, 1934.

[50] Minuit 2 ROOT. https://root.cern.ch/root/htmldoc/guides/minuit2/Minuit2.html.

[51] TH1 Class Reference. https://root.cern.ch/doc/master/classTH1.html.

[52] Douglas Schaefer, Dilia Maria Portillo Quintero, Paolo Francavilla, Calum Michael Macdonald, Mariyan Petrov, and Emma Tolley. Object based Missing Transverse Momentum Significance in the ATLAS Detector. Technical Report ATL-COM-PHYS-2017-1735, CERN, Geneva, Dec 2017.

[53] Morad Aaboud et al. Performance of missing transverse momentum reconstruction with the ATLAS detector using proton-proton collisions at $\sqrt{s}$ = 13 TeV. *Eur. Phys. J.*, C78(11):903, 2018.

[54] RooFit. https://root.cern.ch/roofit.

[55] F and James. MINUIT: Function Minimization and Error Analysis Reference Manual. 1998. CERN Program Library Long Writeups.

[56] ATLAS VP1. https://atlas-vp1.web.cern.ch/atlas-vp1/home/.

[57] Software Tutorial Event Picking For VP1 twiki page. https://twiki.cern.ch/twiki/bin/view/AtlasComputing/SoftwareTutorialEventPickingForVP1.

[58] Running VP1 on various releases. https://atlas-vp1.web.cern.ch/atlas-vp1/home/documentation/how-to-run-vp1/running-the-latest-vp1-version/.

[59] TruthDAOD Tutorial twiki page. https://twiki.cern.ch/twiki/bin/view/AtlasProtected/TruthDAODTutorial.

[60] TruthDAOD twiki page. https://twiki.cern.ch/twiki/bin/viewauth/AtlasProtected/TruthDAOD.

Appendix A

Closure test for the charge-flip rate for Monte Carlo simulated samples

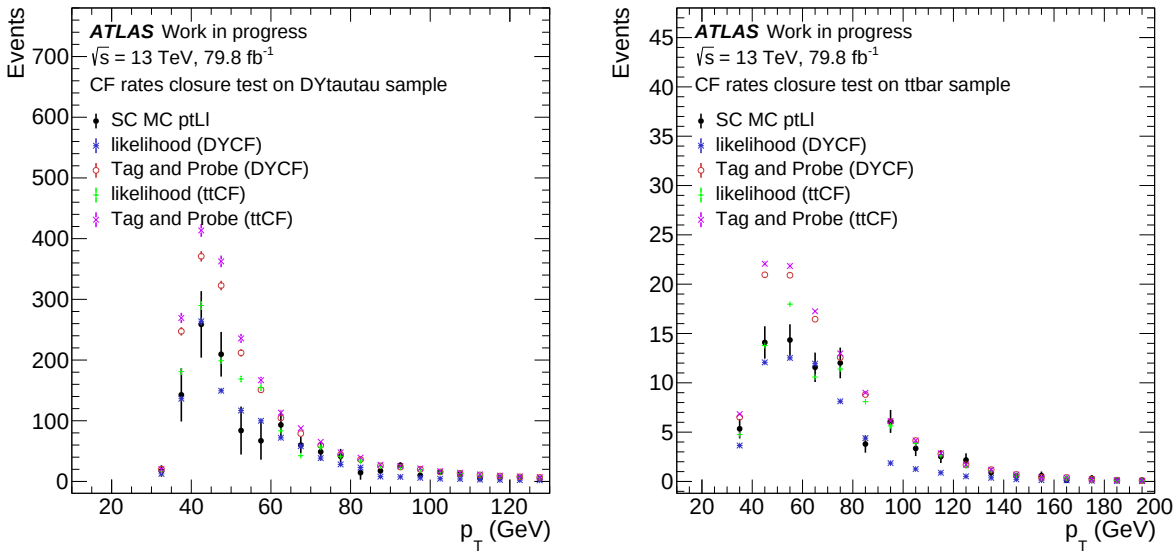

(a) (b)

Fig. A.1 Closure test of the estimated charge-flip rates on leading tau p_T distribution.

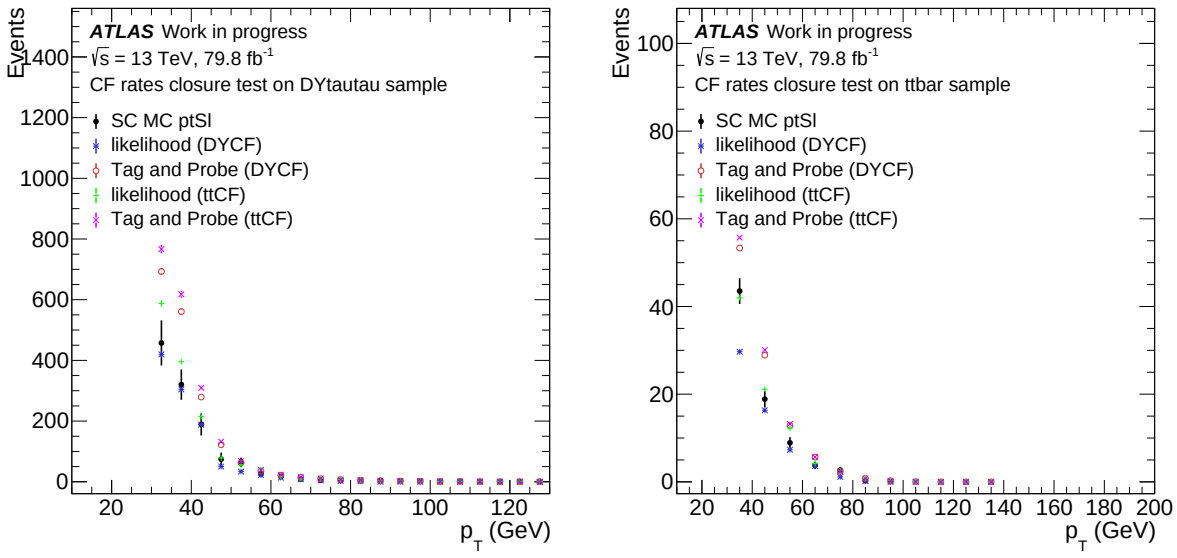

(a) (b)

Fig. A.2 Closure test of the estimated charge-flip rates on sub-leading tau p_T distribution.

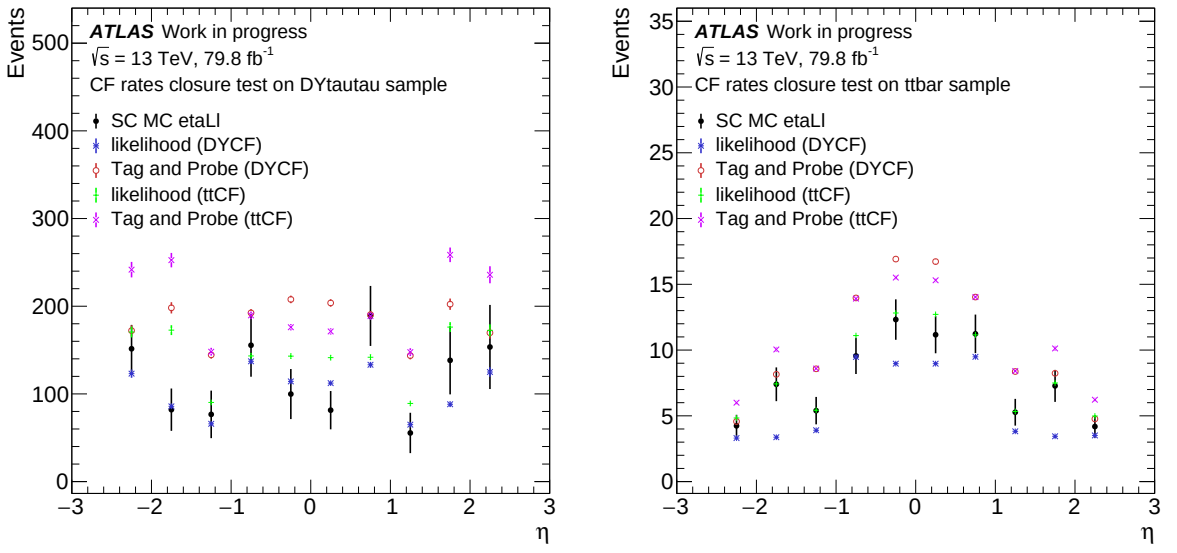

(a) (b)

Fig. A.3 Closure test of the estimated charge-flip rates on leading tau η distribution.

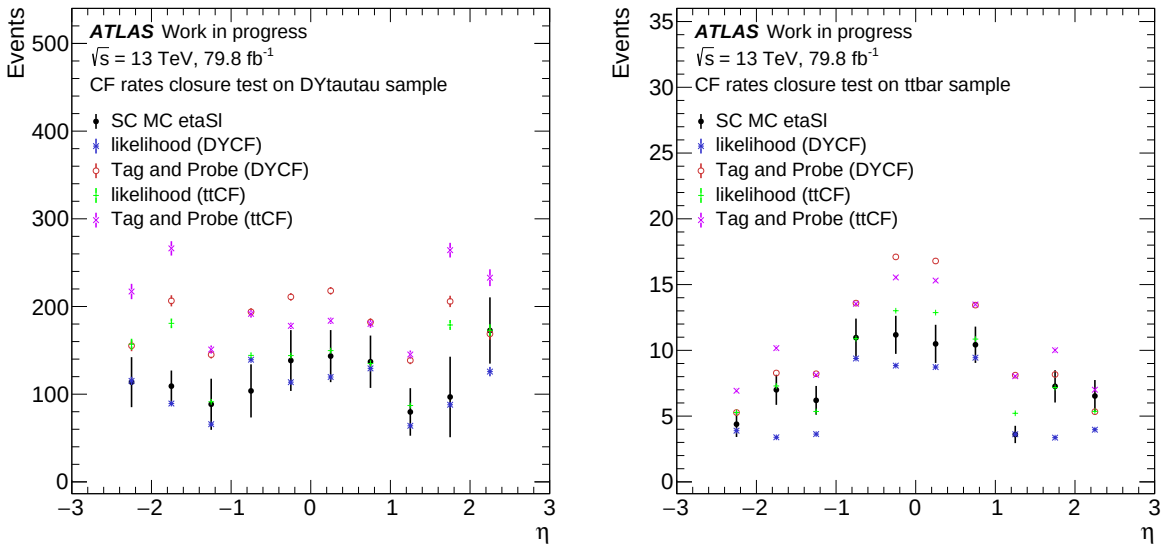

(a) (b)

Fig. A.4 Closure test of the estimated charge-flip rates on sub-leading tau η distribution.

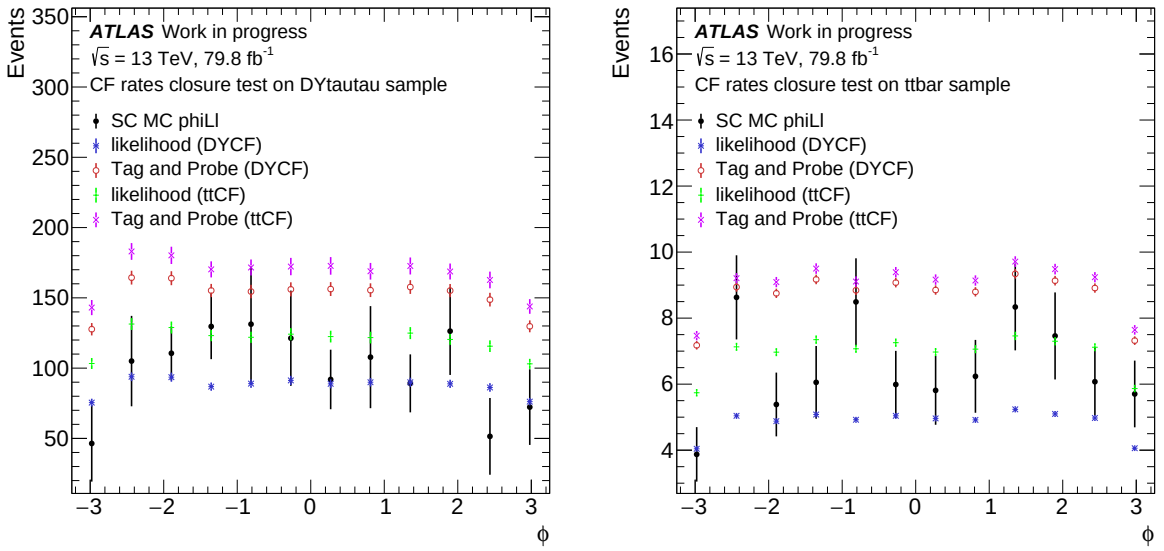

(a) (b)

Fig. A.5 Closure test of the estimated charge-flip rates on leading tau ϕ distribution.

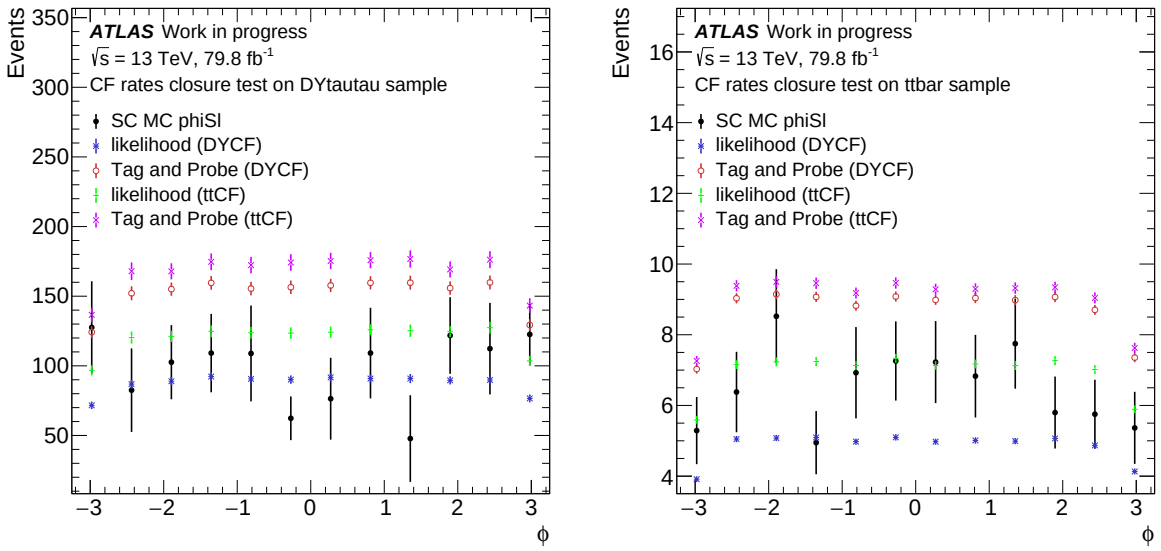

(a) (b)

Fig. A.6 Closure test of the estimated charge-flip rates on sub-leading tau ϕ distribution.

Appendix B

The cause of the charge-flip of hadronic tau

In this section, the study of the cause of the charge-flip of hadronic tau is presented. The current optimum method to achieve the purpose of this study is by using the combination of displaying event recorded as AOD format using Virtual Point 1 (VP1) (see e.g. [56] for latest instructions and updates) and printed out truth information from EVNT file. VP1 runs both remotely on LXPLUS service and locally on a virtual machine loaded with SLC5/6 (Scientific Linux CERN) platforms. The LXPLUS service is used to run VP1 in this study. After testing with different data format, VP1 opens AOD and DAOD files perfectly but unable to be open EVNT files [1].

B.1 Method

The procedure to download the corresponding AOD data set containing the event of interest given the run number and event number and to extract the event of interest from the AOD data set is based on [57]. The commands are summarised as below:

1. `setupATLAS; lsetup eiclient`
2. `el -e "00364130 05581840" -api mc` (This command returns the fileGUID of the AOD, DAOD, or ROD file containing this event. The first number is the event number and the second number is the run number. Note that the run numbers printed out from our SUSY3 ntuples recording the charge-flip events are not same as the run numbers to locate the AOD, DAOD, or ROD data set.)
3. `lsetup pyAMI; voms-proxy-init -voms atlas` (One needs to have a valid grid certificate for it to work)

[1]

4. `ami command AMIGetFileInfo -fileGUID=61ED266E-640A-9245-8F30-AE22F892D47E` (The fileGUID in this example corresponds to the AOD data set. This command returns the LFN denoting the luminosity block in this data set which contain the event of interest.)

5. `lsetup rucio`

6. `rucio download mc16_13TeV:AOD.11189485._000711.pool.root.1` (Download the luminosity block. Each luminosity block has size of around a few GB.)

7. `lsetup asetup; asetup AtlasProduction,21.0.20.1`

8. `acmd.py filter-files -s eventlist.txt AOD.11189485._000711.pool.root.1 -o myEvent.pool.root` (This command extracts the particular event of interest for VP1 to open. The eventlist.txt is a one-line text file recording the run number and the event number. Note that this run number is not same as the run number in step 2, but same as the run number printed out from our SUSY3 ntuples.)

To open the extracted single-event AOD file, the latest instruction to setup VP1 can be found in [58]. It should be noted that the latest instruction is not guaranteed to open the extracted AOD file based on previous instructions since each setup specifically . The well-tested setup uses the old `lxplus6.cern.ch` (instead of `lxplus.cern.ch` corresponding to lxplus7) to log in and set up as the follows:

1. `asetup 22.0.0,Athena,slc6` or `asetup master,latest,Athena,slc6`

2. `export QT_PLUGIN_PATH=/cvmfs/atlas-nightlies.cern.ch/repo/sw/master/sw/lcg/releases/LCG_91/qt5/5.6.2/x86_64-slc6-gcc62-opt/plugins/`

3. `export QT_XKB_CONFIG_ROOT=/cvmfs/sft.cern.ch/lcg/releases/LCG_91/libxkbcommon/0.7.1/x86_64-slc6-gcc62-opt/lib` (Note that step 2 and 3 are only required for `asetup` using 22.0.0.)

4. `vp1 FileName`

Since the AOD files recording the charge-flip events do not contain truth information of the tracks (e.g. the sign of the charge and the type of particle it corresponds to), the exact cause of charge misidentification is unable to be determined. The commands to obtain and print out the full truth records of the event is presented below (see e.g. [59] for more detailed meanings of some commands):

1. `el -e "00364130 05581840" -api mc -p all -details type dataset` (This command returns the fileGUID for all type of data set including EVNT.)

2. `ami command AMIGetFileInfo -fileGUID=3BE0891F-FA32-2043-A22A-6796F7C6E906` (This fileGUID corresponds to the EVNT data set.)

3. `rucio download mc15_13TeV:EVNT.09300364._058536.pool.root.1`

4. `asetup 20.1.8.3,AtlasDerivation,gcc48` (More recent versions are available for AtlasDerivation, but this version match with the command to print out the truth information. The information of more recent versions can be found in [60].)

5. `Reco_tf.py -inputEVNTFile EVNT.09300364._058536.pool.root.1 -outputDAODFile 284500_5581840.pool.root -reductionConf TRUTH0` (Convert EVNT to DAOD format.)

6. `asetup 20.1.8.1,AtlasDerivation,gcc48`

7. `get_files xAODTruthReader_jobOptions.py` (One needs to first open the file `xAODTruthReader_jo` and change the path of the input file to match the TRUTH0 file made above before proceeding to the next step. The number of events that one wants to print out is controlled by the variable "`theApp.EvtMax = -1`", where "`-1`" means "process everything" here.)

8. `athena xAODTruthReader_jobOptions.py > xAODTruth.txt` (It is possible to print out the truth information directly from EVNT file as described in [59], but the information of the decay vertices in the TRUTH0 level DAOD file is clearer. In addition, only TRUTH0 file can be printed out using this method. See e.g. [60] for the description of the difference among EVNT, TRUTH0, TRUTH1, TRUTH2 and TRUTH3. In short, TRUTH0 is an exact copy of the input EVNT, which is desired for this study since it contains all truth information of the event.)

B.2 Results

A number of events are examined and three of them are presented with one corresponding to a 1-prong event and two being 3-prong events.

B.2.1 1-prong event

Based on the truth record of the decay history of the 1-prong event (run number: 284500, event number: 5581840), the Feynman diagram is shown in Fig. B.1. In this event, the hadronic tau decays into one π^- and two π^0's, where both π^0's decay into two photons, respectively.

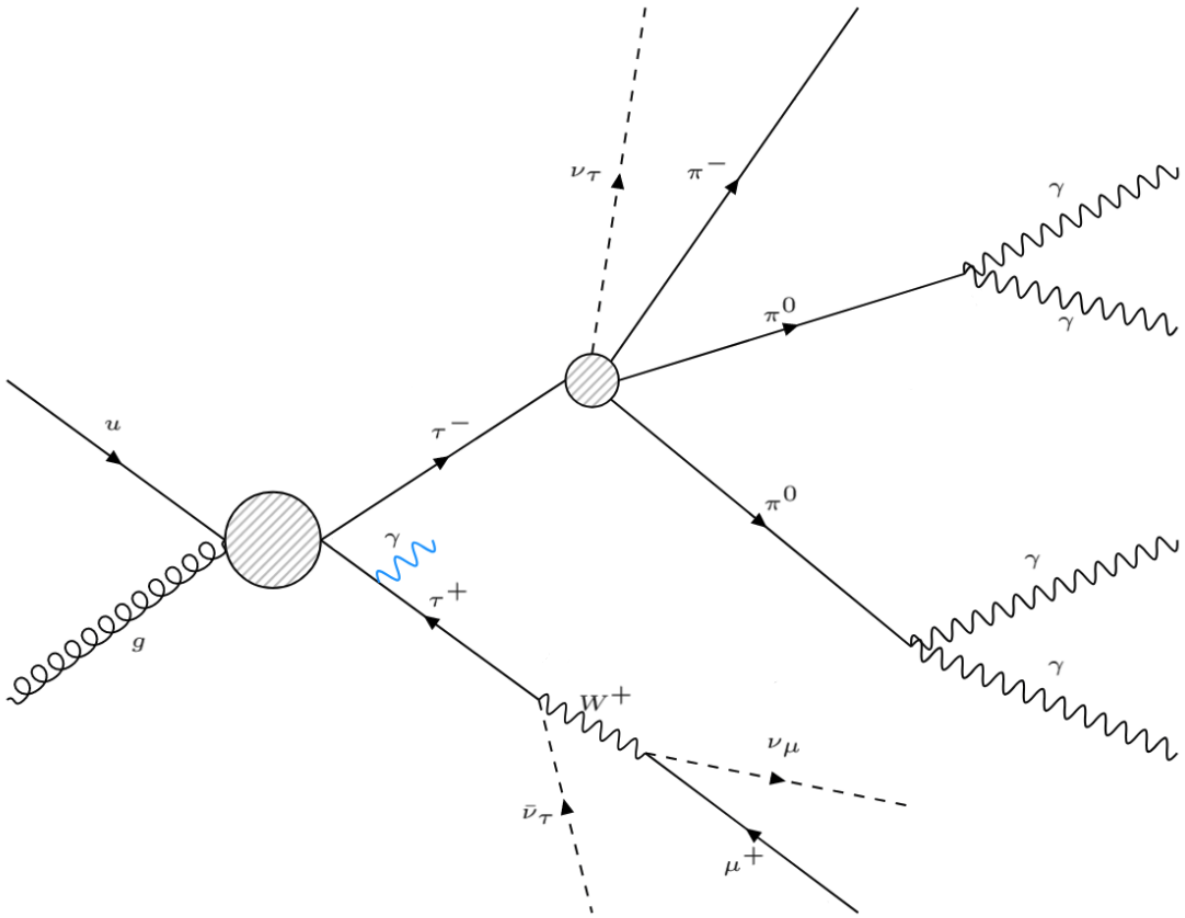

Fig. B.1 The Feynman diagram of the 1-prong event (run number: 284500, event number: 5581840) corresponding to $\tau^+_{\text{had}}\tau^-_\mu \rightarrow \pi^-\pi^0\pi^0\mu^+\nu_\mu\bar{\nu}_\tau$.

The event display of the AOD file for this event is shown in Fig. B.2 with different p_T cuts applied. The colour of the track denotes the sign of the charge with the red and yellow colour denoting positively and negatively charged track, respectively. As shown in Fig. B.2c, only two tracks are left after applying a p_T cut of 10 GeV. The red track on the right side can be clearly identified as μ^+ since it leaves a track in the muon spectrometer. To assure that the right red track indeed corresponds to μ^+, its truth kinematic values from ENVT are checked for the agreement with the kinematics from AOD. Another red track on the right side is matched to π^- by checking the agreement of the truth (from EVNT) and measured (from AOD) values of p_T, $|\vec{p}|$, η and ϕ. The truth and measured values are summarised in table B.1.

Particle	Parameter	Truth value (from EVNT)	Measured value (from AOD)
μ^-	$E \approx \lvert\vec{p}\rvert$	286 GeV	276 GeV
	p_T	53.440 GeV	51.537 GeV
	η	2.362	2.363
	ϕ	2.597	2.590
π^+	$E \approx \lvert\vec{p}\rvert$	80.7 GeV	67.2 GeV
	p_T	14.062 GeV	11.728 GeV
	η	2.433	2.431
	ϕ	0.193	0.199

Table B.1 Summary of the truth and measured values of p_T, $|\vec{p}|$, η and ϕ for the 1-prong event (run number: 284500, event number: 5581840).

In this event, the charge of π^- is misidentified. The reason for this is suggested by the hit summary which says that only three, four and zero hit(s) are left in Pix (silicon pixel detector), SCT and TRT, respectively. The low number of hits leads to difficulties in measuring the curvature of the track precisely. In addition, as shown in Fig. B.2b, other two yellow tracks almost overlap with the π^- track which may cause confusion in determining which hit belonging to its own track. This is further confirmed by the hit summary of these two yellow tracks as shown in table B.2. The second yellow track leaves zero hit in the Pix but up to nine hits in the SCT.

Track	Hit summary		
	Pix (Pixel silicon detector)	SCT	TRT
π^-	3	4	0
Yellow track no. 1	3	10	0
Yellow track no. 2	0	9	0
μ^+	6	8	0

Table B.2 Hit summary of the charged tracks in Fig. B.2b corresponding to the 1-prong event (run number: 284500, event number: 5581840).

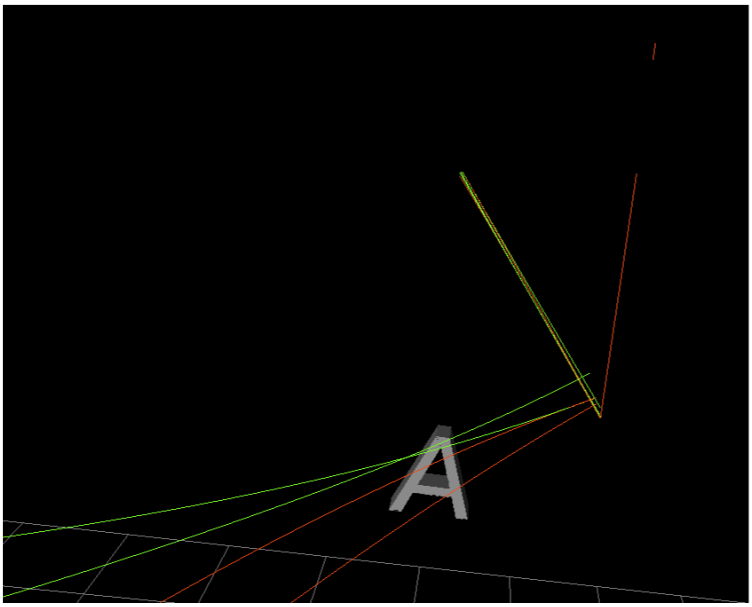

(a)

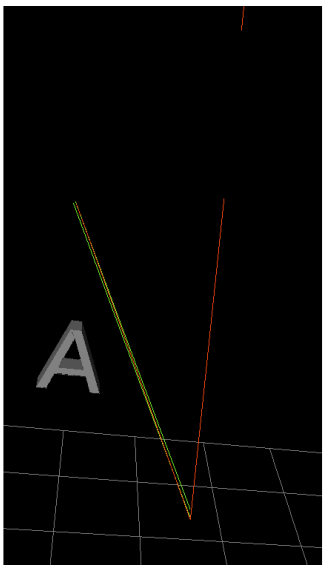

(b)

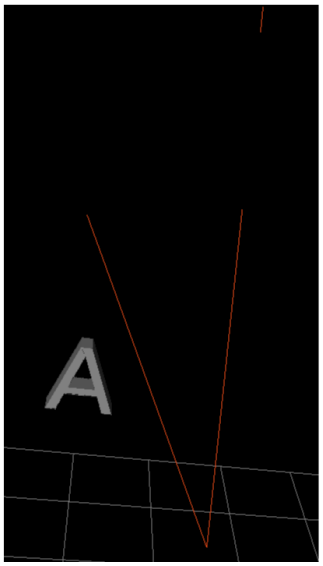

(c)

Fig. B.2 Event display of the AOD file containing the 1-prong event (run number: 284500, event number: 5581840) after applying different p_T cuts: (a) 1 GeV p_T cut, (b) 5 GeV p_T cut, (c) 10 GeV p_T cut. The red and yellow colour indicate positively and negatively charged, respectively.

B.2.2 3-prong event

Run number: 284500; Event number: 4300793

The truth record indicates that this event corresponds to following decay mode:

$$\begin{aligned} \tau^+\tau^- : \tau^- &\rightarrow \pi^+\pi^-\pi^-\pi^0\nu_\tau \\ \tau^+ &\rightarrow \bar{\nu}_\tau\mu^+\nu_\mu. \end{aligned} \tag{B.1}$$

The truth and measured values of p_T, $|\vec{p}|$, η and ϕ are summarised in table B.3.

Particle	Parameter	Truth value (from EVNT)	Measured value (from AOD)
μ^+	$E \approx \lvert\vec{p}\rvert$	37.5 GeV	38.0 GeV
	p_T	32.237 GeV	32.766 GeV
	η	0.560	0.560
	ϕ	0.329	0.375
π^+	$E \approx \lvert\vec{p}\rvert$	7.38 GeV	7.42 GeV
	p_T	7.375 GeV	7.410 GeV
	η	-0.040	-0.041
	ϕ	2.608	2.608
π^- (1^{st})	$E \approx \lvert\vec{p}\rvert$	4.44 GeV	4.47 GeV
	p_T	4.432 GeV	4.469 GeV
	η	-0.029	-0.029
	ϕ	2.559	2.558
π^- (2^{nd})	$E \approx \lvert\vec{p}\rvert$	11.3 GeV	/
	p_T	11.295 GeV	/
	η	-0.075	/
	ϕ	2.625	/
Red track	$E \approx \lvert\vec{p}\rvert$	/	4.792 GeV
	p_T	/	4.777 GeV
	η	/	-0.079
	ϕ	/	2.594

Table B.3 Summary of the truth and measured values of p_T, $|\vec{p}|$, η and ϕ for the 3-prong event (run number: 284500, event number: 4300793).

As shown in Fig. B.3a, only three tracks (two red and one yellow) are recorded in the AOD file to be matched to three charged pion tracks in the truth record. In this event, the truth record of the second π^- (the fourth row in table B.3) cannot be matched to any tracks recorded in the AOD file. The only AOD track in Fig. B.3a left unmatched does not match well with the second

π^- listed in the fourth row not only because the value of η and ϕ does not match as well as other tracks, but also because this track has a much lower measured $|\vec{p}|$ or p_T. The charge of this AOD track is opposite to the truth record, which means that the wrong track with the opposite charge is mismatched to the original π^- track in the AOD file leading to the charge of the τ_{had} being misidentified. The origin of the mismatched AOD track is unclear as the truth record does not include electron-positron pairs originated from the photons from the decay of π^0's. It is speculated that the mismatched track comes from a conversion from one of the photons.

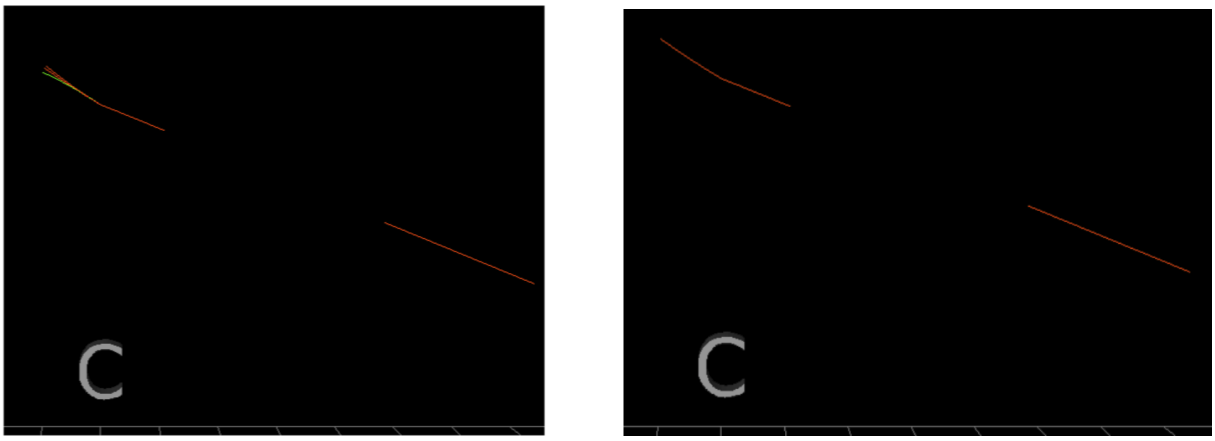

(a) (b)

Fig. B.3 Event display of the AOD file containing the 3-prong event (run number: 284500, event number: 4300793) after applying different p_T cuts: (a) no p_T cut, (b) 5 GeV p_T cut. The red and yellow colour indicate positively and negatively charged, respectively.

Run number: 284500; Event number: 7329244

The truth record indicates that this event corresponds to following decay mode:

$$\begin{aligned} \tau^+\tau^- : \tau^+ &\rightarrow \pi^-\pi^+\pi^+\pi^0\pi^0\pi^0\bar{\nu}_\tau \\ \tau^- &\rightarrow \nu_\tau\mu^-\bar{\nu}_\mu. \end{aligned} \tag{B.2}$$

The truth and measured values of p_T, $|\vec{p}|$, η and ϕ are summarised in table B.4.

Particle	Parameter	Truth value (from EVNT)	Measured value (from AOD)
μ^-	$E \approx \lvert\vec{p}\rvert$	106 GeV	105 GeV
	p_T	42.060 GeV	41.650 GeV
	η	1.572	1.572
	ϕ	0.329	0.330
π^-	$E \approx \lvert\vec{p}\rvert$	49.4 GeV	51.0 GeV
	p_T	13.053 GeV	13.501 GeV
	η	2.005	2.005
	ϕ	2.358	2.359
π^+ (1^{st})	$E \approx \lvert\vec{p}\rvert$	3.81 GeV	4.983 GeV
	p_T	1.012 GeV	1.335 GeV
	η	2.000	1.992
	ϕ	2.340	2.425
π^+ (2^{nd})	$E \approx \lvert\vec{p}\rvert$	9.07 GeV	10.991 GeV (negatively charged)
	p_T	2.291 GeV	2.896 GeV
	η	2.053	2.009
	ϕ	2.344	2.320

Table B.4 Summary of the truth and measured values of p_T, $|\vec{p}|$, η and ϕ for the 3-prong event (run number: 284500, event number: 7329244).

As shown in Fig. B.4a, this event has a lot of charged tracks recorded in the AOD file, while most of the tracks are not in the same direction as the charged pions recorded in the EVNT file. It can be seen in table B.4 that the measured charge of the second π^+ (the fourth row) is opposite to the sign of charge in the truth record. Therefore, the charge of that track is misidentified. By checking the hit summary shown in table B.5, the second π^+ does not leave any hit in the Pix, which could lead to mis-determination of its charge.

Track	Hit summary		
	Pix (Pixel silicon detector)	SCT	TRT
π^-	5	6	19
π^+ (1^{st})	2	9	0
π^+ (2^{nd})	0	9	0
μ^-	4	8	36

Table B.5 Hit summary of the charged tracks in table. B.4 corresponding to the 3-prong event (run number: 284500, event number: 7329244).

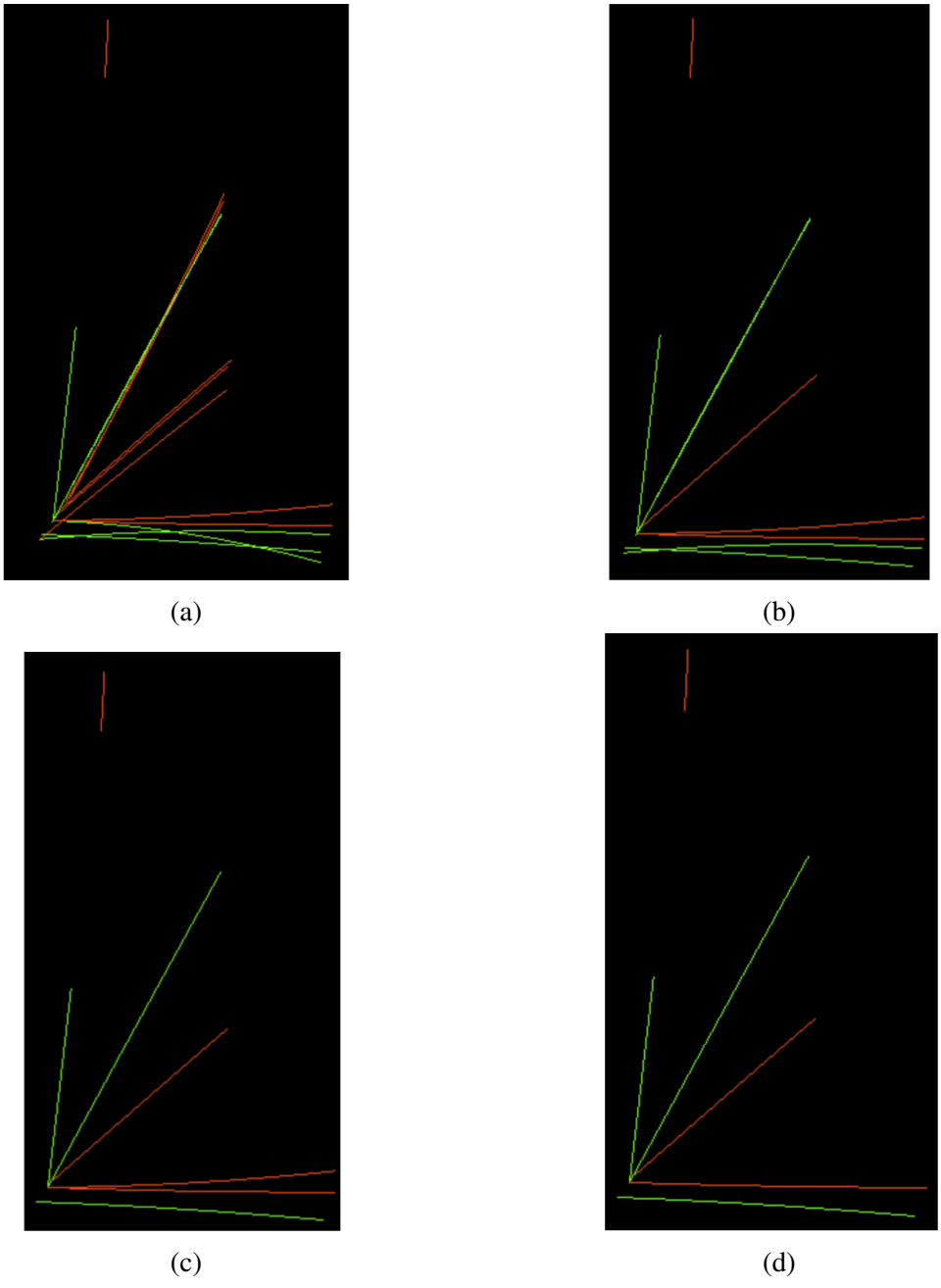

(a) (b)

(c) (d)

Fig. B.4 Event display of the AOD file containing the 3-prong event (run number: 284500, event number: 7329244) after applying different p_T cuts: (a) no p_T cut, (b) 2 GeV p_T cut, (c) 5 GeV p_T cut, (d) 8 GeV p_T cut. The red and yellow colour indicate positively and negatively charged, respectively.

It is also noticed that two parts of the muon track circled out in white (as shown in Fig. B.5) have different colours, which imply that the charge determined by the ID and the muon spectrometer yield opposite signs. Though the charge determined by the ID is assigned to the muon track in the AOD file, the cause of the difference in muon charge is unclear.

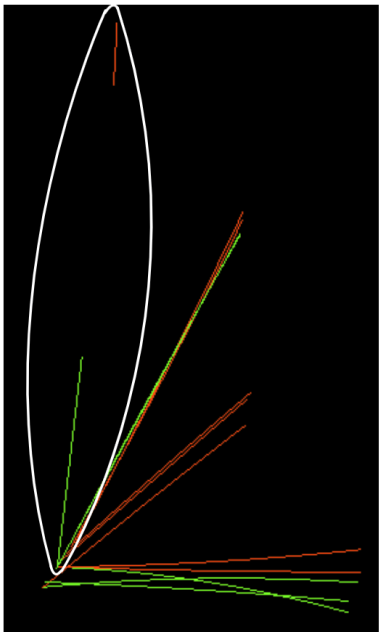

Fig. B.5 Event display of the AOD file containing the 3-prong event with the muon track circled out in white.

B.3 Conclusion

In this appendix, the cause of the charge flip of hadronic taus is studied. The detailed method and commands are presented. Three events with one being 1-prong and two being 3-prong are presented with details. Based on these three events, the causes include:

1. the charge of the charged pion track being misidentified due to poor hits in the ID and the busy environment where charged tracks from the decay of τ_{had} are too close to each other which may cause confusion in determining which hit belonging to its own track (e.g. section B.2.1 and B.2.2.2);

2. another track with opposite charge being misidentified as the true charged pion track (e.g. section B.2.2.1).

It is not possible to conclude the major cause of the charge flip based on three events. Apart from the need to study more events, it will be great if the AOD files with truth information can be created so that the cause will be more clear without the need to match with EVNT files. It is anticipated that a good understanding of the cause of the charge flip of τ_{had} will benefit the improvement of the BDT dedicated for the reconstruction and identification of τ_{had}.